

ANALYSIS AND DESIGN OF FIXED-FREQUENCY CONTROLLED LCL-T TYPE DC-DC SOFT-SWITCHING POWER CONVERTER FOR RENEWABLE ENERGY APPLICATIONS

Thesis

Submitted in partial fulfillment of the requirements for the degree of

DOCTOR OF PHILOSOPHY

by

VIJAYA BHASKAR REDDY G.



DEPARTMENT OF ELECTRICAL AND ELECTRONICS ENGINEERING

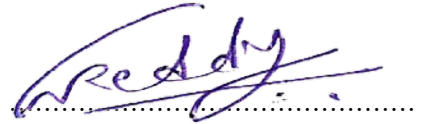
NATIONAL INSTITUTE OF TECHNOLOGY KARNATAKA

SURATHKAL, MANGALORE -575025

JUNE, 2021

DECLARATION

I hereby *declare* that the Research Thesis entitled **Analysis and Design of Fixed-Frequency Controlled LCL-T Type DC-DC Soft-Switching Power Converter for Renewable Energy Applications** which is being submitted to the National Institute of Technology Karnataka, Surathkal in partial fulfillment of the requirement for the award of the Degree of Doctor of Philosophy in Electrical and Electronics Engineering is a *bonafide report of the research work carried out by me*. The material contained in this Research Thesis has not been submitted to any University or Institution for the award of any degree.



Vijaya Bhaskar Reddy G., 158028EE15F06
Department of Electrical and Electronics Engineering

Place: NITK, Surathkal

Date: 25-06-2021

CERTIFICATE


This is to *certify* that the Research Thesis entitled **Analysis and Design of Fixed-Frequency Controlled LCL-T Type DC-DC Soft-Switching Power Converter for Renewable Energy Applications** submitted by Vijaya Bhaskar Reddy G. (Register Number: 158028EE15F06) as the record of the research work carried out by him, is *accepted as the Research Thesis submission* in partial fulfillment of the requirements for the award of degree of Doctor of Philosophy.



25th June, 2021

Dr. Nagendrappa H.

(Research Guide)



Prof. G. S. Punekar

(Chairman-DRPC, EEE Dept.)

Acknowledgements

I would like to thank a number of people who contributed to this dissertation in many different ways:

Firstly, I would like to express my deepest gratitude to my supervisor, Dr. Nagendrappa Harischandrappa, Assistant Professor, Department of Electrical and Electronics Engineering, for his guidance, encouragement and showing trust in me all the time.

I would like to thank my research progress assessment committee (RPAC) members Dr. Sheron Figarado, Dr. Krishnan C M C., and Dr. Geetha V., for their constructive feedback and guidance. Also, I would like to thank Dr. G. S. Punekar, Head of the Department of Electrical and Electronics Engineering, NITK, Surathkal. Thanks also go to Dr. Shubhanga K N., Dr. Venkatesa Perumal and Dr. Vinatha U, former HODs for providing the necessary resources in the department to carry out my research. I also wish to thank Mr. Nayak M., Assistant Engineer, and other non-teaching staff of the EEE department for providing necessary support in conducting experimentation.

I am truly grateful to my friends Uday Patil, Srikanth, Reddy Prasad, Sai Krishna, Ravi Teja, Omkar, and Kavya for their support and encouragement in carrying out my research work. I would like to express my heartfelt thanks to all my colleagues, I have gained a lot from them through scholarly interactions.

I would like to express my deepest gratitude towards my parents and my sister for their love and patience which kept me going on this journey. Their faith and unconditional love towards me are the reason for whatever I have achieved in my life.

VIJAYA BHASKAR REDDY G.

Abstract

Electrical power is one of the important requirements for sustainable development of any nation. A wider gap is being created between the power supply and the ever increasing power demand. The available conventional energy sources are either insufficient or cannot sustain for long to meet the current power demand as they are depleting in nature. Renewable energy sources (RESs) have been the most attractive alternate sources of energy for meeting the ever increasing power demand. Power generation from renewable energy sources depend on atmospheric conditions and hence the power produced is highly fluctuating in nature. To convert this fluctuating power into usable constant power, a power conditioning system is essential. DC-DC converter is one of the important components of the power conditioning system. This research is to find a suitable DC-DC resonant power converter topology that can be used in solar power generation applications and investigate on its performance. Therefore, in this work, the literature survey on resonant converter topologies, power controlling methods, and analysis methods are presented.

Fixed-frequency control makes the design of magnetic components and filters simple for effective filtering. Therefore, in this study, two fixed-frequency control schemes have been proposed. The first fixed-frequency control scheme is phase-shifted gating (PSG) control and the second is modified gating signal (MGS) control. The proposed PSG and MGS control schemes are experimentally validated and the choice between schemes is made by comparing the performance of the converter. It is found that both the gating schemes are effective in regulating the output voltage for variable input voltage and loading conditions. However, the efficiency of the converter is found to be higher with MGS due to the fact that only one switch loses ZVS as compared to two with the PSG when operated with maximum input voltage. Also, the variation in pulse-width angle (δ) required to regulate the output voltage is small in MGS as compared to that with PSG.

The complete behavior of the resonant converter at different intervals of the operation can be predicted by analysing the circuit in steady-state

and transient state. Two steady-state analysis methods have been proposed in this work. Firstly, fundamental harmonic approximation (FHA) method, and second, Fourier series (FS) method. The proposed steady-state analysis methods are experimentally validated. The performance of the LCL-T converter designed by using the FHA and FS analysis methods is compared. Fourier series method gives efficient results since it considers n-harmonic components of voltages and currents as compared to the fundamental harmonic approximation (FHA) method where, only fundamental component is considered. In order to understand the complete behavior of the converter for fluctuations in the input, load, and control parameters, small-signal modeling of the converter is essential. Therefore, an extended describing function (EDF) method available in the literature is used in this work for small signal modeling of the converter. It is convenient to derive all small-signal transfer functions and improve the accuracy by using the EDF method since it combines both the time-domain and frequency-domain analyses.

Contents

Acknowledgements	i
Abstract	iii
List of figures	vii
List of tables	xii
Nomenclature	xiii
Abbreviations	xiii
1 INTRODUCTION	1
1.1 SOLAR PHOTOVOLTAIC POWER GENERATION	2
1.2 GRID INTERFACING	4
1.3 DC-DC POWER CONVERTERS	4
1.3.1 HARD-SWITCHING CONVERTERS	5
1.3.2 SOFT-SWITCHING CONVERTERS	5
1.4 SOFT-SWITCHING MECHANISM	6
1.4.1 ZERO VOLTAGE SWITCHING (ZVS)	6
1.4.2 ZERO CURRENT SWITCHING (ZCS)	8
1.5 MOTIVATION OF THIS WORK	9
1.6 PROBLEM STATEMENT	9
1.7 THESIS ORGANIZATION	10
2 LITERATURE REVIEW	11
2.1 RESONANT POWER CONVERTER TOPOLOGIES	12
2.1.1 TWO-ELEMENT RC TOPOLOGIES	14
2.1.2 THREE-ELEMENT RC TOPOLOGIES	14
2.2 POWER CONTROLLING METHODS	16
2.2.1 VARIABLE-FREQUENCY CONTROL	16
2.2.2 FIXED-FREQUENCY CONTROL	18

2.3	ANALYSIS METHODS	18
2.3.1	STEADY-STATE ANALYSIS	19
2.3.2	TRANSIENT ANALYSIS	19
2.4	IDENTIFIED RESEARCH GAPS	21
2.5	RESEARCH OBJECTIVES	21
3	PHASE-SHIFTED GATING SIGNAL CONTROLLED LCL-T RES-	
	ONANT POWER CONVERTER	23
3.1	CIRCUIT DESCRIPTION	24
3.2	OPERATING PRINCIPLE OF PSG CONTROL	27
3.2.1	OPERATING MODES	27
3.2.1.1	Mode-1 ($S_3, D_1 = \text{ON}$)	27
3.2.1.2	Mode-2 ($D_1, D_2 = \text{ON}$)	29
3.2.1.3	Mode-3 ($S_1, S_2 = \text{ON}$)	29
3.2.1.4	Mode-4 ($S_2, D_4 = \text{ON}$)	29
3.2.1.5	Mode-5 ($D_4, D_3 = \text{ON}$)	30
3.2.1.6	Mode-6 ($S_4, S_3 = \text{ON}$)	30
3.3	STEADY-STATE ANALYSIS	30
3.3.1	MODELING	31
3.3.2	ANALYSIS	34
3.3.3	ZVS CONDITIONS	36
3.4	DESIGN	37
3.4.1	DESIGN TRADE-OFFS	39
3.4.2	DESIGN SUMMARY	40
3.5	SIMULATION RESULTS	40
3.6	EXPERIMENTAL RESULTS	47
3.7	SUMMARY	52
4	MODIFIED GATING SIGNALS CONTROLLED LCL-T RPC AND	
	COMPARISONS	53
4.1	OPERATING PRINCIPLE OF MGS CONTROL SCHEME	54
4.1.1	OPERATING MODES	54
4.1.1.1	Mode-1 ($D_1, D_2 = \text{ON}$)	54
4.1.1.2	Mode-2 ($S_1, S_2 = \text{ON}$)	58
4.1.1.3	Mode-3 ($S_1, D_3 = \text{ON}$)	58

4.1.1.4	Mode-4 ($D_3, D_4 = \text{ON}$)	58
4.1.1.5	Mode-5 ($S_3, S_4 = \text{ON}$)	59
4.2	STEADY-STATE ANALYSIS USING FOURIER SERIES	59
4.2.1	MODELING	59
4.2.2	NORMALIZATION	61
4.2.3	ANALYSIS	62
4.2.4	ZVS CONDITIONS	65
4.3	DESIGN	66
4.3.1	DESIGN TRADE-OFFS	67
4.4	SIMULATION RESULTS	70
4.5	EXPERIMENTAL RESULTS	76
4.6	PERFORMANCE COMPARISON OF PSG AND MGS CONTROL SCHEMES	81
4.7	SUMMARY	87
5	SMALL-SIGNAL MODELING OF LCL-T RESONANT POWER CONVERTER	89
5.1	SMALL-SIGNAL MODELING	89
5.1.1	STATE-SPACE ANALYSIS	90
5.1.2	TRANSFER FUNCTIONS	95
5.2	CLOSED LOOP CONTROL	96
5.3	SUMMARY	96
6	CONCLUSIONS AND FUTURE SCOPE	97
6.1	CONTRIBUTIONS	97
6.2	CONCLUSIONS	99
6.3	FUTURE SCOPE	100
	BIBLIOGRAPHY	108
	PUBLICATIONS BASED ON THE THESIS	118

List of Figures

1.1	Equivalent circuit of a photovoltaic cell.	2
1.2	Characteristics of a photovoltaic cell.	3
1.3	Block diagram representation of grid integration of renewable energy sources.	4
1.4	Classification of DC-DC converters.	5
1.5	ZVS phenomena: (a) Circuit diagram of half-bridge resonant converter, (b) Waveforms of voltage across and current through switch S_1	7
1.6	ZCS phenomena: (a) Circuit diagram of half-bridge resonant converter, (b) Waveforms of voltage across and current through switch S_1	8
2.1	Basic structure of DC-DC isolated resonant power converter.	12
2.2	Classification of resonant power converters.	13
2.3	Two-element resonant converter topologies	13
2.4	Three-element resonant converter topologies	14
3.1	Circuit diagram of single-phase full-bridge LCL-T resonant power converter.	24
3.2	Typical operating waveforms of the proposed phase-shift controlled LCL-T converter.	25
3.3	Typical operating switching waveforms of the proposed phase-shift controlled LCL-T converter.	26
3.4	Equivalent circuits of LCL-T converter operating in: (a) mode-1 ($S_3, D_1 = \text{ON}$), (b) mode-2 ($D_1, D_2 = \text{ON}$), (c) mode-3 ($S_1, S_2 = \text{ON}$), (d) mode-4 ($S_2, D_4 = \text{ON}$), (e) mode-5 ($D_4, D_3 = \text{ON}$), (f) mode-6 ($S_4, S_3 = \text{ON}$)	28

3.5	Simplification of converter circuit: (a) representation of HF transformer by its T-equivalent, (b) series connected L_1 , L'_2 , and L are replaced by L_t , (c) diode rectifier, filter capacitor and load resistance equivalently represented by an AC resistance R_{ac} , and (d) phasor circuit for analysis.	32
3.6	Input voltage and current waveforms of the diode rectifier which are used in deriving the expression for R_{ac}	33
3.7	Plot of: kVA/kW versus F for (a) $K = 1$ and (b) $K = 1.1$; I_{Lsp} versus I_o for (c) $K = 1$ and (d) $K = 1.1$	38
3.8	Design curves: (a) percentage of δ versus percentage of I_o for variations in F with $Q = 2.5$ and $K = 1$. (b) M versus F for variations in Q with $K = 1$	39
3.9	Simulation waveforms for cases 1 and 2: (a), (c) Current through and voltage across inverter switches; (b), (d) v_{AB} , i_{Ls} , v_{Cs} , v_{Cs} , i_{Lt} , v_{rect} , and i_{rect}	42
3.10	Simulation waveforms for cases 3 and 4: (a), (c) Current through and voltage across inverter switches; (b), (d) v_{AB} , i_{Ls} , v_{Cs} , v_{Cs} , i_{Lt} , v_{rect} , and i_{rect}	43
3.11	Simulation waveforms for cases 5 and 6: (a), (c) Current through and voltage across inverter switches; (b), (d) v_{AB} , i_{Ls} , v_{Cs} , v_{Cs} , i_{Lt} , v_{rect} , and i_{rect}	44
3.12	Experimental setup of 300 W LCL-T resonant power converter.	46
3.13	Experimental waveforms for case-1 ($V_s(\text{min.}) = 110$ V & full load, $R_L = 161.17 \Omega$): (a) v_{AB} , i_{Ls} , v_{pri} , v_{rect} , (b) v_{rect} , i_{rect}	47
3.14	Experimental waveforms for case-2 ($V_s(\text{min.}) = 110$ V & half load, $R_L = 322.34 \Omega$): (a) v_{AB} , i_{Ls} , v_{pri} , v_{rect} , (b) v_{rect} , i_{rect}	48
3.15	Experimental waveforms for case-3 ($V_s(\text{min.}) = 110$ V & 10% of full load, $R_L = 1611.7 \Omega$).	48
3.16	Experimental waveforms for case-4 ($V_s(\text{max.}) = 180$ V & full load, $R_L = 161.17 \Omega$).	49
3.17	Experimental waveforms for case-5 ($V_s(\text{max.}) = 180$ V & half load, $R_L = 322.34 \Omega$).	49
3.18	Experimental waveforms for case-6 ($V_s(\text{max.}) = 180$ V & 10% of full load, $R_L = 1611.7 \Omega$).	50

3.19	Efficiency comparison plot of theoretical, simulation, and experimental results at: (a) the minimum input voltage (i.e., $V_s(\min) = 110$ V), (b) the maximum input voltage (i.e., $V_s(\max) = 180$ V).	50
4.1	Typical operating waveforms of the proposed modified gating signal controlled LCL-T converter.	55
4.2	Typical switching waveforms of the proposed modified gating signal controlled LCL-T converter.	56
4.3	Equivalent circuits of LCL-T converter operating in: (a) mode-1 ($D_1, D_2 = \text{ON}$), (b) mode-2 ($S_1, S_2 = \text{ON}$), (c) mode-3 ($S_1, D_3 = \text{ON}$), (d) mode-4 ($D_3, D_4 = \text{ON}$), (e) mode-5 ($S_3, S_4 = \text{ON}$).	57
4.4	Simplification of converter circuit: (a) high frequency transformer represented as T-connection, (b) equivalent circuit of Fig. 4.4(a) after L_m treated as open circuit, (c) equivalent circuit of Fig. 4.4(b) after combining $L_1 + L'_2 + L = L_t$ and represented with the rectifier input voltage, and (d) phasor equivalent circuit for n^{th} harmonic of Fig. 4.4(c) used for analysis.	60
4.5	Variation of resonant tank kVA/kW versus converter gain (M): (a) for different values of F with $K = 0.8$, and (b) for different values of K with $F = 1.4$	67
4.6	Variation of peak resonant current (I_{Lsp}) versus converter gain (M) for variations in F with: (a) $K = 0.8$, and (b) $K = 1$	68
4.7	Variation of: (a) pulse width angle (δ) versus percentage of load current, and (b) normalized output current (J) versus M with $K = 0.8$	68
4.8	Block diagram indicating the steps involved in converter design.	69
4.9	The block diagram of control process in the event of changes in load/input voltage.	71
4.10	Simulation waveforms with $V_s(\min.) = 110$ V: (a) inverter switch currents and voltages to show ZVS in full load, $R_L = 161.17 \Omega$. Waveforms of v_{AB} , i_{Ls} , v_{Cs} , v_{pri} , i_{Lt} , v_{rect} and i_{rect} at: (b) full load ($R_L = 161.17 \Omega$), (c) half load ($R_L = 322.34 \Omega$), (d) 10% of full load ($R_L = 1611.7 \Omega$).	72

4.11	Simulation waveforms with $V_s(\text{max.}) = 180 \text{ V}$: (a) inverter switch currents and voltages to show ZVS in full load, $R_L = 161.17 \Omega$. Waveforms of v_{AB} , i_{Ls} , v_{Cs} , v_{pri} , i_{Lt} , v_{rect} and i_{rect} at: (b) full load ($R_L = 161.17 \Omega$), (c) half load ($R_L = 322.34 \Omega$), (d) 10% of full load ($R_L = 1611.7 \Omega$).	73
4.12	simulation waveforms of resonant/switch current (i_{Ls}) and output voltage (V_o) during (a) load short circuit test, (b) no-load test.	75
4.13	Power loss distribution of a 300 W LCL-T resonant power converter for full load to 10% of full load at: (a) the minimum input voltage (i.e., $V_s(\text{min.}) = 110 \text{ V}$), (b) the maximum input voltage (i.e., $V_s(\text{max.}) = 180 \text{ V}$).	75
4.14	Experimental waveforms of case-1 ($V_s(\text{min.}) = 110 \text{ V}$ & full load, $R_L = 161.17 \Omega$): (a) v_{AB} , i_{Ls} , v_{pri} , v_{rect} ; (b) v_{rect} , i_{rect}	76
4.15	Experimental waveforms of case-2 ($V_s(\text{min.}) = 110 \text{ V}$ & half load, $R_L = 322.34 \Omega$): (a) v_{AB} , i_{Ls} , v_{pri} , v_{rect} ; (b) v_{rect} , i_{rect}	77
4.16	Experimental waveforms of case-3 ($V_s(\text{min.}) = 110 \text{ V}$ & 10% of full load, $R_L = 1611.7 \Omega$): (a) v_{AB} , i_{Ls} , v_{pri} , v_{rect} ; (b) v_{rect} , i_{rect}	78
4.17	Experimental waveforms for case-4 ($V_s(\text{max.}) = 180 \text{ V}$ & full load, $R_L = 161.17 \Omega$): (a) v_{AB} , i_{Ls} , v_{pri} , v_{rect} ; (b) v_{rect} , i_{rect}	78
4.18	Experimental waveforms for case-5 ($V_s(\text{max.}) = 180 \text{ V}$ & half load, $R_L = 322.34 \Omega$): (a) v_{AB} , i_{Ls} , v_{pri} , v_{rect} ; (b) v_{rect} , i_{rect}	79
4.19	Experimental waveforms for case-6 ($V_s(\text{max.}) = 180 \text{ V}$ & 10% of full load, $R_L = 1611.7 \Omega$): (a) v_{AB} , i_{Ls} , v_{pri} , v_{rect} ; (b) v_{rect} , i_{rect}	79
4.20	Experimental efficiency versus load.	81
4.21	Simulation waveforms with $V_s(\text{min.}) = 110 \text{ V}$: (a) Inverter switch currents and voltages to show ZVS in full load, $R_L = 161.17 \Omega$. Waveforms of v_{AB} , i_{Ls} , v_{Cs} , v_{pri} , i_{Lt} , v_{rect} and i_{rect} at: (b) full load ($R_L = 161.17 \Omega$), (c) half load ($R_L = 322.34 \Omega$), (d) 10% of full load ($R_L = 1611.7 \Omega$).	82
4.22	Simulation waveforms with $V_s(\text{max.}) = 180 \text{ V}$: (a) Inverter switch currents and voltages to show ZVS in full load, $R_L = 161.17 \Omega$. Waveforms of v_{AB} , i_{Ls} , v_{Cs} , v_{pri} , i_{Lt} , v_{rect} and i_{rect} at: (b) full load ($R_L = 161.17 \Omega$), (c) half load ($R_L = 322.34 \Omega$), (d) 10% of full load ($R_L = 1611.7 \Omega$).	83
4.23	Power loss calculations: (a) at different stages of circuit in case-1, (b) turn-on loss for all cases in PSG and MGS control.	84

4.24	Experimental waveforms of v_{AB} , i_{Ls} , v_{pri} , and v_{rect} : (a) case-1, (b) case-2, (c) case-3, (d) case-4, (e) case-5, and (f) case-6.	85
4.25	Theoretical, simulation, and experimental efficiency comparison plot.	86
5.1	Conceptual diagram for small-signal model of resonant converters (Yang et al., 1992).	90
5.2	Equivalent circuit at the inverter output terminals of LCL-T resonant power converter.	90
5.3	Voltage feedback control scheme to control the output voltage of the converter.	96
A.1	Rectifier input voltage waveform	102
A.2	Inverter output voltage waveform with phase-shifted gating control scheme	103
A.3	Inverter output voltage waveform with modified gating signals control scheme	104
B.1	Typical voltage and current waveforms of a MOSFET during turn-on and turn-off process (v_{DS} : Drain to source voltage, i_{DS} : Drain current, v_{GS} : Gating signal, t_{on} : turn-on time, t_{off} : turn-off time, t_d : delay time, t_r : rise time of the MOSFET).	106

List of Tables

2.1	Resonant power converter topologies	15
2.2	Resonant power converter power controlling methods	17
2.3	Resonant converter steady-state and transient state analysis methods	20
3.1	Design specification of the converter	38
3.2	Summary of power loss calculations	45
3.3	Details of the components used in experimental prototype	46
3.4	Comparison of theoretical, simulation, and experimental results . . .	51
4.1	Details of the components used in experimental prototype	76
4.2	Comparison of theoretical, simulation, and experimental results . . .	80
4.3	Experimental performance comparison of PSG and MGS control schemes	87
4.4	Comparison of resonant power converter topologies	88
4.5	Comparison of FS analysis over FHA analysis	88

Nomenclature

ADC	Asymmetrical duty cycle
FF	Fixed-frequency
FHA	Fundamental harmonic approximation
FS	Fourier series
HF	High-frequency
max.	Maximum
MGS	Modified-gating signal
min.	Minimum
PRC	Parallel resonant converter
PSG	Phase-shifted gating
RC	Resonant converter
RPS	Resonant power converter
SPRC	Series-parallel resonant converter
SRC	Series resonant converter
ZCS	Zero-current switching
ZVS	Zero-voltage switching
I_o	Converter DC output current
I_s	Converter DC input current
K	Inductors's ratio
M	Converter DC voltage gain
n_t	Trasformer turns ratio
v_{AB}	Inverter output voltage
V_o	Converter DC ouput voltage
V_s	Converter DC input voltage
α	Phase-shifting angle
δ	Pulse-width angle
ϕ	Impedance anagle
θ	Rectifier voltage phase-shift angle
ω_s	Angular switching frequency
ω_r	Angular resonant frequency

Chapter 1

INTRODUCTION

Contents

1.1	SOLAR PHOTOVOLTAIC POWER GENERATION	2
1.2	GRID INTERFACING	4
1.3	DC-DC POWER CONVERTERS	4
1.3.1	HARD-SWITCHING CONVERTERS	5
1.3.2	SOFT-SWITCHING CONVERTERS	5
1.4	SOFT-SWITCHING MECHANISM	6
1.4.1	ZERO VOLTAGE SWITCHING (ZVS)	6
1.4.2	ZERO CURRENT SWITCHING (ZCS)	8
1.5	MOTIVATION OF THIS WORK	9
1.6	PROBLEM STATEMENT	9
1.7	THESIS ORGANIZATION	10

In this chapter, a brief introduction to the integration of renewable energy sources to grid using DC-DC power converters and soft-switching mechanisms are discussed. Also, organization of the thesis as chapters is given.

Electrical power is one of the important requirements for sustainable development of any nation. A wider gap is being created between the power supply and the ever increasing power demand. The available conventional energy sources are either insufficient or cannot sustain for long to meet the current power demand as they are depleting in nature. Also some of the conventional energy sources (e.g., coal)

are highly polluting and can contribute to the undesired global warming. Hence, renewable energy sources (RESs) e.g., photovoltaics, wind, fuel cells etc. have been the most attractive alternate sources of energy. Among all RESs, use of solar energy is becoming very popular day by day due to the availability of the sunlight.

1.1 SOLAR PHOTOVOLTAIC POWER GENERATION

Photovoltaic cell (PV cell) is the main component for producing solar energy in the solar photovoltaic system. It converts sunlight directly into electricity without making any harm to our environment. Typical PV cells produce very small range of power. Hence, these cells are connected in series and/or parallel to form a module, which can produce the power in the range of few hundred watts. Further increasing the power range, these modules can be connected in series and/or parallel to form the arrays.

The power generated by PV modules depend on the cell temperature (T) and irradiance (G) falling on its surface (Lappalainen and Valkealahti, 2016). The single diode solar cell model shown in Fig. 1.1 is an efficient model to analyse PV cell (Hyeonah Park and Hyosung Kim, 2013) characteristics for variation in different parameters (T and G). In a PV cell there is an equivalent circuit that consists of a diode (D), a series resistor (R_s), a current source (I_{Ph}) and a shunt resistance (R_p).

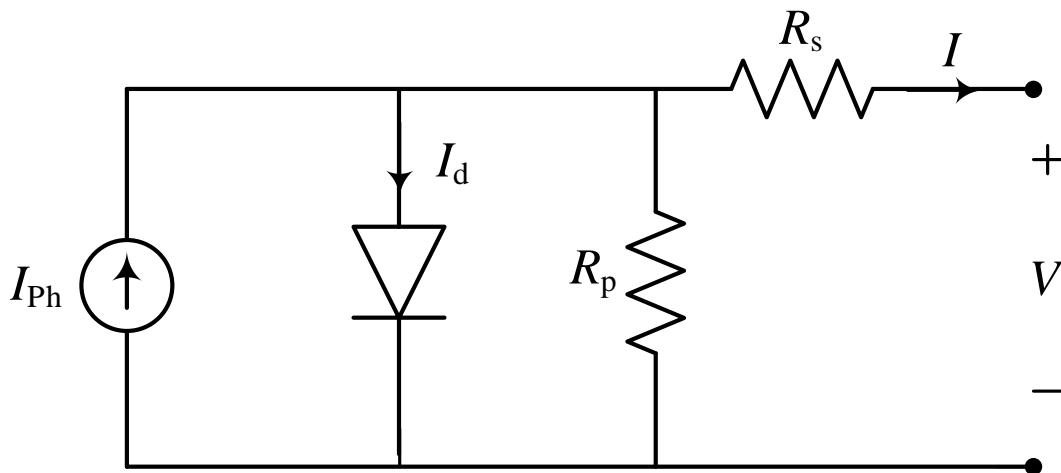


Figure 1.1: Equivalent circuit of a photovoltaic cell.

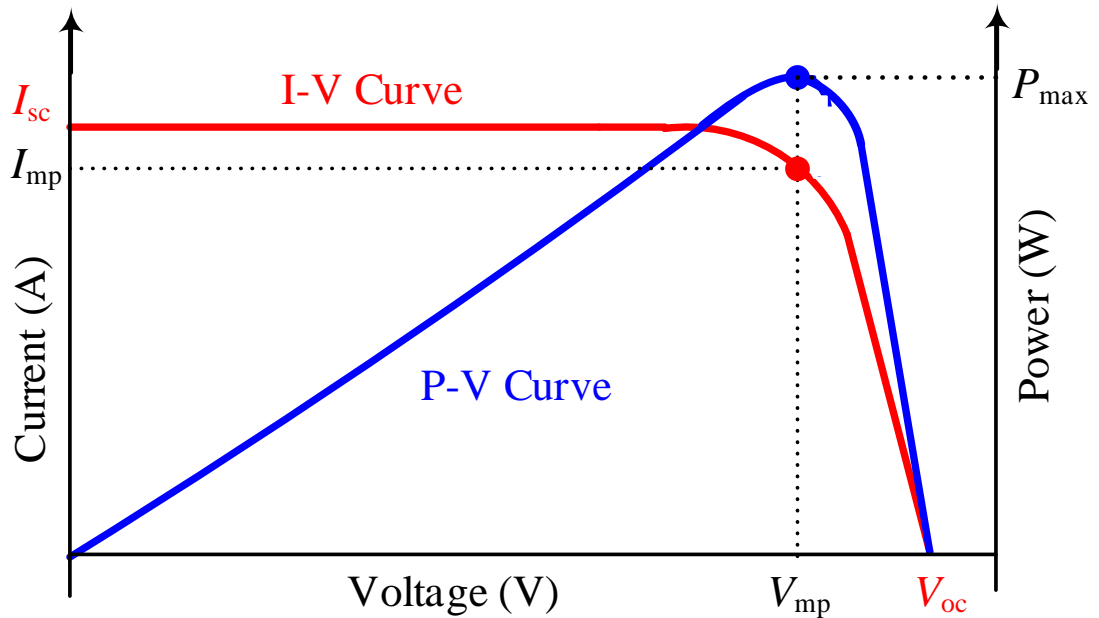


Figure 1.2: Characteristics of a photovoltaic cell.

The current produced by PV source depends on amount of solar radiation falling on PV Surface. The resistance between the metal contacts is represented by series resistance (R_s). The shunt resistance (R_p) represents the resistance offered to leakage path of the current flow in a PV cell and therefore, it is represented in parallel with the current source (Ahmed et al., 2016).

The current and voltage (I-V) characteristics of a photovoltaic (PV) cell is shown in Fig. 1.2. Electrical I-V characteristics (particularly P_{max}) of a solar cell or panel are useful in determining the solar device's performance and efficiency. When the solar cell is open-circuited, the current (I) will be at its minimum (zero) and the voltage (V) across the cell is at its maximum and it is known as the open circuit voltage (V_{oc}) of the solar cell. At the other extreme, when the solar cell is short circuited, the voltage across the cell is at its minimum (zero) but the current flowing out of the cell reaches its maximum and it is known as the short circuit current (I_{sc}) of the solar cell.

There is one particular combination of current and voltage for which the power reaches its maximum value (P_{max}) i.e., at I_{mp} and V_{mp} in Fig. 1.2. This point is called as the 'maximum power point' (MPP) (Abdelsalam et al., 2011). Therefore, the ideal operation of a photovoltaic cell (or panel) is defined to be at the maximum power

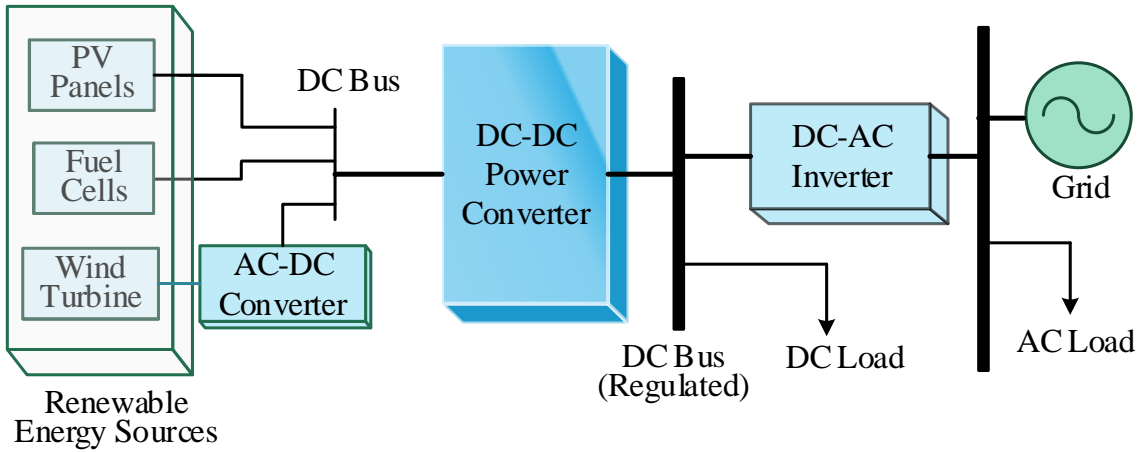


Figure 1.3: Block diagram representation of grid integration of renewable energy sources.

point. Since solar cell output voltage and current both depend on temperature, the actual output power will vary with changes in ambient temperature.

1.2 GRID INTERFACING

The generation of energy from renewable energy sources depends on the atmospheric conditions. Therefore, to control and convert this variable power into constant useful power, power conditioning system (i.e., DC-DC converter, DC-AC converter etc.) is essential (Li and He, 2011, Wai and Wang, 2008). The block diagram of grid interfacing of renewable energy sources using power conditioning system is shown in Fig. 1.3.

1.3 DC-DC POWER CONVERTERS

DC-DC converter is one of the important components of the power conditioning system in grid interfacing of renewable energy sources (Fig. 1.3). The general classification of DC-DC converters is shown in Fig. 1.4. These DC-DC converters are broadly classified as hard-switching and soft-switching converters.

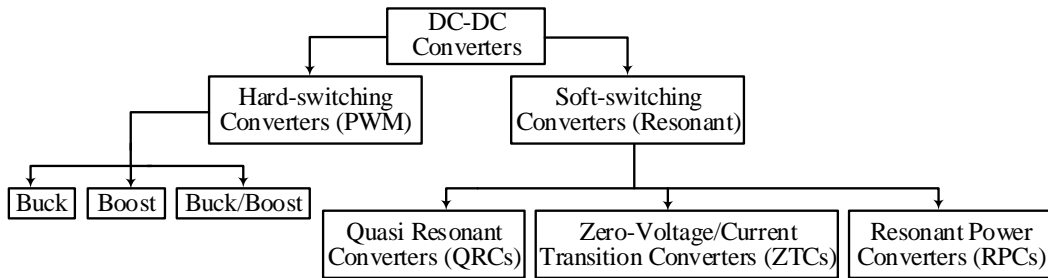


Figure 1.4: Classification of DC-DC converters.

1.3.1 HARD-SWITCHING CONVERTERS

The hard-switching converters use pulse-width modulation methods to control the power flow in the circuit. Hence, these converters are also called pulse-width modulation (PWM) converters (Tasi-Fu Wu and Yu-Kai Chen, 1998). Electrical isolation is essential for safety concerns in grid-tie applications. The line frequency (50/60 Hz) transformer which is used for electrical isolation in PWM converters makes the system bulky and also increases the cost. The size of transformer and other magnetic components can be reduced by increasing the switching frequency. But, increasing the switching frequency in the PWM converters leads to higher switching losses that results in poor efficiency. Hence, the PWM converters operation is limited to a few kilohertz (kHz) of switching frequency (Van Dijk et al., 1995). Therefore, they are not preferred for applications where the high power density requirement is the primary concern.

1.3.2 SOFT-SWITCHING CONVERTERS

Soft-switching converters use the resonance feature of tank circuit to control the power flow in the circuit. Hence, these converters are also called as resonant converters (Steigerwald, 1984). These converters can facilitate the high-frequency operations by using the soft-switching mechanism. It can be either zero-voltage switching (ZVS) or zero-current switching (ZCS) operation (Liu and Lee, 1990, Hamada and Nakaoka, 2002). Due to soft-switching mechanism, the switching losses will reduce and hence, operation with high-switching frequency is possible. High-switching frequency operation leads to the advantages like small size, high power density, high efficiency and reduced EMIs in the resonant converters (Pilawa-Podgurski et al., 2009).

1.4 SOFT-SWITCHING MECHANISM

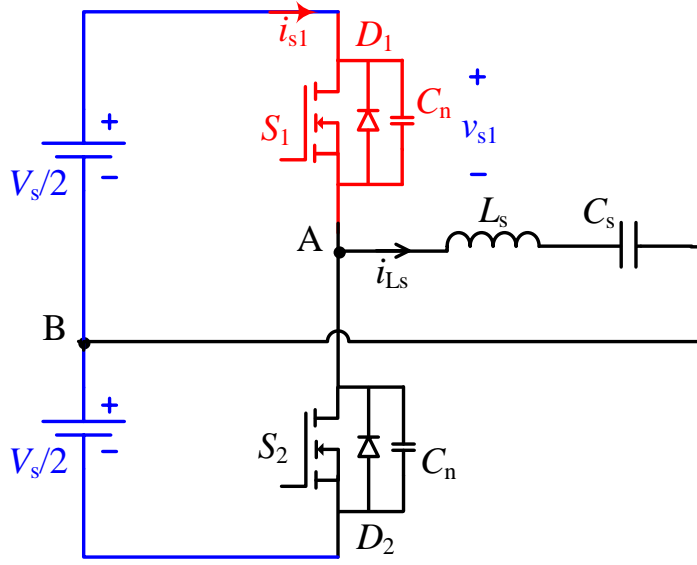
The semiconductor switches, whether diodes or transistors switching from off to on or vice versa takes a finite time due to parasitic elements involved in the circuit. Voltage across and current through the switches during this switching times depends on both the characteristics of the switches and the circuit connected to them. The existence of the voltage and current together in this finite switching times leads to power loss in switches. This power loss is not severe in low switching frequency operations. However, with high-frequency switching operations the power loss in the switches will be very significant and hence cannot be ignored. Therefore, soft-switching techniques are used to minimize the switching power losses (Canales et al., 2002). Soft-switching process involves turning on/off of a switch when either voltage or current is zero, hence the switching power loss is zero (Husev et al., 2015). This soft-switching process can be classified as following:

1. Zero Voltage Switching (ZVS)
2. Zero Current Switching (ZCS)

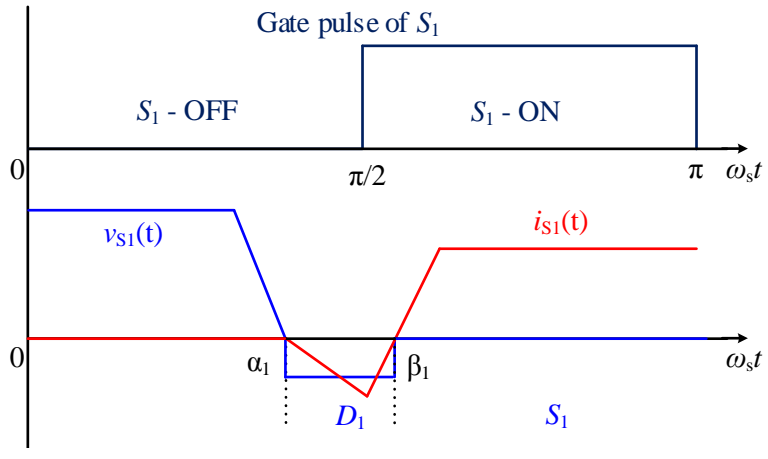
1.4.1 ZERO VOLTAGE SWITCHING (ZVS)

Resonant tank circuit elements i.e., inductance L and capacitance C are used to make the switch current sinusoidal. If the switch is turned on when the voltage across its terminals is zero, then zero-voltage switching (ZVS) is achieved (Steigerwald, 1984). To achieve ZVS, the converter has to be designed to operate in lagging pf mode. While operating the converter with switching frequency greater than the resonant frequency, the input impedance of resonant tank is predominantly inductive. Hence, the resonant/switch current (i_{L_s}) lags the inverter output voltage (v_{AB}). Therefore, designing the converter to operate in the above resonance/lagging pf mode results in ZVS of the converter switches (Liu and Lee, 1990, Jain et al., 2002).

In Fig.1.5, the ZVS phenomena is explained with the help of switch voltage (v_{s1}) and switch current (i_{s1}) waveforms for an example circuit of a half-bridge resonant converter. In Fig.1.5(b), at $\omega t = \alpha_1$, when the the voltage across switch S_1 (i.e., v_{s1}) tries to go to negative, the anti-parallel diode D_1 gets forward biased which makes the switch current i_{s1} negative. Now at $\omega t = \beta_1$, when the diode current just becomes zero,



(a)



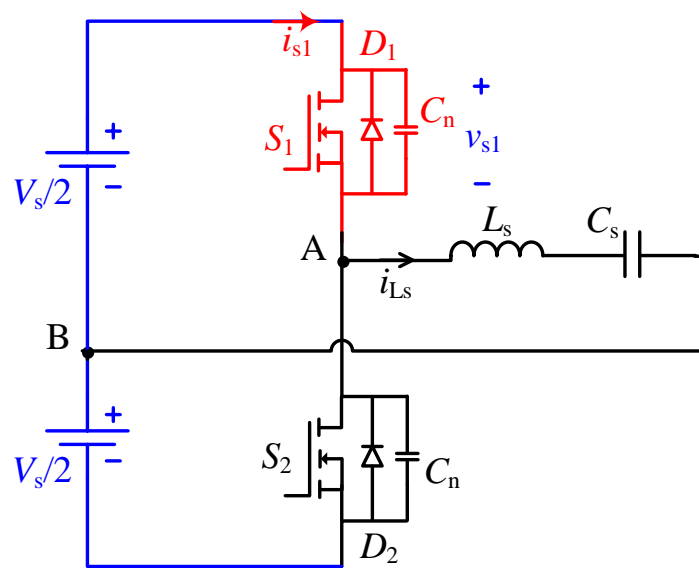
(b)

Figure 1.5: ZVS phenomena: (a) Circuit diagram of half-bridge resonant converter, (b) Waveforms of voltage across and current through switch S_1 .

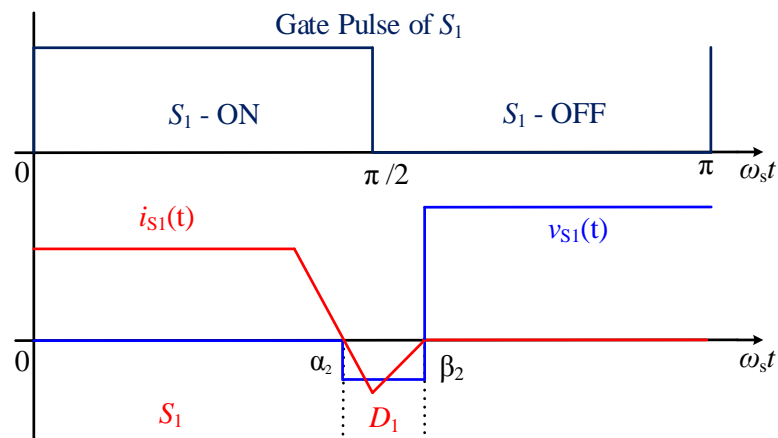
since there is already a gating signal applied to S_1 , the switch S_1 starts conducting. Hence, ZVS of switch S_1 is achieved. Therefore, in above resonance mode, the switch conducts after the anti-parallel diode, that results in minimum switching losses at turn-on.

1.4.2 ZERO CURRENT SWITCHING (ZCS)

Resonant tank circuit elements i.e., inductance L and capacitance C are used to make the switch current sinusoidal. If the switch is turned off when the current through its terminals is zero, then zero current switching (ZCS) is achieved (Steigerwald, 1985). To achieve ZCS, the converter has to be designed to operate in leading pf mode. While operating the converter with switching frequency less than the resonant



(a)



(b)

Figure 1.6: ZCS phenomena: (a) Circuit diagram of half-bridge resonant converter, (b) Waveforms of voltage across and current through switch S_1 .

network frequency, the input impedance of resonant tank is predominantly capacitive. Hence, the resonant/switch current (i_{Ls}) leads the inverter output voltage (v_{AB}) (Chien-Ming Wang, 2005). Therefore, designing the converter to operate in the below resonance/leading pf mode results in ZCS of the converter switches (Bo-Tao Lin et al., 1999, Shu et al., 2018).

In Fig.1.6, the ZCS phenomena is explained with the help of switch voltage (v_{s1}) and switch current (i_{s1}) waveforms for an example circuit of a half-bridge resonant converter. In Fig.1.6(b), at $\omega t = \alpha_2$, when the the current through switch S_1 (i.e., i_{s1}) tries to go to negative, the anti-parallel diode D_1 gets forward biased which makes the switch current i_{s1} negative. Therefore, at $\omega t = \alpha_2$, the switch S_1 turns-off before its gating signal is removed. Hence, ZCS of switch S_1 is achieved. Therefore, in below resonance mode, the switch conducts before the anti-parallel diode, that results in minimum switching losses at turn off.

1.5 MOTIVATION OF THIS WORK

The PWM converters are not preferred in high power density applications as their operation is limited to a few kHz of frequency due to hard switching. Resonant power converters are likely to be operated with high-frequency due to soft-switching mechanisms and have advantages like small size, high power density, high efficiency and reduced EMIs. Hence, resonant power converters are preferred in renewable energy applications as compared to PWM converters. The exhaustive literature survey on resonant power converter topologies, modeling, analysis and design of resonant power converters for variable load and variable input voltage applications with different control methods have been done and the findings are presented.

1.6 PROBLEM STATEMENT

To find a suitable high-frequency transformer isolated, fixed-frequency controlled, soft-switching DC-DC power converter topology that can be used in solar power generation applications and investigate on its performance, with different gating schemes.

1.7 THESIS ORGANIZATION

The whole thesis is organized into six chapters as follows,

Chapter 1: A brief introduction to the DC-DC power converters and soft-switching mechanisms are discussed in this chapter.

Chapter 2: Soft-switching converter topologies, power controlling methods, steady-state analysis methods, identified research gaps and research objectives are discussed in this chapter.

Chapter 3: The fixed-frequency based phase-shift control scheme is proposed for LCL-T resonant converter. The steady-state analysis of converter is carried using fundamental harmonic analysis (FHA) method. The simulation and experimental performances of proposed phase-shift control scheme are discussed in this chapter.

Chapter 4: The Fourier series based analysis and design of fixed-frequency modified gating scheme controlled LCL-T resonant converter is proposed in this chapter. The steady-state analysis of resonant power converter is carried using Fourier series analysis (FS) method. The simulation and experimental performances of proposed modified gating scheme are discussed in this chapter. Also, the proposed control scheme is comprehensively compared with conventional phase-shift control scheme.

Chapter 5: The small-signal modeling of the converter using extended describing function (EDF) method is performed in this chapter. This can be used for study the dynamic behavior of the converter.

Chapter 6: This chapter concludes the contributions of the proposed research work and also discusses about scope for the possible future works.

Chapter 2

LITERATURE REVIEW

Contents

2.1	RESONANT POWER CONVERTER TOPOLOGIES .	12
2.1.1	TWO-ELEMENT RC TOPOLOGIES	14
2.1.2	THREE-ELEMENT RC TOPOLOGIES	14
2.2	POWER CONTROLLING METHODS	16
2.2.1	VARIABLE-FREQUENCY CONTROL	16
2.2.2	FIXED-FREQUENCY CONTROL	18
2.3	ANALYSIS METHODS	18
2.3.1	STEADY-STATE ANALYSIS	19
2.3.2	TRANSIENT ANALYSIS	19
2.4	IDENTIFIED RESEARCH GAPS	21
2.5	RESEARCH OBJECTIVES	21

The detailed literature review of the resonant power converter topologies, power control methods, and the analysis methods are presented in this chapter. Also, the main objectives of this research work are given in this chapter.

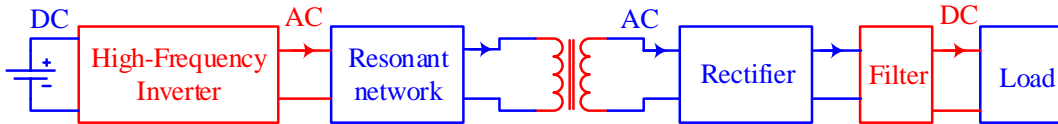


Figure 2.1: Basic structure of DC-DC isolated resonant power converter.

2.1 RESONANT POWER CONVERTER TOPOLOGIES

Resonant power converters can facilitate soft-switching operation (i.e., zero-voltage switching (ZVS) or zero-current switching (ZCS)) of inverter switches. Due to soft-switching operation, the switching losses will reduce and hence, operation with high-frequency (HF) is possible (Steigerwald, 1984). High-frequency operation leads to the advantages like high power density, high efficiency, small size and reduced EMIs in the resonant converters (Tan and Ruan, 2016, Outeiro et al., 2016). high-frequency operated converters are being widely used in applications like induction heating (Husev et al., 2015), energy storage (Kanamarlupudi et al., 2018), renewable energy source (RES) (York et al., 2013, Seok et al., 2018), and hybrid electric vehicles (HEV) (Outeiro et al., 2016, Saeed, 2018) due to their small size and high power density (Jiang et al., 2020).

The basic structure of any isolated resonant power converter shown in Fig. 2.1 consists of high-frequency (HF) switched inverter, resonant network, HF transformer, diode rectifier and filter. Energy generated by the solar photovoltaics (or any renewable energy source) is given as the DC input to the HF switched DC to AC converter (i.e., inverter). The HF inverter output is given to the resonant circuit which consists of different combinations of resonant inductor (L) and resonant capacitor (C) elements. The primary of HF transformer is connected to the output of resonant circuit and secondary side is connected to the AC to DC converter (i.e., rectifier). The rectifier output is connected to the load through a filter which removes the ripples in DC output of the rectifier. The circuit of HF inverter/output rectifier can be of 1-phase/3-phase either half-bridge or full-bridge depending on the power requirements. The resonant network can be of either two-element or three-element or more element network based on the choice of suitable topology. The filters can have com-

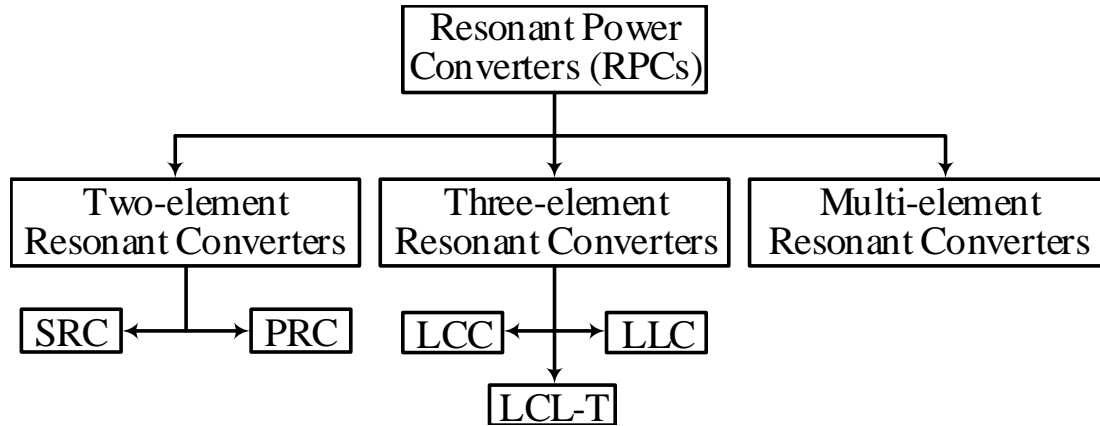


Figure 2.2: Classification of resonant power converters.

bination of C , L or LC depending on the design considerations. The DC output of the DC-DC resonant converter has to be finally inverted to supply either standalone line-frequency AC loads or for grid-interfacing.

The classification of resonant power converter topologies is given in Fig. 2.2. This classification is done based on the number of resonant elements (i.e., inductors and capacitors) are connected in resonant tank network (Severns, 1990, Bhat and Dewan, 1989), (Salem et al., 2018). Namely,

1. Two-element resonant converter topologies
2. Three-element resonant converter topologies

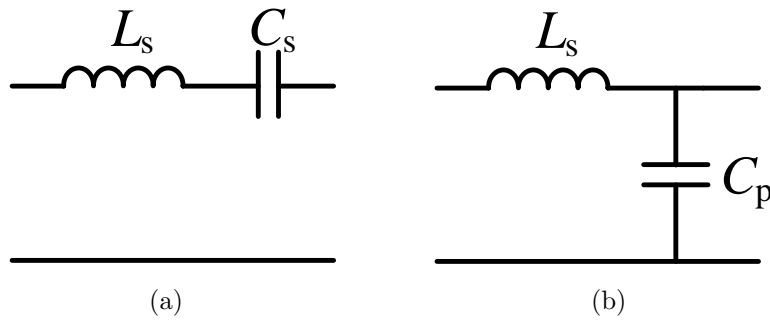


Figure 2.3: Two-element resonant converter topologies

2.1.1 TWO-ELEMENT RC TOPOLOGIES

Two element resonant converters shown in Fig. 2.3 are the basic converter topologies in resonant converter family. The combination of inductor (L_s) and capacitor (C_s) in series as shown in Fig. 2.3(a) is called series resonant converter (SRC) (King and Stuart, 1981). The limitations of SRC are difficulty in no-load voltage regulation and unavailability of load short circuit protection.

The connection of inductor (L_s) and capacitor (C_p) elements in resonant network as shown in Fig. 2.3(b) is called as parallel resonant converter (PRC) (Ranganathan et al., 1982). The main concern in the PRC is that the peak currents do not reduce with load, hence poor part-load efficiency (Amjad and Salam, 2014).

2.1.2 THREE-ELEMENT RC TOPOLOGIES

Three element resonant converters shown in Fig. 2.4 were proposed in the literature to overcome the limitations of two-element resonant converter topologies.

The PRC after connection of an additional series capacitor (C_s) (with L_s) in the

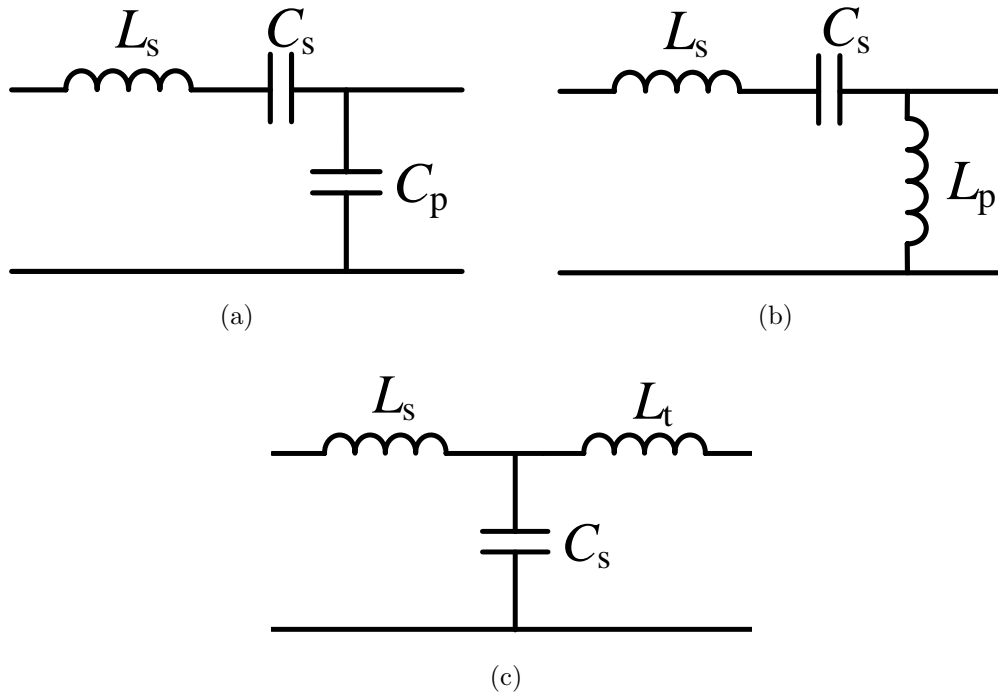


Figure 2.4: Three-element resonant converter topologies

Table 2.1: Resonant power converter topologies

#	Reference	Remarks
1	(j. King and Stuart, 1982)	Full-bridge series resonant converter (SRC) is proposed. The voltage regulation of converter is limited.
2	(Johnson and Erickson, 1988)	Parallel resonant converter (PRC) is proposed. The part-load efficiency with this topology is poor.
3	(Bhat, 1991b)	Analysis and design of a series-parallel (LCC) resonant converter with capacitive output filter.
4	(Steigerwald, 1988)	The half-bridge series-resonant, parallel-resonant, and combination series-parallel resonant converters are compared for use in low output voltage power supply applications.
5	(Bhat, 1992)	A series-parallel (LCC) resonant converter with inductive output filter is proposed.
6	(Bhat, 1990)	The modified series or LCL type resonant converter is proposed.
7	(Gautam and Bhat, 2013)	This paper presents the design of three soft-switched high-frequency transformer isolated dc-to-dc converters for electrolyzer application. It is shown that LCL-type series resonant converter (SRC) with capacitive output filter is suitable for this application.
8	(Fu et al., 2008)	The LC filter (i.e., notch filter) is connected on primary side of the LCL converter to protect from load short circuit. Hence, increases the cost and complexity of the system.
9	(Wu et al., 2016)	The notch filter is also connected on secondary side of the LCL converter. Therefore it also increases the cost and complexity of the system.
10	(Gao et al., 2017)	A new multioutput LLC resonant converter with a semi-active rectifier (SAR) is proposed for high-efficiency multiple-output applications.

resonant network as shown in Fig. 2.4(a) is named as series-parallel (LCC) resonant converter (Bhat and Dewan, 1987). LCC type resonant converter incorporates benefits of both SRC and PRC. However, the limitation of poor part-load efficiency remains as PRC in the LCC-type resonant converter (Yang et al., 2014).

The SRC after inclusion of an additional inductor (L_p) as shown in Fig. 2.4(b) is named as modified SRC or LCL-type resonant converter (Kojori et al., 1991, Bhat, 1991a). LCL resonant converter has been the most popular and widely used configuration in different applications since it overcomes the limitations that occur in the SRC and LCC type converter topologies (Liu and Lee, 1992). Though LCL converter is preferred, it does not have built-in protection against load short circuit. When the load is short-circuited, currents higher than the rated value flows through the inverter switches due to resonance. Hence, it causes damage to inverter bridge and power supply (Feng and Lee, 2014).

In (Chakraborty et al., 1999), an inductor (L_t) connected after PRC as shown in Fig. 2.4(c) was proposed and it was named as series-parallel LCL-T type resonant converter, since three resonant elements in resonant tank are connected in T-shape. It has the benefits of LCC and LCL type resonant converters and additionally provides the load short circuit protection without adding any additional element.

2.2 POWER CONTROLLING METHODS

The power controlling methods are essential to control the power flow in the circuit. The following two power controlling methods are commonly being used in resonant power converter topologies.

1. Variable-frequency Control
2. Fixed-Frequency Control

2.2.1 VARIABLE-FREQUENCY CONTROL

In variable frequency control, the frequency (i.e., changing either T_{on} or T_{off} of gating signals) is changed to regulate the output voltage in the case of changes in load and input voltage (Grigorova and Vuchev, 2018). However, variable frequency control leads to difficulty in designing the filters and other magnetics. When below resonant

Table 2.2: Resonant power converter power controlling methods

#	Reference	Remarks
1	(Chakraborty et al., 1999)	The LCL-T type resonant converter is controlled using variable frequency control scheme.
2	(Borage et al., 2009)	The fixed-frequency asymmetrical duty cycle (ADC) control scheme is used. It can resolve the problems associated with variable frequency control scheme. But, switch utilization is less in ADC control and voltage regulation range is limited.
3	(Yang et al., 2016)	A variable duty cycle soft startup strategy based on optimal current-limiting curve is presented, which can realize the suppression of the resonant current inrush under low startup frequency.
4	(Shakib and Mekhilef, 2017)	A Frequency Adaptive Phase shift Modulation Control of LLC converter is proposed. Adaptive frequency control is used to secure ZVS in the primary bridge with regards to load change. But, phase shift control loses the ZVS for two switches at maximum input voltage.
5	(Bhowmick and Bhat, 2014)	A fixed-frequency series parallel LCC converter with inductive output filter using a modified gating scheme (MGS) is proposed. Only one switch loses ZVS using MGS control compared to conventional gating scheme.
6	(Fei et al., 2017)	This paper proposes a method to implement soft start-up and short-circuit protection for LLC converters by using low-cost microcontrollers (MCUs) with minimum stresses and optimal energy delivery.

frequency operation takes place, at light load the switching frequency becomes too low which results in the need for increase in the size of magnetics and the filters for effective filtering. When above resonant frequency operation takes place, at light load the switching frequency becomes very high, which increases the magnetic losses.

2.2.2 FIXED-FREQUENCY CONTROL

In fixed-frequency control, the duty ratio (i.e., the ratio of T_{on}/T) is changed to regulate the output voltage in the case of changes in load and input voltage while keeping the frequency of the gating signal constant (Sun et al., 2017). Fixed-frequency control technique minimizes the difficulties that occur in variable-frequency control i.e., complexity in design of magnetic components and filters for effective filtering. Also, the size of the converter can be reduced by designing the converter with a constant high-frequency (HF) (both in above or below resonance operation) (Asa et al., 2015).

Different fixed-frequency control schemes are available in the literature to control the power flow in the resonant converters. Asymmetrical duty cycle (ADC) control is the basic method in fixed-frequency control of power electronics converters (Redl, 1996). ADC control delivers the unsymmetrical inverter output voltage due to unequal switching signals (Kranprakon et al., 2016, Zong et al., 2016). Due to unsymmetrical inverter output voltage, high-frequency transformer gets saturated easily. Hence, it is necessary to connect a series capacitor in resonant circuit. This is one of the disadvantages with this ADC control. Also, switches in inverter bridge with ADC control are under-utilized (Lucia et al., 2009). A fixed-frequency phase-shifted gating (PSG) control scheme does not require a series capacitor unlike in ADC control (Du and Bhat, 2016). However, this PSG control using the regular 180° wide gating signals when applied to the inverter results in two switches losing ZVS with maximum input voltage (Shi et al., 2016). Also, two zero voltage intervals occur in the inverter output voltage. Fixed-frequency modified gating scheme (MGS) (Hamdad and Bhat, 2001) results in loss of ZVS for only one switch when operated with maximum input voltage (Harischandrapa and Bhat, 2014). Further, only one zero voltage interval occurs in the inverter output voltage as compared to two such intervals in PSG control (Chen and Bhat, 2016).

2.3 ANALYSIS METHODS

The complete behavior of the resonant converters at different intervals of the operation can be predicted by analyzing the converter circuit in steady-state and transient state.

2.3.1 STEADY-STATE ANALYSIS

Different steady-state analysis methods are available to analyze the resonant converters. Namely, differential equations (DEs) method (Ranganathan et al., 1982), fundamental harmonic Approximation (FHA) method, and Fourier series (FS) method (Bhat and Dewan, 1989). DEs method is the most complex to apply and solve (Johnson and Erickson, 1988). FHA method is simple and easy to apply. But, it considers only fundamental components in the voltage and current waveforms neglecting all higher order harmonics. Hence, this method cannot predict the performance more accurately. Accuracy reduces as the switching frequency is away from the designed value since the sinusoidal approximation does not hold good at light loads. However, this method is used in the literature for quick analysis. Also, this FHA method gives a simple design procedure. Fourier series method considers all the harmonic components in voltage and current waveforms (Li and Bhat, 2012, Bhat and Zheng, 1996). Hence, this method provides accurate and efficient results as compared to the FHA analysis method where, only fundamental component is considered.

2.3.2 TRANSIENT ANALYSIS

In order to understand the complete behavior of the converter for fluctuations in the input voltage, load, and control parameters, small-signal modeling of the converter is essential (Agarwal et al., 1997). State space average technique is the most popular approach for modeling of PWM converters (Mahdavi et al., 1997, Davoudi and Jatskevich, 2007). It provides simple and accurate solutions. This method cannot be applied for modeling of resonant converter when the switching frequency is close to resonant frequency (Witulski and Erickson, 1990, Green, 1993). Sample-data method also used in (Elbuluk et al., 1988, Mandal et al., 2015) for modeling the resonant converters. When the number of elements used in resonant tank increases (third order or more), the sample-data method is difficult to apply (Abbasi et al., 2019). All these modeling techniques involved time domain analysis and derived in discrete time model (Agarwal and Bhat, 1995). Therefore, it is difficult to use in the compensator design (Martin-Ramos et al., 2002). In order to improve the accuracy, a model in both frequency-domain and time-domain is obtained. Extended describing function (EDF) method combines both time-domain and frequency-domain analyses (Ayachit et al., 2012). Using EDF method, it is easy to derive all small-signal transfer functions

Table 2.3: Resonant converter steady-state and transient state analysis methods

#	Reference	Remarks
1	(j. King and Stuart, 1982)	A steady state model is derived for the full-bridge series-resonant power converter using differential equations method
2	(Bhat, 1991)	Complex ac circuit analysis method is used to analyze the resonant converter in steady-state
3	(Harischandrappa and Bhat, 2014)	Steady-state analysis of the LCL resonant converter using approximate complex ac circuit analysis method is presented.
4	(Bhat, 1995b)	Two-port model based Fourier-series approach is proposed for steady-state analysis of LCL-type resonant converter
5	(Du and Bhat, 2014)	The Fourier series analysis of dual tank LCL converter is proposed
6	(Buccella et al., 2015)	A nonlinear model for the LLC resonant converter was developed using the EDF method; then, based on the derived model, a nonlinear observer-based controller was designed and implemented with a DSP micro-controller.
7	(Tahavorgar and Quaicoe, 2019)	The small-signal model of the converter is derived from the EDF analysis. Frequency-domain analysis is then employed to derive the small-signal transfer functions of the converter.
8	(Tahavorgar and Quaicoe, 2017)	Small-signal analysis of a dual series resonant dc-dc converter is derived using EDF method.
9	(Yang et al., 1992)	Small-signal modeling of LCC resonant converter using EDF concept.

like output control-to-output, input voltage-to-output, frequency-to-output, and duty ratio-to-output. A single loop voltage feedback control is developed to regulate the output voltage for variations in the input voltage and the load.

2.4 IDENTIFIED RESEARCH GAPS

After the thorough literature survey on resonant converters, it is found that load short circuit protection is a concern in the resonant converters. When the load is short-circuited, higher current (beyond the rated value) flows through the inverter switches due to the near resonance operation. This causes damage to inverter switches and hence the reliability of power supply reduces. Therefore, short circuit protection is necessary for the safety of devices and the system. To resolve the load short circuit problem in resonant converters, auxiliary circuits like notch filter on primary side and secondary side and optimal trajectory control methods are used. These auxiliary circuits make the system bulky and increase the cost of the converter. A series-parallel LCL-T type of resonant converter has an inherent load short-circuit protection capability without using any additional components. Therefore, it is worth to extend the research in developing the LCL-T type resonant converter. Fixed-frequency controlled LCL-T type resonant converter is not available in the literature.

From the literature, it is observed that, fixed-frequency control can overcome the difficulties in design of magnetic components and filters that occur with variable frequency control. Therefore, it is worth to investigate the performance of LCL-T type resonant converter by operating with the fixed-frequency control schemes.

2.5 RESEARCH OBJECTIVES

The main objective of this research is to find a suitable DC-DC resonant power converter topology that can be used in solar power generation applications and investigate on its performance. In this regard, the following objectives are set:

1. To propose fixed-frequency control technique for the LCL-T type of DC-DC resonant converter and perform the following:
 - (i). Mathematical modeling,
 - (ii). Steady-state analysis,
 - (iii). Design, and
 - (iv). Simulations
2. To build an experimental model of the converter designed in objective#1.

3. To propose modified gating scheme control for the converter designed in objective#1 and compare the performance.
4. To study the dynamic behavior of the converter designed in objective#1 by performing small signal analysis.

Chapter 3

PHASE-SHIFTED GATING SIGNAL CONTROLLED LCL-T RESONANT POWER CONVERTER

Contents

3.1	CIRCUIT DESCRIPTION	24
3.2	OPERATING PRINCIPLE OF PSG CONTROL	27
3.2.1	OPERATING MODES	27
3.3	STEADY-STATE ANALYSIS	30
3.3.1	MODELING	31
3.3.2	ANALYSIS	34
3.3.3	ZVS CONDITIONS	36
3.4	DESIGN	37
3.4.1	DESIGN TRADE-OFFS	39
3.4.2	DESIGN SUMMARY	40
3.5	SIMULATION RESULTS	40
3.6	EXPERIMENTAL RESULTS	47
3.7	SUMMARY	52

In this Chapter, a fixed-frequency phase-shifted gating (PSG) signal controlled LCL-T type of resonant power converter is discussed. The converter is designed to operate in lagging pf mode to ensure zero-voltage switching (ZVS) of the inverter switches. Fundamental harmonic approximation (FHA) method is used to analyze the converter in steady-state.

3.1 CIRCUIT DESCRIPTION

The circuit diagram of full-bridge single-phase LCL-T resonant converter is shown in Fig. 3.1. The DC output of renewable energy source (i.e., photovoltaics) is given to the full-bridge inverter which produces the ac output voltage. The high-frequency (HF) ac output voltage of inverter is given to the resonant tank circuit which is formed using resonant inductor (L_s), resonant capacitor (C_s), and inductor (L) elements. A HF transformer of $1:n_t$ turns ratio is connected between the resonant circuit and the output diode rectifier. A capacitive output filter is used to absorb the current ripples from entering the load. Since the resonant tank elements L_s , C_s , and L are arranged

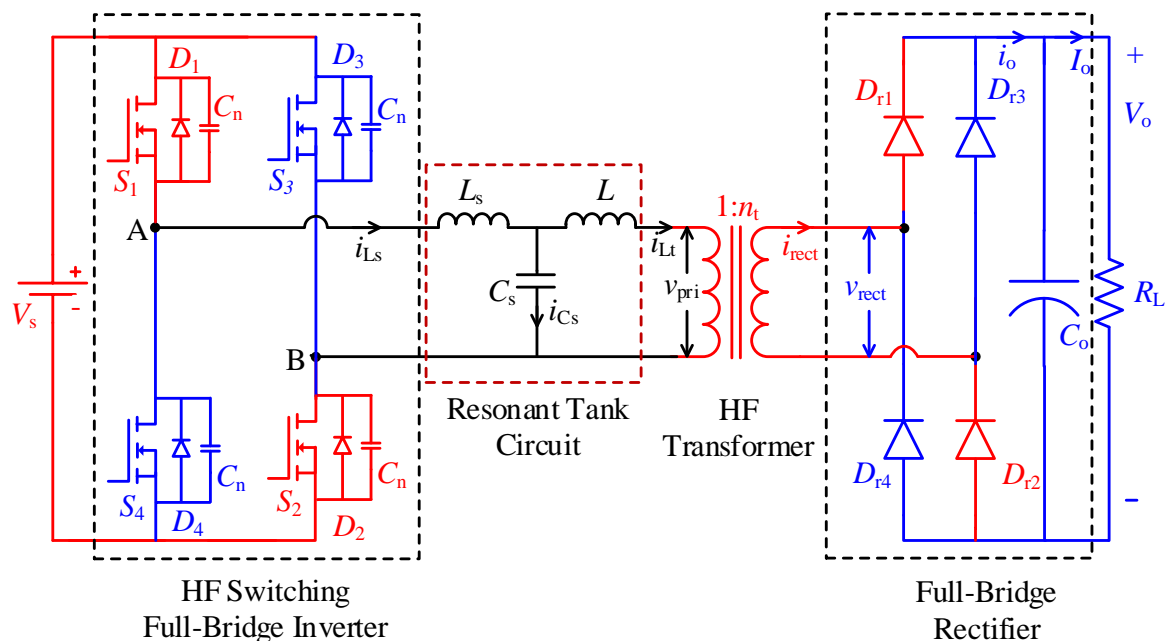


Figure 3.1: Circuit diagram of single-phase full-bridge LCL-T resonant power converter.

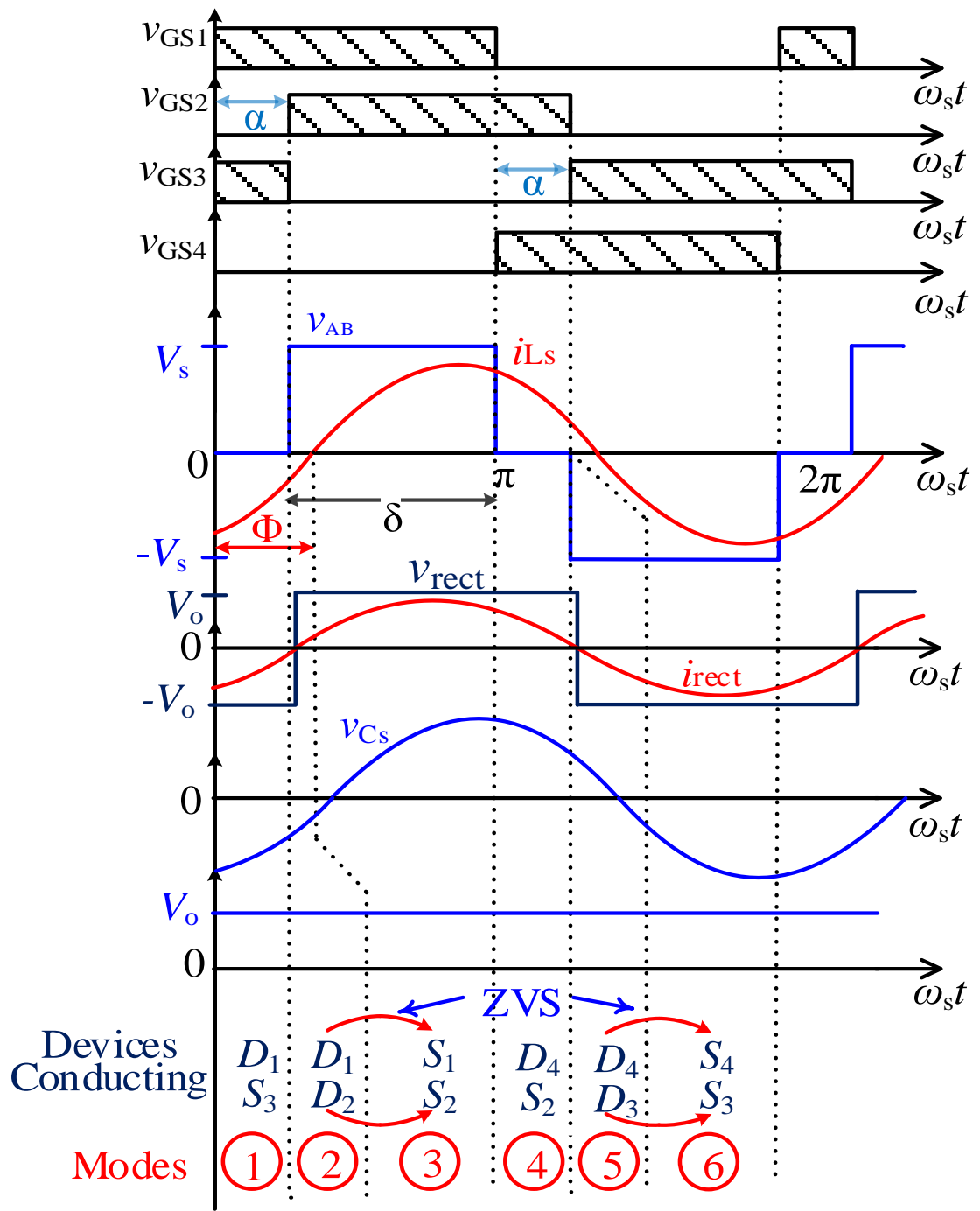


Figure 3.2: Typical operating waveforms of the proposed phase-shift controlled LCL-T converter.

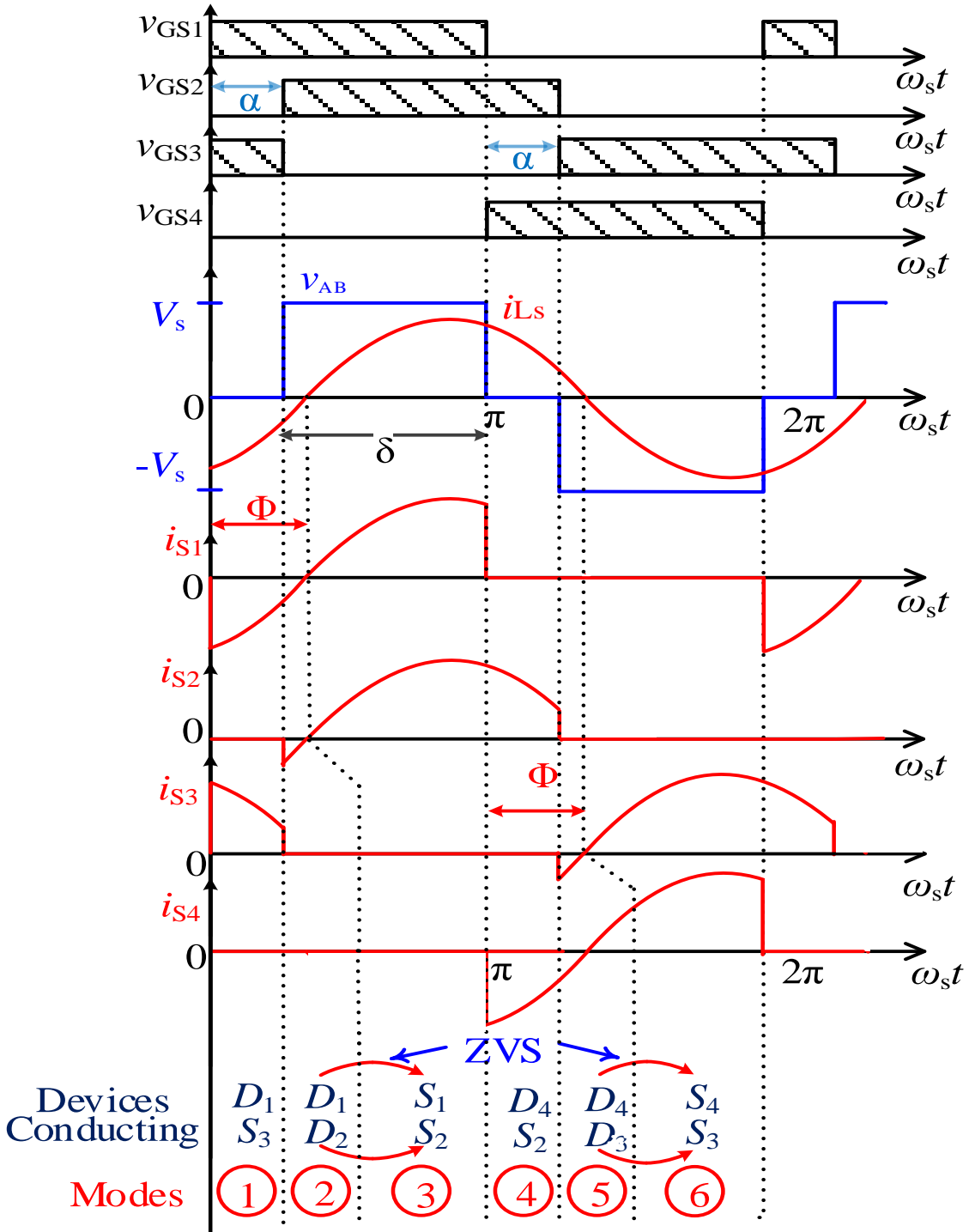


Figure 3.3: Typical operating switching waveforms of the proposed phase-shift controlled LCL-T converter.

in ‘T’ shape, it is named as LCL-T type converter. The inductor, ‘ L ’ protects the circuit when the load is short-circuited. MOSFET’s are used as switches (S_1 - S_4) in full-bridge inverter circuit since the operating switching frequency is in the range of several kHz. The switching frequency is selected such that the converter operates with lagging pf to achieve ZVS for switches in inverter bridge.

3.2 OPERATING PRINCIPLE OF PSG CONTROL

The typical operating and switching waveforms of the proposed fixed-frequency phase-shifted gating (PSG) control scheme are given in Figs. 3.2 and 3.3. The main aim of operating this converter is to maintain output voltage (V_o) for input voltage (V_s) and load (R_L) variations. The pulse width (δ) of the inverter output voltage v_{AB} is varied to maintain the V_o constant. The variation of δ ($= \pi - \alpha$) depends on phase-shift angle (α) between the switching signals of inverter switches as shown in Fig. 3.2. The phase-shift angle α is obtained by shifting the switching signals of the lagging leg switches, i.e., S_2 and S_3 with respect to that of the leading leg switches, i.e., S_1 and S_4 respectively. This angle α is varied for maintaining the output voltage constant for changes in the input voltage and the load.

3.2.1 OPERATING MODES

Different operating modes of LCL-T resonant converter circuit of Fig. 3.1 are presented in Fig. 3.4. For the gating signals shown in Fig. 3.2, there are six different operating modes possible. These modes are identified based on the devices conducting. Each mode of operation is described using the equivalent circuits in the following subsections.

3.2.1.1 Mode-1 ($S_3, D_1 = \text{ON}$)

In this mode, devices S_3 and D_1 conduct while the remaining are all off. Before this mode (i.e., in mode-6), the gating signals for S_4 and S_3 are high which makes S_4 and S_3 to conduct. At the end of mode-6, the gating signal for S_4 is removed. But since, current through resonant inductor cannot alter instantly, the path is provided by the diode D_1 . Hence, in mode-1, S_3 continues to conduct, while D_1 starts conducting.

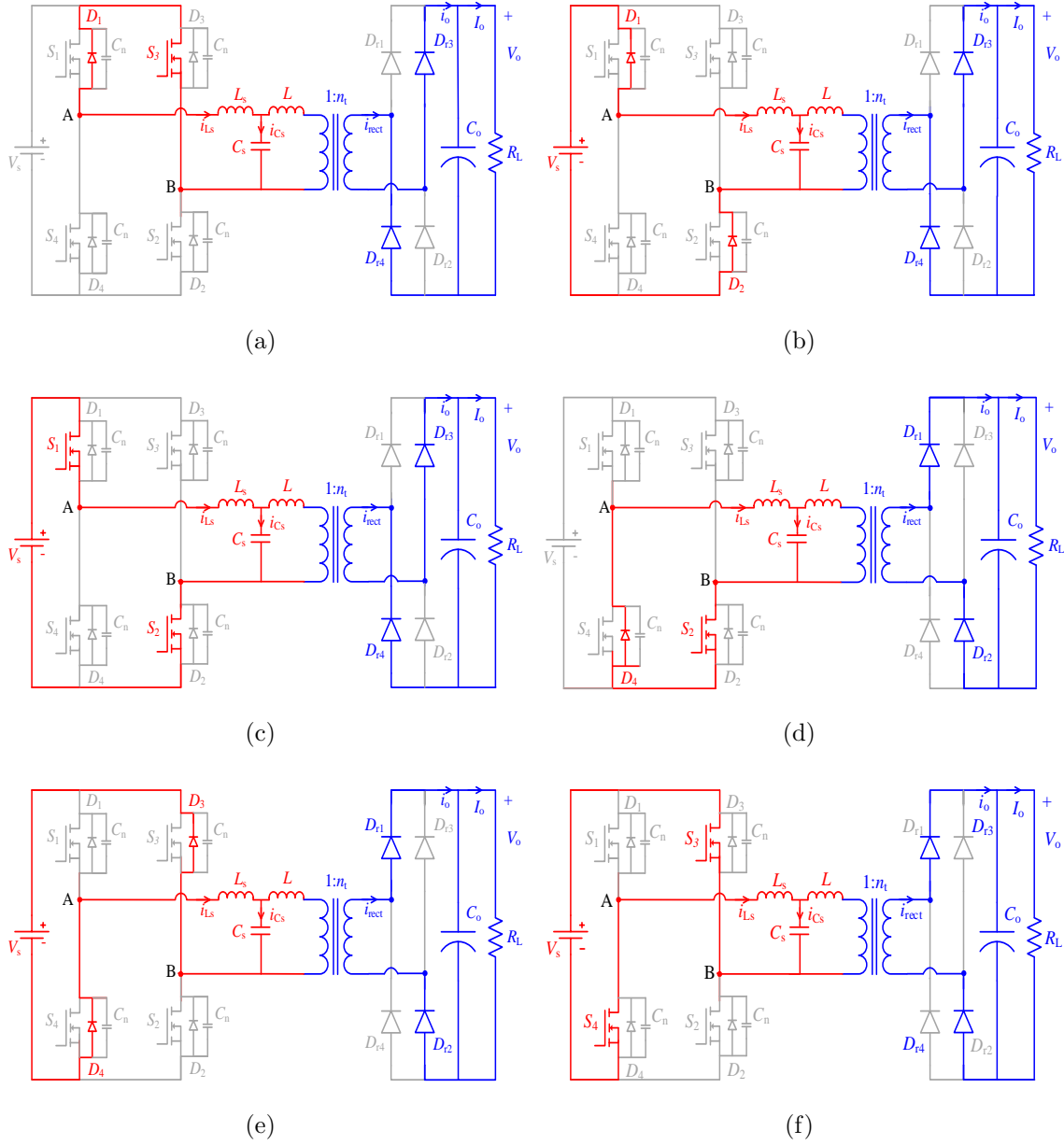


Figure 3.4: Equivalent circuits of LCL-T converter operating in: (a) mode-1 ($S_3, D_1 = \text{ON}$), (b) mode-2 ($D_1, D_2 = \text{ON}$), (c) mode-3 ($S_1, S_2 = \text{ON}$), (d) mode-4 ($S_2, D_4 = \text{ON}$), (e) mode-5 ($D_4, D_3 = \text{ON}$), (f) mode-6 ($S_4, S_3 = \text{ON}$)

This makes the voltage at inverter output terminals (v_{AB}) zero. The resonant current (i_{Ls}) takes the path S_3 - resonant circuit - D_1 as indicated in Fig. 3.4(a). In output rectifier block, diodes D_{r3} and D_{r4} conduct, while the output voltage remains constant. The rectifier diodes D_{r1} and D_{r2} are clamped to output voltage (V_o).

3.2.1.2 Mode-2 ($D_1, D_2 = \text{ON}$)

In this mode, devices D_1 and D_2 conduct while the remaining are all off. Before this mode (i.e., in mode-1), the gating signals for S_3 and S_1 are high and, S_3 and D_1 conduct. At the end of mode-1, the gating signal for S_3 is removed. But since, current through resonant inductor cannot alter instantly, the path is provided by the diode D_2 . Hence, in this mode D_1 continues to conduct, while D_2 starts conducting. This makes the voltage at inverter output terminals, $v_{AB} = +V_s$. The resonant current (i_{Ls}) takes the path V_s - D_2 - resonant circuit - D_1 - V_s as indicated in Fig. 3.4(b). In output rectifier block, diodes D_{r3} and D_{r4} conduct, while the output voltage remains constant. The rectifier diodes D_{r1} and D_{r2} are clamped to output voltage (V_o).

3.2.1.3 Mode-3 ($S_1, S_2 = \text{ON}$)

In this mode, devices S_1 and S_2 conduct while the remaining are all off. Before this mode (i.e., in mode-2), the gating signals for S_1 and S_2 are high and, D_1 and D_2 conduct. At the end of mode-2, the resonant current crosses zero and becomes positive. This makes the S_1 and S_2 to conduct with ZVS. The voltage at inverter output terminals, $v_{AB} = +V_s$. The resonant current (i_{Ls}) takes the path V_s - S_1 - resonant circuit - S_2 - V_s as indicated in Fig. 3.4(c). In output rectifier block, diodes D_{r3} and D_{r4} conduct, while the output voltage remains constant. The rectifier diodes D_{r1} and D_{r2} are clamped to output voltage (V_o).

3.2.1.4 Mode-4 ($S_2, D_4 = \text{ON}$)

In this mode, devices S_2 and D_4 conduct while the remaining are all off. Before this mode (i.e., in mode-3), the gating signals for S_1 and S_2 are high which makes S_1 and S_2 to conduct. At the end of mode-3, the gating signal for S_1 is removed. But since, current through resonant inductor cannot alter instantly, the path is provided by the diode D_4 . Hence, in this mode S_2 continues to conduct, while D_4 starts conducting. This makes the voltage at inverter output terminals (v_{AB}) zero. The

resonant current (i_{Ls}) takes the path D_4 - resonant circuit - S_2 as indicated in Fig. 3.4(d). In output rectifier block, diodes D_{r1} and D_{r2} conduct, while the output voltage remains constant. The rectifier diodes D_{r3} and D_{r4} are clamped to output voltage (V_o).

3.2.1.5 Mode-5 ($D_4, D_3 = \text{ON}$)

In this mode, devices D_4 and D_3 conduct while the remaining are all off. Before this mode (i.e., in mode-4), the gating signals for S_2 and S_4 are high and, S_2 and D_4 conduct. At the end of mode-4, the gating signal for S_2 is removed. But since, current through resonant inductor cannot alter instantly, the path is provided by the diode D_3 . Hence, in this mode D_4 continues to conduct, while D_3 starts conducting. This makes the voltage at inverter output terminals $v_{AB} = -V_s$. The resonant current (i_{Ls}) takes the path $V_s - D_4$ - resonant circuit - $D_3 - V_s$ as indicated in Fig. 3.4(e). In output rectifier block, diodes D_{r1} and D_{r2} conduct, while the output voltage remains constant. The rectifier diodes D_{r3} and D_{r4} are clamped to output voltage (V_o).

3.2.1.6 Mode-6 ($S_4, S_3 = \text{ON}$)

In this mode, devices S_4 and S_3 conduct while the remaining are all off. Before this mode (i.e., in mode-5), the gating signals for S_4 and S_3 are high and, D_4 and D_3 to conduct. At the end of mode-5, the resonant current crosses zero and becomes negative. This makes the S_4 and S_3 to conduct with ZVS. The voltage at inverter output terminals, $V_{AB} = -V_s$. The resonant current (i_{Ls}) takes the path $V_s - S_3$ - resonant circuit - $S_4 - V_s$ as indicated in Fig. 3.4(f). In output rectifier block, diodes D_{r1} and D_{r2} conduct, while the output voltage remains constant. The rectifier diodes D_{r3} and D_{r4} are clamped to output voltage (V_o).

3.3 STEADY-STATE ANALYSIS

Fundamental harmonic approximation (FHA) method is used to analyze the proposed phase-shifted gating controlled LCL-T converter in steady-state. The assumptions made in the analysis are follows:

- (i) All elements including the semiconductors and magnetics are ideal.

- (ii) All harmonics other than fundamental are neglected.
- (iii) T- equivalent circuit of the high-frequency (HF) transformer is used.
- (iv) The current in the magnetizing inductance of HF transformer is negligible.

3.3.1 MODELING

In Fig. 3.5(a), the converter circuit of Fig. 3.1 is redrawn by referring to the primary side of the HF transformer at the output terminals of the inverter (A, B). Since, the magnetizing inductance draws a low current, to simplify the circuit reduction, L_m is shown as open circuit in Fig. 3.5(b), where, $L_t (= L_1 + L'_2 + L)$. The resistance R_{ac} is used to equivalently represent the diode rectifier, filter capacitance, and the load in Fig. 3.5(c). The important steps required in obtaining the expression for R_{ac} are described below:

The input voltage and current (v'_{rect} , i'_{rect}) waveforms of the diode rectifier of Fig. 3.5(b) are shown in Fig. 3.6.

The rectifier input voltage (v'_{rect}) can be obtain using Fourier series as follows (Refer Appendix-A, (A.4)):

$$v'_{rect}(t) = \sum_{n=1,3,5..}^{\infty} \frac{4V'_o}{\pi} \sin(n\omega_s t) \quad (3.1)$$

The fundamental component of $v'_{rect}(t)$ (i.e., $n = 1$) is

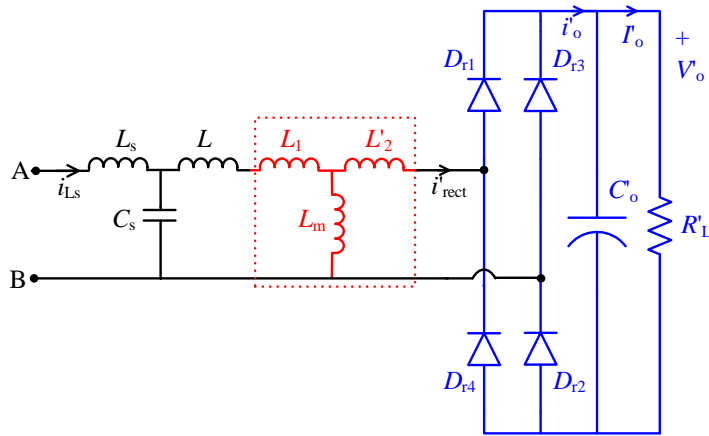
$$v'_{rect1}(t) = \frac{4V'_o}{\pi} \sin(\omega_s t) \quad (3.2)$$

Therefore, the peak value of (3.2) (i.e., $\omega t = \frac{\pi}{2}$)

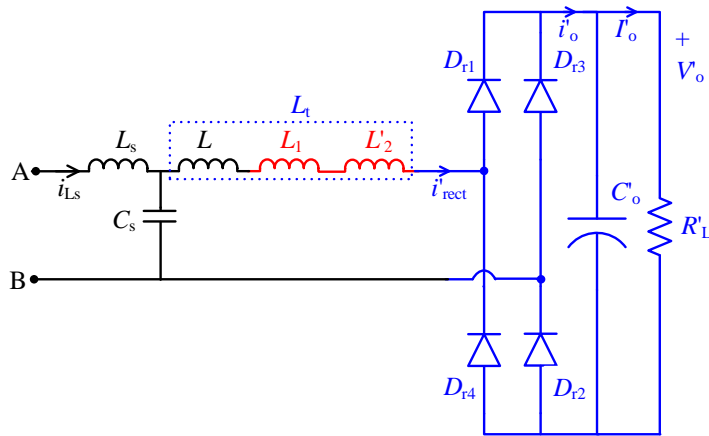
$$V'_{rect1(p)} = \frac{4V'_o}{\pi} \quad (3.3)$$

The average output current from Fig. 3.6 can be obtain as follows:

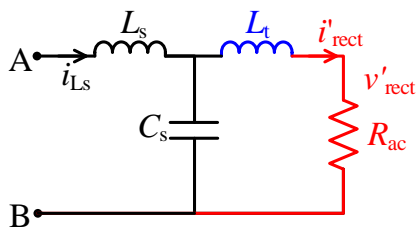
$$I'_o = \frac{1}{\pi} \int_0^{\pi} I'_{rect(p)} \sin(\omega_s t) d(\omega_s t) \quad (3.4)$$



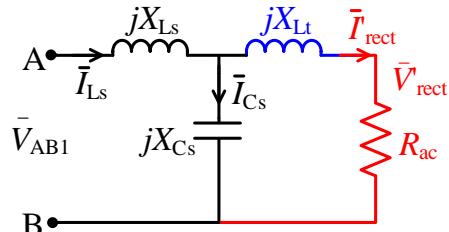
(a)



(b)



(c)



(d)

Figure 3.5: Simplification of converter circuit: (a) representation of HF transformer by its T-equivalent, (b) series connected L_1 , L'_2 , and L are replaced by L_t , (c) diode rectifier, filter capacitor and load resistance equivalently represented by an AC resistance R_{ac} , and (d) phasor circuit for analysis.

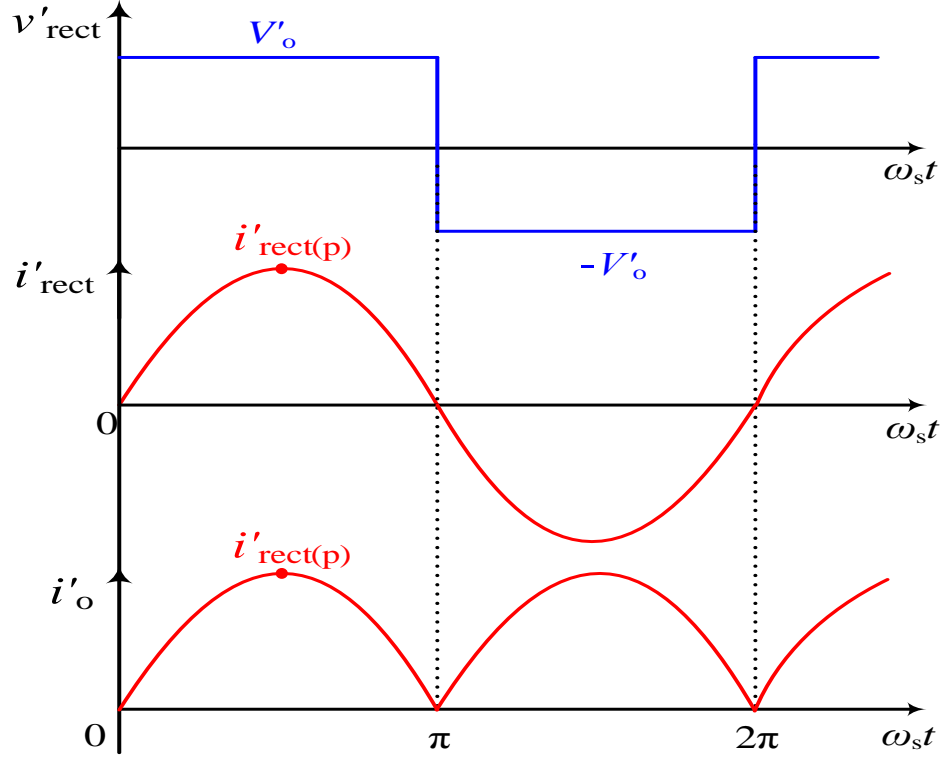


Figure 3.6: Input voltage and current waveforms of the diode rectifier which are used in deriving the expression for R_{ac} .

Therefore,

$$I'_o = \frac{2}{\pi} I'_{rect(p)} \quad (3.5)$$

The RMS values of v'_{rect} and i'_{rect} are obtain from 3.3 and 3.5 as:

$$V'_{rect1} = \left(\frac{2\sqrt{2}}{\pi} \right) V'_o \quad (3.6)$$

$$I'_{rect} = \left(\frac{\pi}{2\sqrt{2}} \right) I'_o. \quad (3.7)$$

From 3.6 and 3.7, the equivalent AC resistance is (Steigerwald, 1988),

$$R_{ac} = \frac{V'_{rect1}}{I'_{rect}} = \left(\frac{8}{\pi^2} \right) R'_L \quad (3.8)$$

where,

$$R'_L = R_L/n_t^2$$

where, R'_L is the primary referred load resistance and n_t is the turns ratio of HF transformer.

The phasor circuit given in Fig. 3.5(d) is used in analysis of the LCL-T converter by using FHA method in the following subsection.

3.3.2 ANALYSIS

The inverter output voltage (v_{AB}) for waveform shown in Fig. 3.2 using Fourier series can be obtain as follows (Refer Appendix-A, (A.7)):

$$v_{AB}(t) = \sum_{n=1,3,5..}^{\infty} \frac{4V_s}{\pi} \sin\left(\frac{n\pi}{2}\right) \sin\left(\frac{n\delta}{2}\right) \sin(n\omega_s t) \quad (3.9)$$

The fundamental component of v_{AB} (i.e., $n = 1$) is obtain as,

$$v_{AB1}(t) = \frac{4V_s}{\pi} \sin\left(\frac{\delta}{2}\right) \sin(\omega_s t) \quad (3.10)$$

The peak inverter output voltage using (3.10) as:

$$V_{AB1(p)} = \frac{4V_s}{\pi} \sin\left(\frac{\delta}{2}\right) \quad (3.11)$$

Therefore, the effective (RMS) inverter output voltage, v_{AB} from Fig. 3.11 is:

$$V_{AB1} = \left(\frac{2\sqrt{2}}{\pi}\right) V_s \cdot \sin\left(\frac{\delta}{2}\right) \quad (3.12)$$

where, δ is the pulse-width angle of v_{AB} .

Using Fig. 3.5(d), we can obtain,

$$\frac{V'_{rect1}}{V_{AB1}} = \frac{1}{\{(1 - F^2)^2 + (\frac{\pi^2}{8}Q[(1 + K)F - KF^3])^2\}^{\frac{1}{2}}} \quad (3.13)$$

but from 3.6 and 3.12,

$$\frac{V'_{rect1}}{V_{AB1}} = \frac{V'_o}{V_s} \cdot \frac{1}{\sin\left(\frac{\delta}{2}\right)}. \quad (3.14)$$

The voltage gain (M) is:

$$M = \frac{V'_o}{V_s}. \quad (3.15)$$

Therefore, using 3.13, 3.14, and 3.15, M can be obtained as:

$$M = \frac{\sin\left(\frac{\delta}{2}\right)}{\left\{(1 - F^2)^2 + \left(\frac{\pi^2}{8}Q[(1 + K)F - KF^3]\right)^2\right\}^{\frac{1}{2}}} \quad (3.16)$$

where,

$$\begin{aligned} F &= \frac{\omega_s}{\omega_r} = \frac{f_s}{f_r}; \quad Q = \frac{\omega_r L_s}{R'_L} = \frac{1}{\omega_r C_s R'_L}; \\ \omega_r &= \frac{1}{\sqrt{L_s C_s}} = 2\pi f_r; \quad \omega_s = 2\pi f_s; \quad K = \frac{L_t}{L_s}. \end{aligned} \quad (3.17)$$

here, f_s is the switching frequency in Hz, f_r is the resonant frequency in Hz, ω_s is the switching frequency in rad/sec, and ω_r is the resonant frequency in rad/sec.

The net impedance (Z_{AB}) from Fig. 3.5(d) is:

$$Z_{AB} = R_{AB} + jX_{AB} \quad (3.18)$$

$$|Z_{AB}| = [R_{AB}^2 + X_{AB}^2]^{1/2} \quad (3.19)$$

$$\phi = \tan^{-1}\left(\frac{X_{AB}}{R_{AB}}\right) \quad (3.20)$$

where,

$$\begin{aligned} R_{AB} &= \frac{R_{ac} X_{Cs}^2}{R_{ac}^2 + (X_{Lt} + X_{Cs})^2} \\ X_{AB} &= \frac{R_{ac}^2 (X_{Ls} + X_{Cs}) + (X_{Lt} + X_{Cs}) + ((X_{Lt} + X_{Cs})X_{Ls} + X_{Cs}X_{Lt})}{R_{ac}^2 + (X_{Lt} + X_{Cs})^2} \end{aligned}$$

and

$$X_{Ls} = \omega_s L_s; \quad X_{Lt} = \omega_s L_t; \quad X_{Cs} = \frac{-1}{\omega_s C_s}. \quad (3.21)$$

The resonant inductor current:

$$i_{Ls}(t) = I_{Lsp} \sin(\omega_s t - \phi). \quad (3.22)$$

The peak resonant inductor current:

$$I_{Lsp} = \frac{V_{AB1(p)}}{|Z_{AB}|} \quad (3.23)$$

Initial resonant inductor current (i.e., i_{Ls} at $\omega_s t = 0$):

$$i_{Ls0} = I_{Lsp} \sin(-\phi). \quad (3.24)$$

The peak resonant capacitor voltage:

$$V_{Csp} = (I_{Lsp} - I_{Ltp})|X_{Cs}| \quad (3.25)$$

The switch current is same as the resonant inductor current.

The kVA/kW rating of resonant tank circuit is:

$$\frac{kVA}{kW} = \frac{I_{Lsr}^2 X_{Ls} - I_{Csr}^2 X_{Cs} + I_{Ltr}^2 X_{Lt}}{P_o}. \quad (3.26)$$

3.3.3 ZVS CONDITIONS

To realize ZVS operation of all switches, the necessary condition is that the anti-parallel diode of respective switches should conduct prior to the switch. Therefore, to ascertain ZVS, expression for current through the switches is obtained as given in (3.27) - (3.30) and the initial current is verified to be negative. The negative switch current indicates conduction of anti-parallel diode. This happens when the current through the resonant circuit/switch lags the inverter output voltage. For the proposed modulation scheme as given in Fig. 3.3, the initial current for switch S_1 is determined by substituting $\omega_s t = 0$ in the expression for current given in (3.22). Similarly, for switches S_2 - S_4 , the initial current is found by substituting $\omega_s t = \alpha, (\pi + \alpha)$ and π respectively in the expression for current given in (3.22). The ZVS condition (i.e., the initial switch current) for all the switches is given below:

Initial current through switch S_1 (i_{S1}) is:

$$i_{S1}(0) = i_{Ls0}(t) = I_{Lsp} \sin(\omega_s t - \phi) < 0 @\omega_s t = 0 \quad (3.27)$$

where, $\phi < \pi$.

Initial current through switch S_2 (i_{S2}) is:

$$i_{S2}(0) = i_{Ls0}(t) = I_{Lsp} \sin(\omega_s t - \phi) < 0 @\omega_s t = \alpha \quad (3.28)$$

where, $\alpha < \phi < \pi$.

Initial current through switches S_3 (i_{S3}) is:

$$i_{S3}(0) = -i_{Ls0}(t) = -I_{Lsp} \sin(\omega_s t - \phi) < 0 @\omega_s t = \pi + \alpha \quad (3.29)$$

where, $\alpha < \phi < \pi$.

Initial current through switches S_4 (i_{S4}) is:

$$i_{S4}(0) = -i_{Ls0}(t) = -I_{Lsp} \sin(\omega_s t - \phi) < 0 @\omega_s t = \pi \quad (3.30)$$

where, $\phi < \pi$.

3.4 DESIGN

The design specifications of the proposed phase-shifted gating controlled LCL-T resonant converter are given in Table 3.1. The choice of optimum design parameters such as full-load quality factor (Q), frequency ratio (F), inductor ratio (K), and DC voltage gain (M) plays a vital role in making the converter design compact and efficient. These optimum design parameters can be selected by using the design curves presented in Figs. 3.7 and 3.8. These design curves are drawn using equations given in Section 3.3. To achieve ZVS, the resonant current is made to lag by using $F > 1$ in the design. The converter is designed for $V_s(\text{min.})$ and full-load, where $\delta = \pi$ is used.

Table 3.1: Design specification of the converter

Parameter	Rating
Minimum DC input voltage, $V_s(\text{min.})$	110 V
Maximum DC input voltage, $V_s(\text{max.})$	180 V
DC output voltage, V_o	220 V
Output load power, P_o	300 W
Switching frequency, f_s	100 kHz

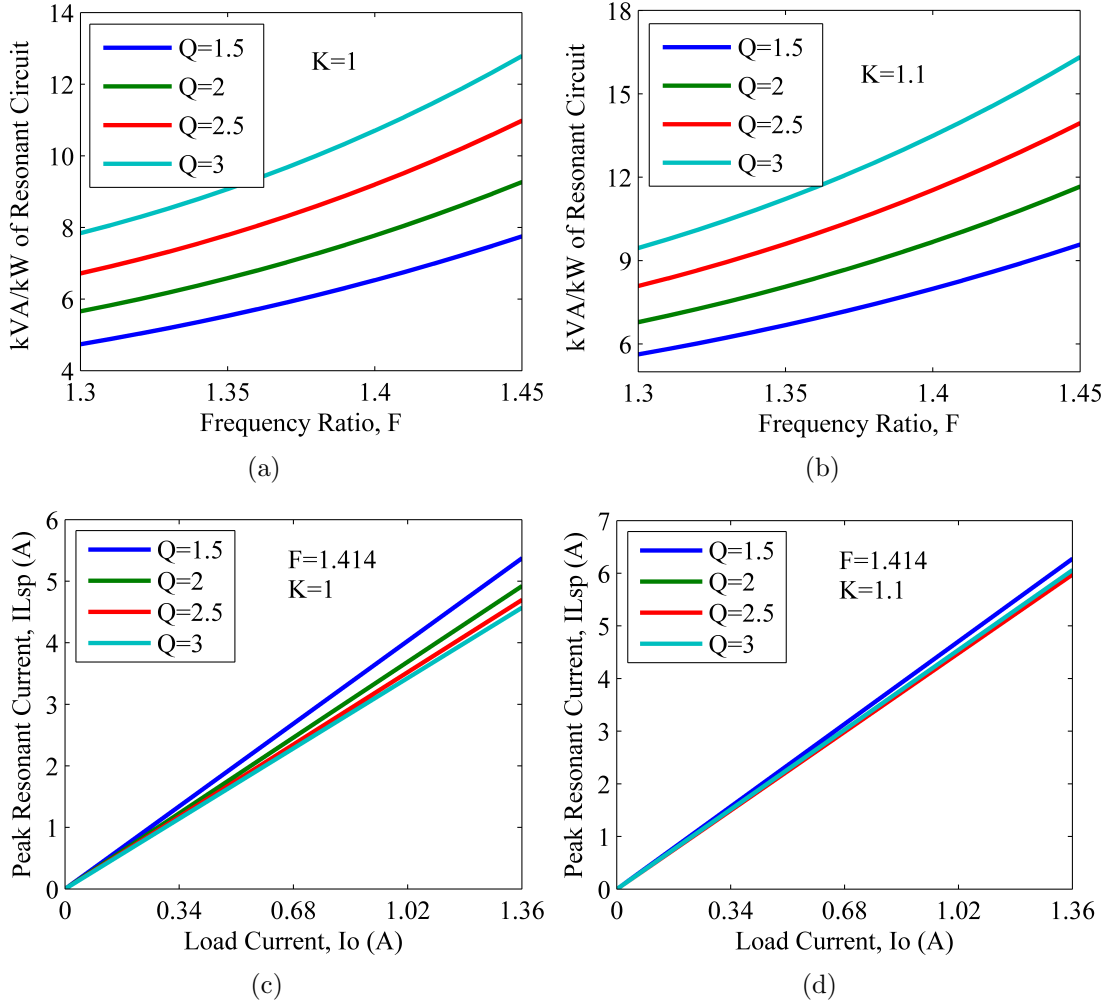


Figure 3.7: Plot of: kVA/kW versus F for (a) $K = 1$ and (b) $K = 1.1$; I_{Lsp} versus I_o for (c) $K = 1$ and (d) $K = 1.1$.

3.4.1 DESIGN TRADE-OFFS

Various design curves are drawn as shown in Figs. 3.7 and 3.8 which are used in choice of optimum design parameters. The following observations can be made from Fig. 3.7:

- kVA/kW rating increases for increasing Q as shown in Figs. 3.7(a) and (b).
- The peak resonant current I_{Lsp} decreases with I_o for increasing Q as shown in Figs. 3.7(c) and (d). Therefore, $Q = 2.5$ is chosen since the decrease in I_{Lsp} is not drastic for $Q \geq 2.5$.
- Both kVA/kW rating and I_{Lsp} increases for increasing K as shown in Fig. 3.7(b) and 3.7(d) respectively for same values of F and Q . Hence, $K = 1$ is chosen.

In Fig. 3.8(a), for $Q = 2.5$ and $K = 1$, the reduction in pulse-width angle (δ) from its full load value (i.e., $\delta = \pi$) to regulate output voltage is lowest for $F = 1.414$. Hence, $F = 1.414$ is selected since it requires a very small change in δ for entire loading conditions. The variation of converter voltage gain (M) versus F for different values of Q with $K = 1$ is shown in Fig. 3.8(b).

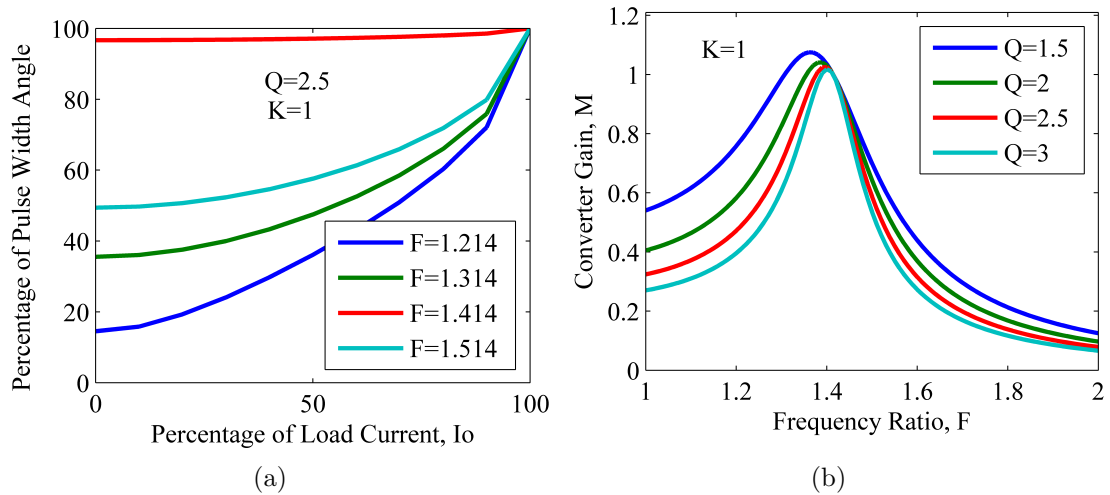


Figure 3.8: Design curves: (a) percentage of δ versus percentage of I_o for variations in F with $Q = 2.5$ and $K = 1$. (b) M versus F for variations in Q with $K = 1$.

3.4.2 DESIGN SUMMARY

The steps involved in calculation of circuit elements for the chosen near optimum design parameters of $Q = 2.5$, $F = 1.414$, and $K = 1.0$, with minimum input voltage of $V_s = 110$ V are as follows

Step-1: The converter gain can be read from Fig. 3.8(b) as $M = 1.0$.

Step-2: The output voltage when reflected on the primary side of the HF transformer is $V'_o = 110$ V.

Step-3: HF transformer turns ratio $n = V_o/V'_o = 2$.

Step-4: The load resistance when reflected on the primary side is $R'_L = R_L/n^2 = 40.33 \Omega$.

Step-5: The values of resonant circuit elements L_s and C_s obtained by solving the (3.17), i.e., $Q = \omega_r L_s/R'_L$, $\omega_r = 1/\sqrt{(L_s C_s)}$, are $L_s = 226.74 \mu\text{H}$ and $C_s = 22.34 \text{ nF}$.

Step-6: Since $K = L_t/L_s = 1$, $L_t = 226.74 \mu\text{H}$.

Step-7: The equivalent impedance across the HF inverter output terminals (A, B) using (3.18)-(3.21) is $Z_{AB} = 27.04 + j12.32 \Omega$, $|Z_{AB}| = 29.69 \Omega$, and $\phi = 24.5^\circ$.

Step-8: The peak current through resonant inductor L_s using 3.23 is $I_{Lsp} = 4.71$ A. The maximum resonant capacitor voltage using 3.25, $V_{Csp} = 639.64$ V. The peak value of current through L_t is $I_{Ltp} = 4.28$ A.

3.5 SIMULATION RESULTS

PSIM simulation software tool is used to study the performance of proposed phase-shifted gating controlled LCL-T resonant converter. In the simulations, the converter specifications and the calculated values of different elements as given in Section 3.4 are used. The following six different cases are considered with two input voltages and three loading conditions.

- Case-1: $V_s(\text{min.}) = 110$ V & full-load

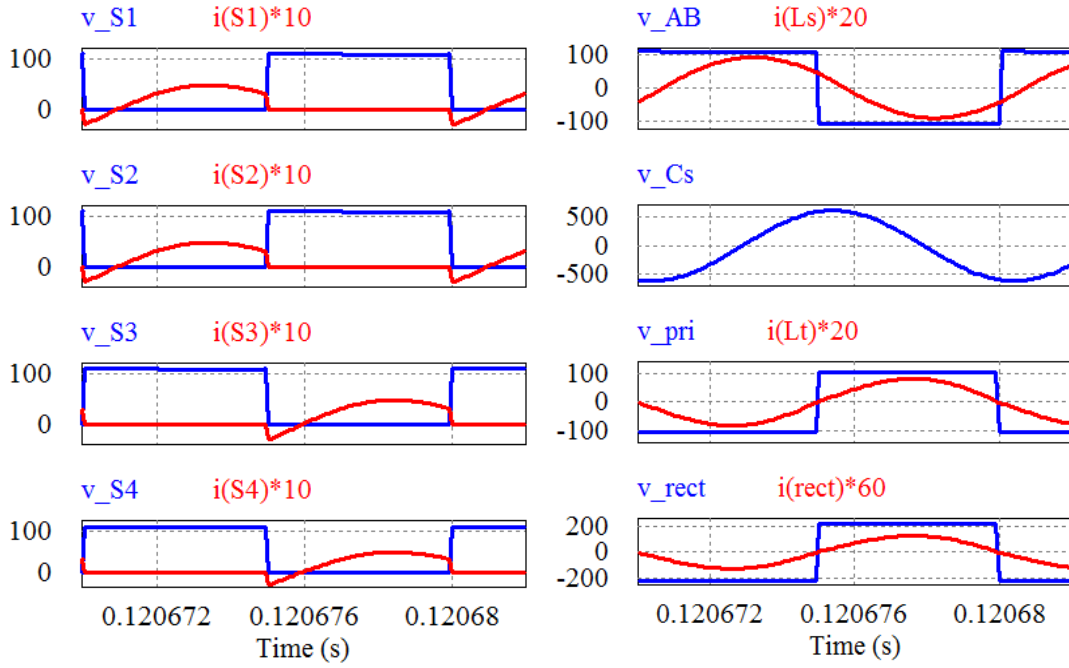
- Case-2: $V_s(\text{min.}) = 110 \text{ V}$, half-load
- Case-3: $V_s(\text{min.}) = 110 \text{ V}$, 10% of full-load
- Case-4: $V_s(\text{max.}) = 180 \text{ V}$, full-load
- Case-5: $V_s(\text{max.}) = 180 \text{ V}$, half-load
- Case-6: $V_s(\text{max.}) = 180 \text{ V}$, 10% of full-load

The waveforms obtained from the simulations are shown in Figs. 3.9-3.11. In the simulations, the resonant inductors, resonant capacitor, and high-frequency transformer are chosen to be ideal. The output voltage (V_o) is 213.96 V in case-1. This voltage is regulated for changes V_s and R_L by phase-shifting the gating signals of S_2 and S_3 by an angle α (or $\delta = \pi - \alpha$) as described in Section 3.1. The phase-shift angle ‘ α ’ is changed manually. Hence, several iterations were carried out in simulations to determine the appropriate value of ‘ α ’ for the given input voltage/loading condition.

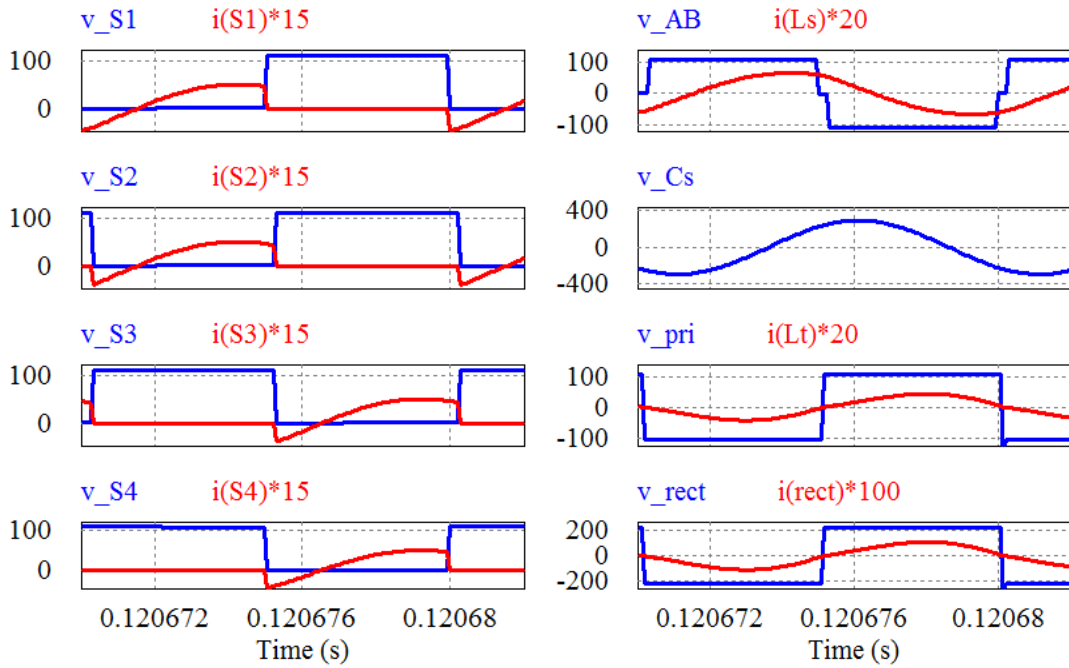
The simulation waveforms are presented in Figs. 3.9-3.11. In these Figs. the waveforms are arranged as following:

(a), (c): shows the voltage across each switch (v_{s1} , v_{s2} , v_{s3} , and v_{s4}) and current through respective switches (i_{s1} , i_{s2} , i_{s3} , and i_{s4}) to show the zero-voltage switching (ZVS). Since the switch voltage becomes zero before the switch current starts to rise in the positive direction indicates that there is ZVS. This minimizes the turn-on loss of the switch. From Figs. 3.9(a), 3.9(c) and 3.10(a) it can be observed that, this is true for all the switches with the $V_s(\text{min.})$ (i.e., cases 1-3) and from Fig. ??(c) with maximum input voltage. However, two switches lose ZVS when operating with $V_s(\text{max.})$. This can be verified from Figs. 3.10(c), 3.11(a) for the cases with the maximum input voltage (i.e., cases 4-5). Also, from Figs. 3.10(c) and 3.11(a), it can be seen that the anti-parallel diodes of switches S_2 and S_3 conduct before current jumps to zero. Hence, switches S_2 and S_3 turn-off with ZCS.

(b), (d): shows the voltage across inverter output terminals (v_{AB}), current through resonant inductor (i_{Ls}), resonant capacitor voltage (v_{Cs}), inductor current (i_{Lt}), rectifier input voltage (v_{rect}) and current (i_{rect}). From Figs. 3.9(b)-3.11(d), it can be observed that the peak resonant/switch current reduces as the load is decreased. This is an important feature of a good converter since the part load efficiency can be maintained high. The peak current through resonant inductor decreases from 4.68 A at $V_s(\text{max.}) = 180 \text{ V}$, full-load (Fig. 3.10(d)) to 1.92 A at $V_s(\text{min.}) = 110 \text{ V}$, 10%

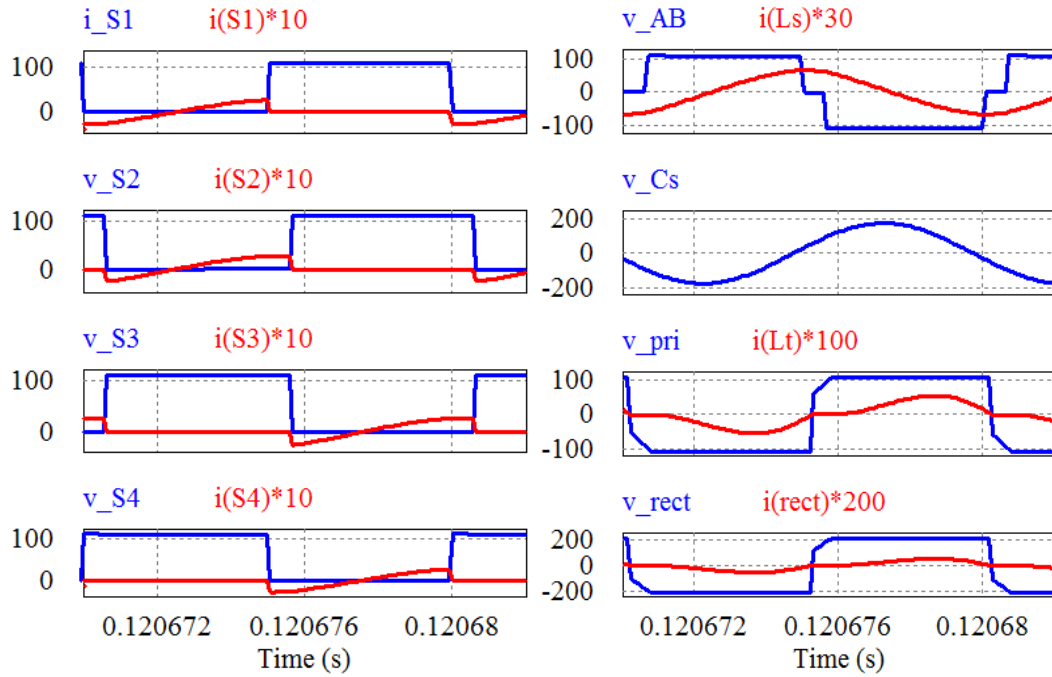


(a) (b)
 (i) Case-1 ($V_s(\text{min.}) = 110$ V, full-load)

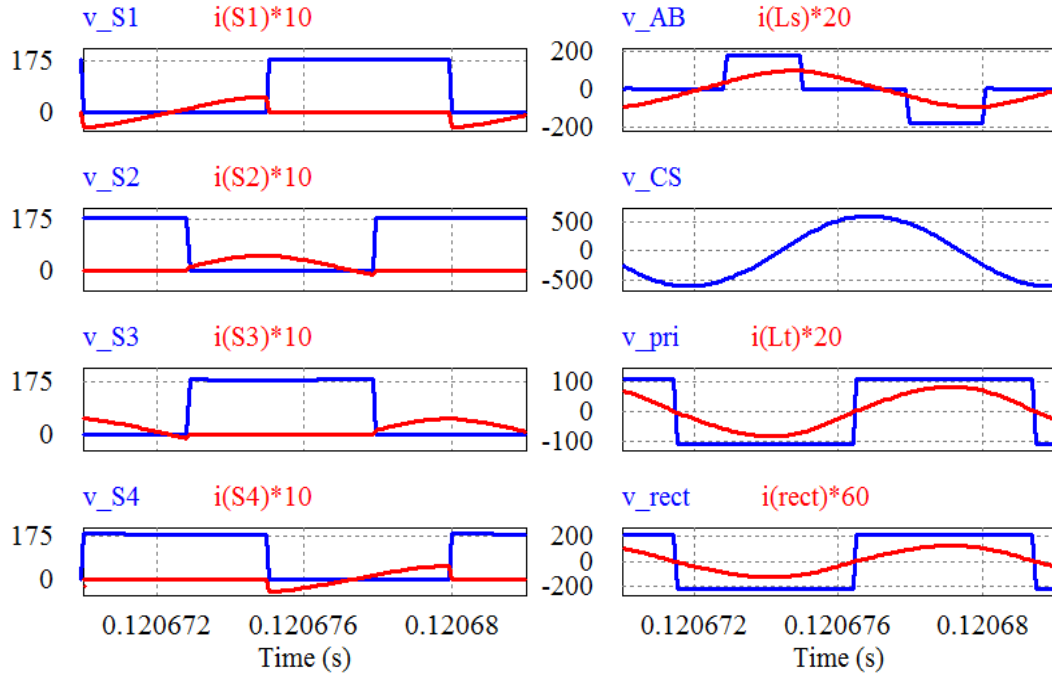


(c) (d)
 (ii) Case-2 ($V_s(\text{min.}) = 110$ V, half-load)

Figure 3.9: Simulation waveforms for cases 1 and 2: (a), (c) Current through and voltage across inverter switches; (b), (d) v_{AB} , i_{Ls} , v_{Cs} , v_{Cs} , i_{Lt} , v_{rect} , and i_{rect} .

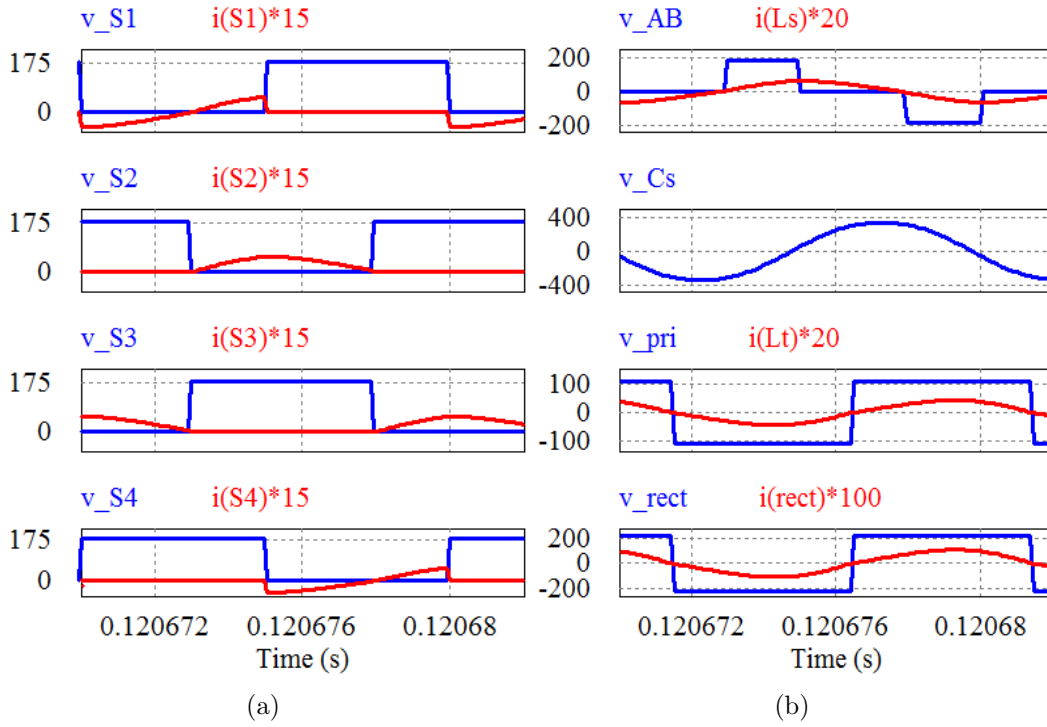


(i) Case-3 ($V_s(\text{min.}) = 110$ V, 10% of full-load)

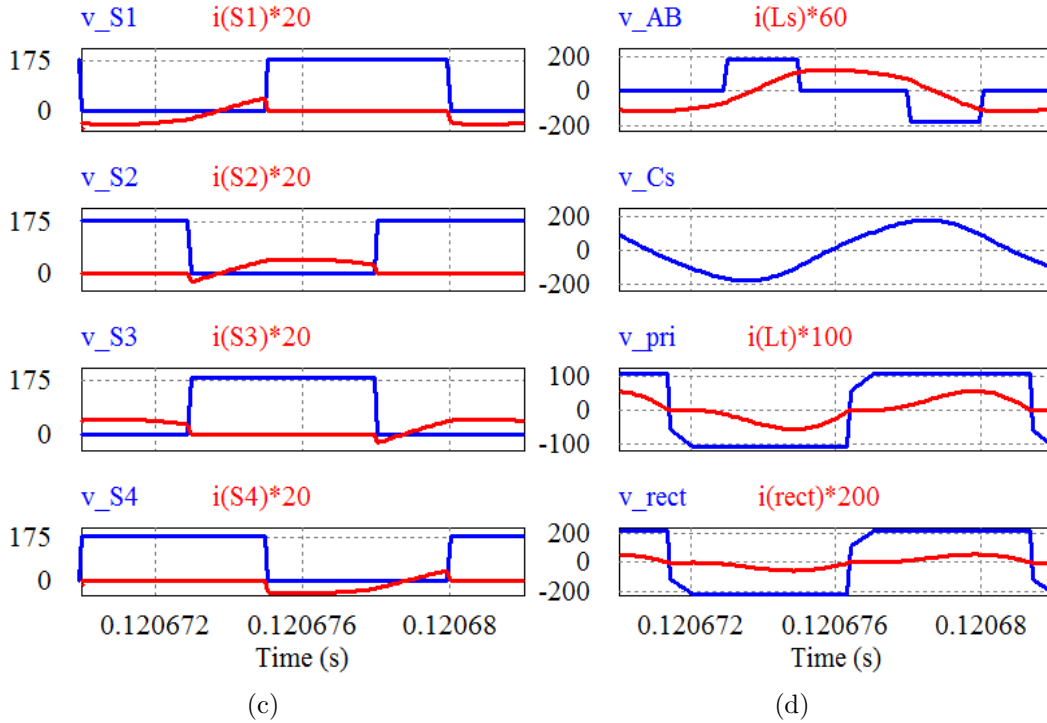


(ii) Case-4 ($V_s(\text{max.}) = 180$ V, full-load)

Figure 3.10: Simulation waveforms for cases 3 and 4: (a), (c) Current through and voltage across inverter switches; (b), (d) v_{AB} , i_{Ls} , v_{Cs} , v_{Cs} , i_{Lt} , v_{rect} , and i_{rect} .



(i) Case-5 ($V_s(\max)= 180$ V, half-load)



(ii) Case-6 ($V_s(\max.) = 180$ V, 10% of full-load)

Figure 3.11: Simulation waveforms for cases 5 and 6: (a), (c) Current through and voltage across inverter switches; (b), (d) v_{AB} , i_{Ls} , v_{Cs} , v_{Cs} , i_{Lt} , v_{rect} , and i_{rect} .

Table 3.2: Summary of power loss calculations

Case	Inverter MOSFET Losses				Transformer +Q Losses (W)	Output Rectifier Losses (W)	Total Loss (W)
	Turn -on (W)	Turn -off (W)	Condu -ction (W)	Body Diode (W)			
Full-load $V_s = 110$ V	0	0.071	10.40	0.428	3	2.728	16.628
Half-load	0	0.035	5.20	0.214	1.5	1.364	8.313
10% load	0	0.007	1.04	0.042	3	0.272	1.661
Full-load $V_s = 180$ V	57.62	0.071	10.40	0.428	3	2.728	74.24
Half-load	28.81	0.035	5.20	0.214	1.5	1.364	37.12
10% load	5.76	0.007	1.04	0.042	3	0.272	7.42

of full-load (Fig. 3.10(b)). Also, rectifier voltage and current are in-phase, which indicates that the rectifier diode losses are at minimum. The peak voltage stress that appears across each switch is the maximum value of the input voltage (i.e., $V_s(\text{max.}) = 180$ V). The maximum voltage stress across each output rectifier diodes is the value of the output voltage (i.e., $V_o = 220$ V).

The power loss calculations of 300 W LCL-T resonant converter for a full load to 10% of full load with $V_s(\text{min.})$ and $V_s(\text{max.})$ are given in Table 3.2. The following

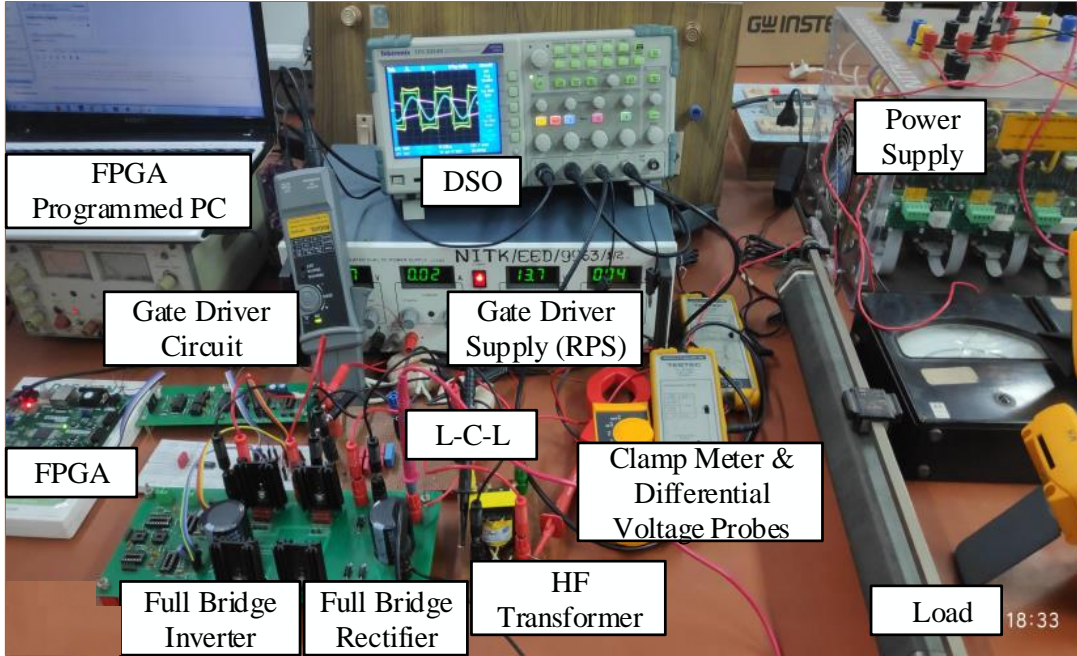


Figure 3.12: Experimental setup of 300 W LCL-T resonant power converter.

devices are chosen in the calculation of power losses. Inverter MOSFETs: IRF740, rectifier diode: UF5404. The transformer and Q losses are assumed to be 1% of output power.

Table 3.3: Details of the components used in experimental prototype

Component	Details
MOSFET switches (S_1 - S_4)	IRF740 (400V, 10A)
Resonant inductor (L_s)	242.71 μ H
Resonant inductor (L_t)	239.55 μ H
Resonant capacitor (C_s)	22.52 nF
HF transformer	Core: EE4215; Turns ratio: 14:28
Rectifier diodes (D_{r1} - D_{r4})	UF5404
Output capacitor (C_o)	470 μ F (400 V)

3.6 EXPERIMENTAL RESULTS

A 300 W experimental prototype of LCL-T resonant power converter given in Fig. 3.12 is built in the laboratory to validate the theoretical and simulation results. The part number/value of components used in this experimental prototype are listed in Table 3.3.

MOSFETs are used as the switching devices in building the full bridge inverter. Since the MOSFET has an inbuilt body diode, no external anti-parallel diode was used to connect across the MOSFET in the prototype. Ultra-fast recovery diodes are used in the output full-bridge rectifier due to faster switching times. The magnetic components in the resonant tank circuit and high-frequency transformer are built using EE type ferrite core. The resonant inductor, L_s is built with EE4215 core, and 1.56 mm^2 litz wire of 37 turns was used for winding. The designed values of the converter components are given in Section 3.4. The measured value of L_s using LCR meter is $242.71 \mu\text{H}$ at 100 kHz. The high-frequency transformer was built with EE4215 core. The measured value of total leakage inductance referred to the primary side is $3.16 \mu\text{H}$. Since the leakage inductance of the transformer is used as part of L_t , an inductance of $(242.71-3.16) 239.55 \mu\text{H}$ is built and connected at the primary side of the transformer. The gating signals of 3.75 V are generated using Nexys DDR4 artex-7 FPGA board. Driver circuit is developed to scale up the voltage to 15 V so as to drive the MOSFETs. Some of the waveforms obtained from the experiment are

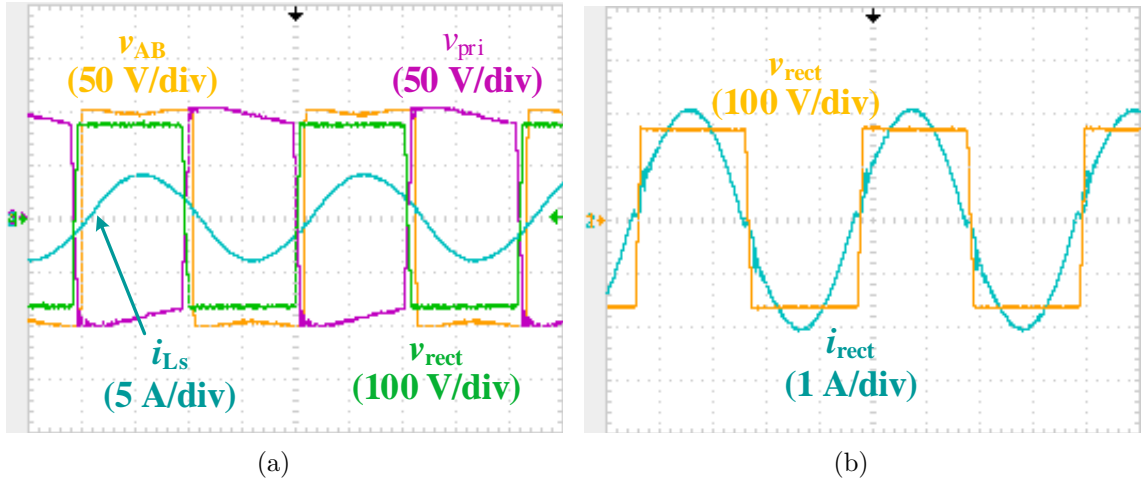


Figure 3.13: Experimental waveforms for case-1 ($V_s(\text{min.}) = 110 \text{ V}$ & full load, $R_L = 161.17 \Omega$): (a) v_{AB} , i_{L_s} , v_{pri} , v_{rect} , (b) v_{rect} , i_{rect} .

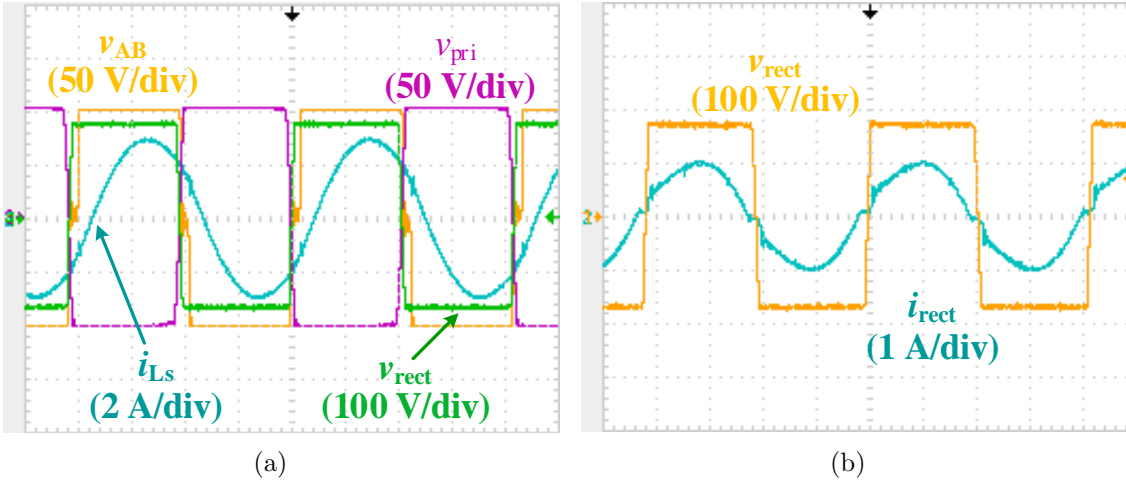


Figure 3.14: Experimental waveforms for case-2 ($V_s(\text{min.}) = 110 \text{ V}$ & half load, $R_L = 322.34 \Omega$): (a) v_{AB} , i_{L_s} , v_{pri} , v_{rect} , (b) v_{rect} , i_{rect} .

shown in Figs. 3.13-3.18. Since the built value of resonant inductor (L_s) is different from the actual designed value, switching frequency of the converter is reduced to 96.15 kHz. The experimental waveforms are presented in Figs. 3.13-3.18. In these Figs. the waveforms are arranged as following:

(a): voltage across inverter output terminals (v_{AB}); current through resonant inductor (i_{L_s}); transformer primary voltage (v_{pri}); and rectifier input voltage (v_{rect}).

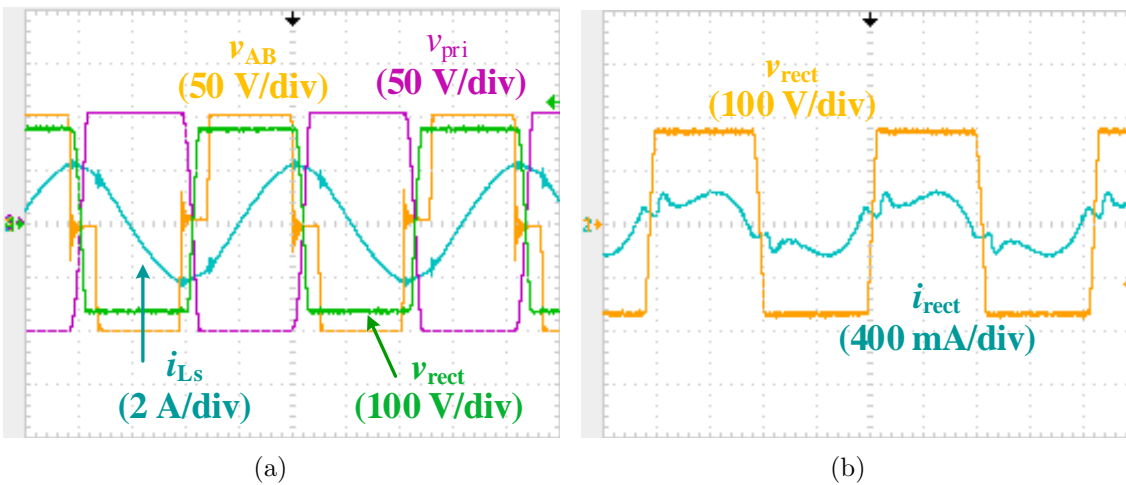


Figure 3.15: Experimental waveforms for case-3 ($V_s(\text{min.}) = 110 \text{ V}$ & 10% of full load, $R_L = 1611.7 \Omega$).

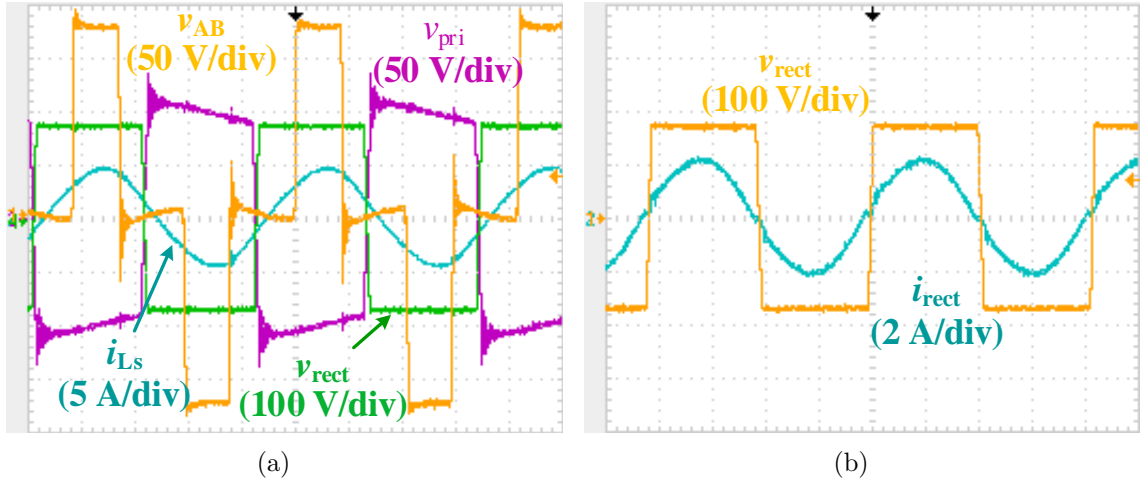


Figure 3.16: Experimental waveforms for case-4 ($V_s(\max.) = 180$ V & full load, $R_L = 161.17 \Omega$).

(b): voltage (v_{rect}) across and current (i_{rect}) through the input terminals of diode rectifier.

The peak inverter output current drops from 4.51 A at $V_s(\max.) = 180$ V, full-load (Fig. 3.16(a)) to 2.04 A at $V_s(\max.) = 180$ V, 10% of full-load (Fig. 3.18(b)). The results are presented in Table 3.4 for comparison. The efficiency comparison plot of theoretical, simulation, and experimental results for different loading conditions at

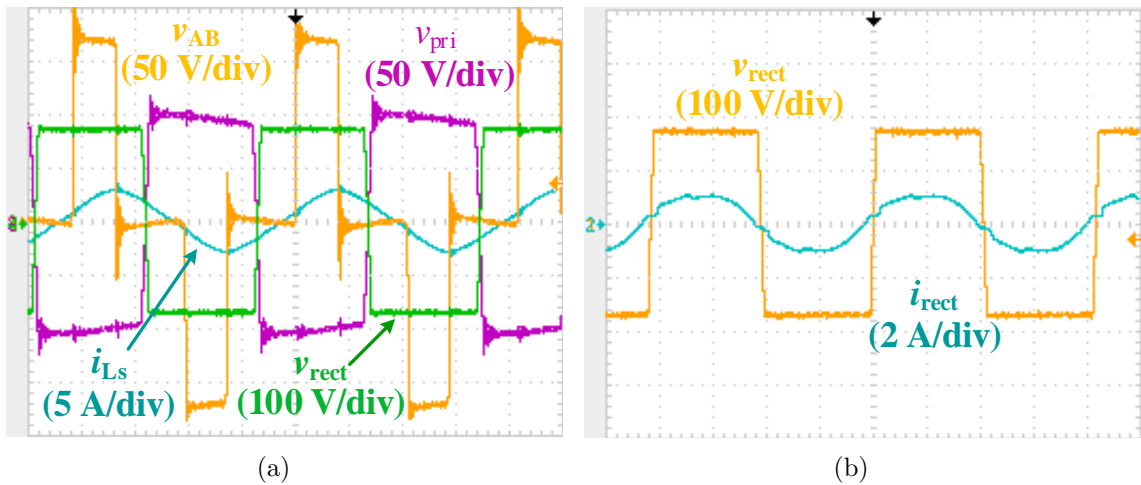


Figure 3.17: Experimental waveforms for case-5 ($V_s(\max.) = 180$ V & half load, $R_L = 322.34 \Omega$).

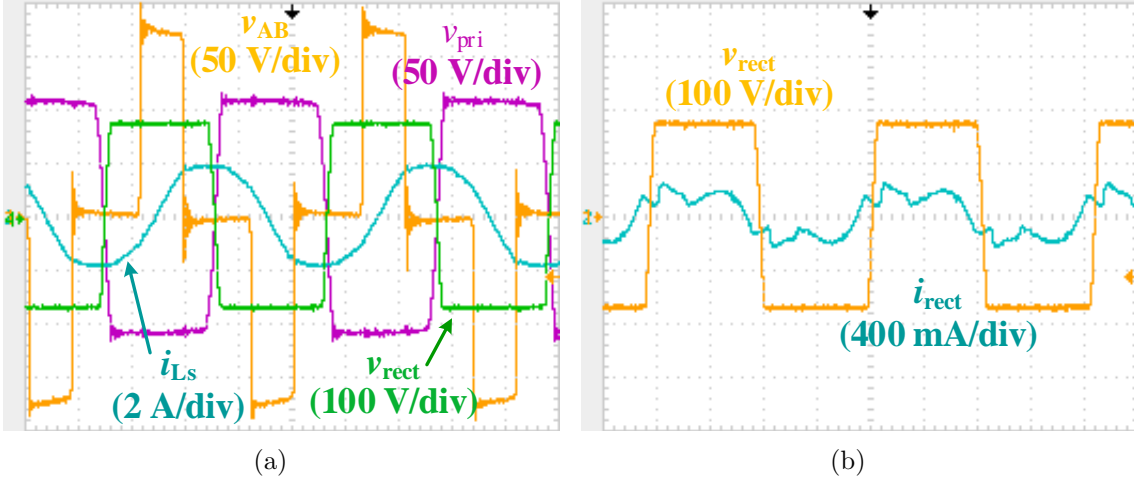


Figure 3.18: Experimental waveforms for case-6 ($V_s(\text{max.}) = 180 \text{ V}$ & 10% of full load, $R_L = 1611.7 \Omega$).

the minimum input voltage (i.e., $V_s(\text{min}) = 110 \text{ V}$) and the maximum input voltage (i.e., $V_s(\text{max}) = 180 \text{ V}$) is shown in Fig. 3.19(a) and (b) respectively.

Possible reasons behind the discrepancy between calculated, simulation, and experimental results are:

1. Only the fundamental components are considered in theoretical calculations. But, the effect of all the harmonics are included in simulations and experiments.
2. All switches, diodes, inductors, capacitors, and HF transformer are treated as

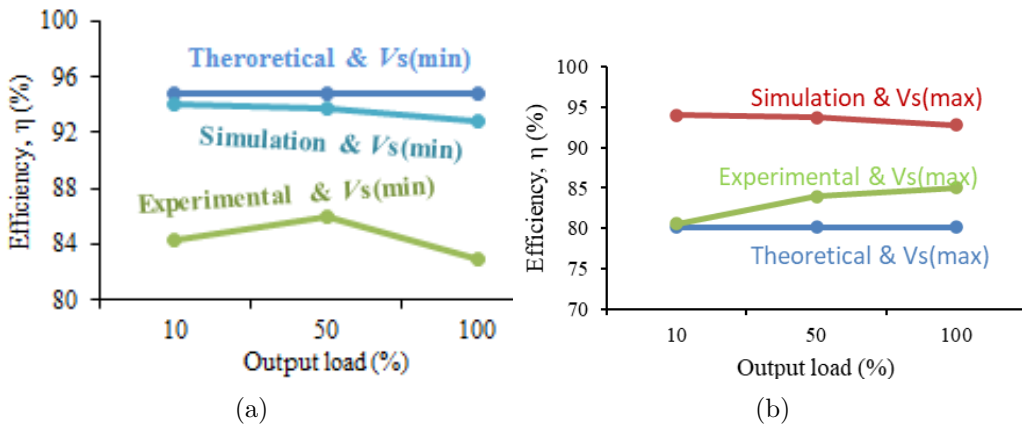


Figure 3.19: Efficiency comparison plot of theoretical, simulation, and experimental results at: (a) the minimum input voltage (i.e., $V_s(\text{min}) = 110 \text{ V}$), (b) the maximum input voltage (i.e., $V_s(\text{max}) = 180 \text{ V}$).

Table 3.4: Comparison of theoretical, simulation, and experimental results

Parameters	Case-1:			Case-2:			Case-3:		
	$V_s(\text{min.}), \text{ Full Load}$			$V_s(\text{min.}), \text{ Half Load}$			$V_s(\text{min.}), \text{ 10\% Load}$		
	Cal.	Sim.	Exp.	Cal.	Sim.	Exp.	Cal.	Sim.	Exp.
V_o (V)	220	213.96	197.4	220	213.92	204.60	220	213.82	202.20
I_o (V)	1.36	1.32	1.25	0.68	0.66	0.63	0.136	0.132	0.125
δ ($^\circ$)	180	180	180	176.4	170	154	174.6	157	146
I_{Lsr} (A)	3.33	3.30	2.87	1.66	1.97	2.15	0.33	1.36	1.51
I_{Ltr} (A)	3.03	2.94	2.92	1.51	1.47	1.46	0.30	0.29	0.33
V_{Csr} (V)	452.29	445	432.9	226.14	238.64	299.91	45.22	117.83	137.57
η (%)	94.74	94.14	82.96	94.74	94.12	85.93	94.74	94.00	84.25
Parameters	Case-4:			Case-5:			Case-6:		
	$V_s(\text{max.}), \text{ Full Load}$			$V_s(\text{max.}), \text{ Half Load}$			$V_s(\text{max.}), \text{ 10\% Load}$		
	Cal.	Sim.	Exp.	Cal.	Sim.	Exp.	Cal.	Sim.	Exp.
V_o (V)	220	212.52	202.50	220	213	201.4	220	213.17	201.5
I_o (V)	1.36	1.32	1.26	0.68	0.66	0.625	0.136	0.132	0.12
δ ($^\circ$)	75.33	76	80	75.13	75	72	75	73	67
I_{Lsr} (A)	3.34	3.31	3.19	1.67	2.01	1.92	0.33	1.37	1.44
I_{Ltr} (A)	3.03	2.92	3.02	1.51	1.47	1.58	0.3	0.3	0.3
V_{Csr} (V)	453.73	444.24	464.73	226.86	247.88	261.68	45.37	118.32	130.09
η (%)	80.16	92.80	85.05	80.16	93.72	83.91	80.16	94.02	80.60

ideal in theoretical calculations. In simulations, the drain to source resistance $R_{DS(\text{on})} = 0.45 \Omega$ in MOSFETs (IRF 740) and a voltage drop of 1 V in rectifier diodes (UF5404) are set and all other elements are chosen to be ideal. But in practical circuits, components suffer from loss of voltage and power.

3. In calculations, power loss of 1% is used for the transformer. However, in experiments, only the copper loss changes with the load and core losses are constant.

4. In theory, component values as designed are used, while in practical circuit, there is small difference in these values due to the difficulties in building the exact value components in the laboratory.
5. No dead gap is accounted for in theoretical calculations. But, in the experiment about 150 ns dead gap is provided.

3.7 SUMMARY

A fixed-frequency phase-shifted gating (PSG) controlled LCL-T resonant converter is proposed. The steady-state analysis using fundamental harmonic approximation method is presented. Performance of the proposed fixed-frequency converter is studied using simulations. Power loss breakdown analysis is performed for different input voltages and loading conditions. A 300 W laboratory prototype is built to validate the theoretical and simulation results. Using proposed phase-shift control technique from full-load to 10% of full-load, all switches in the inverter are achieving ZVS with the minimum input voltage and two switches lose ZVS with the maximum input voltage. A small change in phase-shift angle is sufficient to maintain the output voltage for input voltage and load variations. It is shown that LCL-T resonant converter works with fixed-frequency phase-shift control. Hence, the requirement of additional capacitor as in ADC control is avoided and the design of filter is simplified.

Chapter 4

MODIFIED GATING SIGNALS CONTROLLED LCL-T RPC AND COMPARISONS

Contents

4.1	OPERATING PRINCIPLE OF MGS CONTROL SCHEME	54
4.1.1	OPERATING MODES	54
4.2	STEADY-STATE ANALYSIS USING FOURIER SERIES	59
4.2.1	MODELING	59
4.2.2	NORMALIZATION	61
4.2.3	ANALYSIS	62
4.2.4	ZVS CONDITIONS	65
4.3	DESIGN	66
4.3.1	DESIGN TRADE-OFFS	67
4.4	SIMULATION RESULTS	70
4.5	EXPERIMENTAL RESULTS	76
4.6	PERFORMANCE COMPARISON OF PSG AND MGS CONTROL SCHEMES	81
4.7	SUMMARY	87

In this Chapter, a fixed-frequency modified gating signals (MGS) controlled LCL-T resonant power converter is discussed. Fourier series method is used to analyze the converter in steady-state. Also, the operation and performance comparison of LCL-T DC-DC resonant power converter when controlled with fixed-frequency phase-shifted gating (PSG) and modified-gating signals (MGS) schemes is discussed in this Chapter.

4.1 OPERATING PRINCIPLE OF MGS CONTROL SCHEME

The circuit diagram of LCL-T resonant converter is shown in Fig. 3.1. The fixed-frequency modified gating signal (MGS) control scheme is used to regulate the output voltage (V_o) of the LCL-T resonant converter whenever the input voltage (V_s) and the load (R_L) is changed. To achieve ZVS of inverter switches, the converter is required to be operated in lagging pf mode. Figs. 4.1 and 4.2 shows the typical operating and switching waveforms of proposed modified gating signal control for an arbitrary pulse width angle δ of the inverter output voltage v_{AB} . The converter is designed at an operating point where, the input voltage is minimum, and the load is maximum with $\delta = \pi$. To control the output DC voltage, the pulse-width angle δ is controlled by increasing the length of the gating signals of switches S_1 and S_3 and reducing the gating signals of switches S_2 and S_4 by an angle α as shown in Fig. 4.1.

4.1.1 OPERATING MODES

Different operating modes of LCL-T resonant power converter shown in Fig. 3.1 are presented in Fig. 4.3. There are five different operating modes possible for an angle α as arranged gating signals in Fig. 4.1. These modes are identified based on the devices conducting. Each mode of operation is explained with the help of equivalent circuits in the following subsections.

4.1.1.1 Mode-1 ($D_1, D_2 = \text{ON}$)

In this mode, the gating signals of devices S_1 and S_2 are active. Hence, the inverter output voltage, $v_{AB} = +V_s$. Since the converter operating in lagging pf mode, devices D_1 and D_2 conduct to provide a path for resonant current (i_{Ls}). Therefore, the

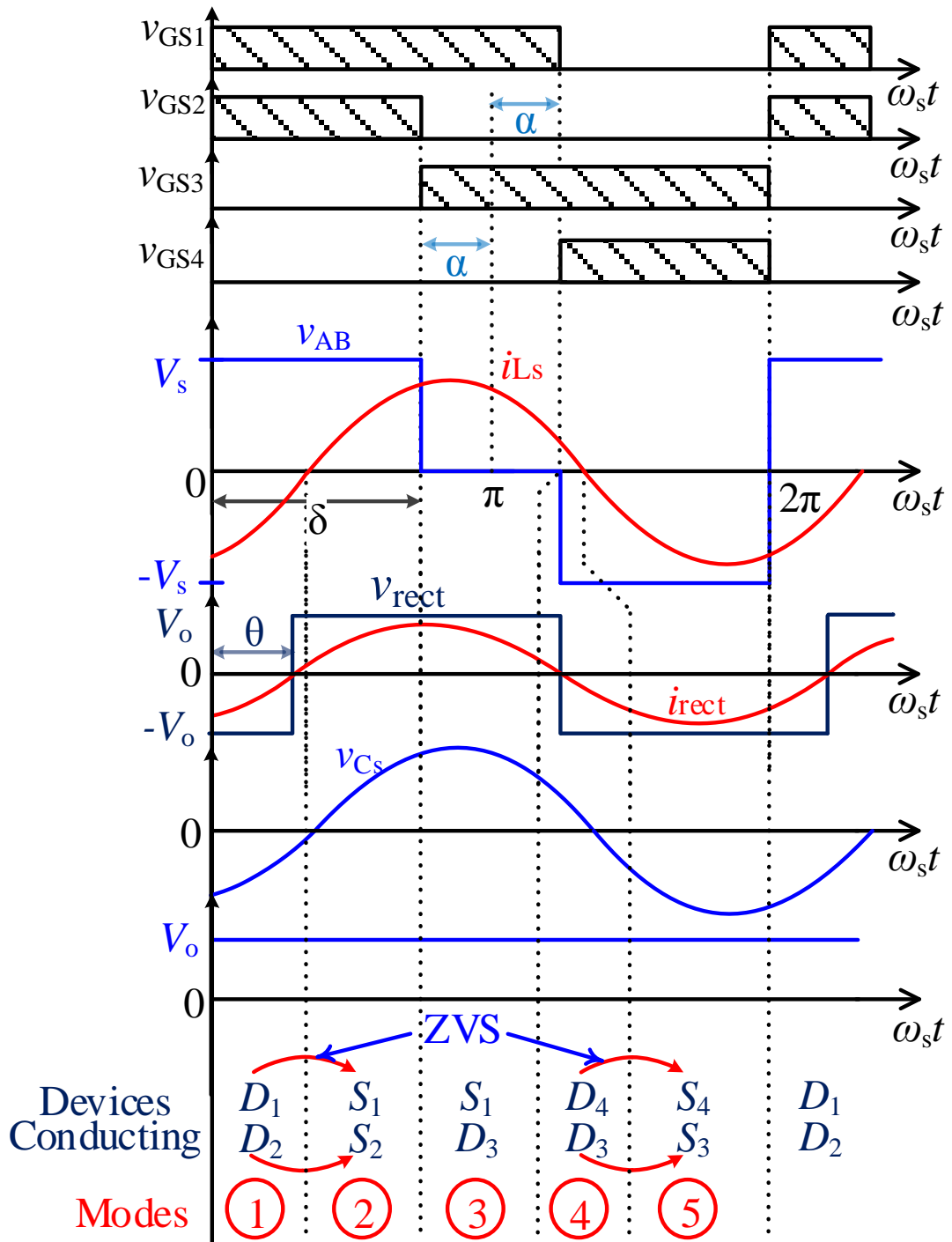


Figure 4.1: Typical operating waveforms of the proposed modified gating signal controlled LCL-T converter.

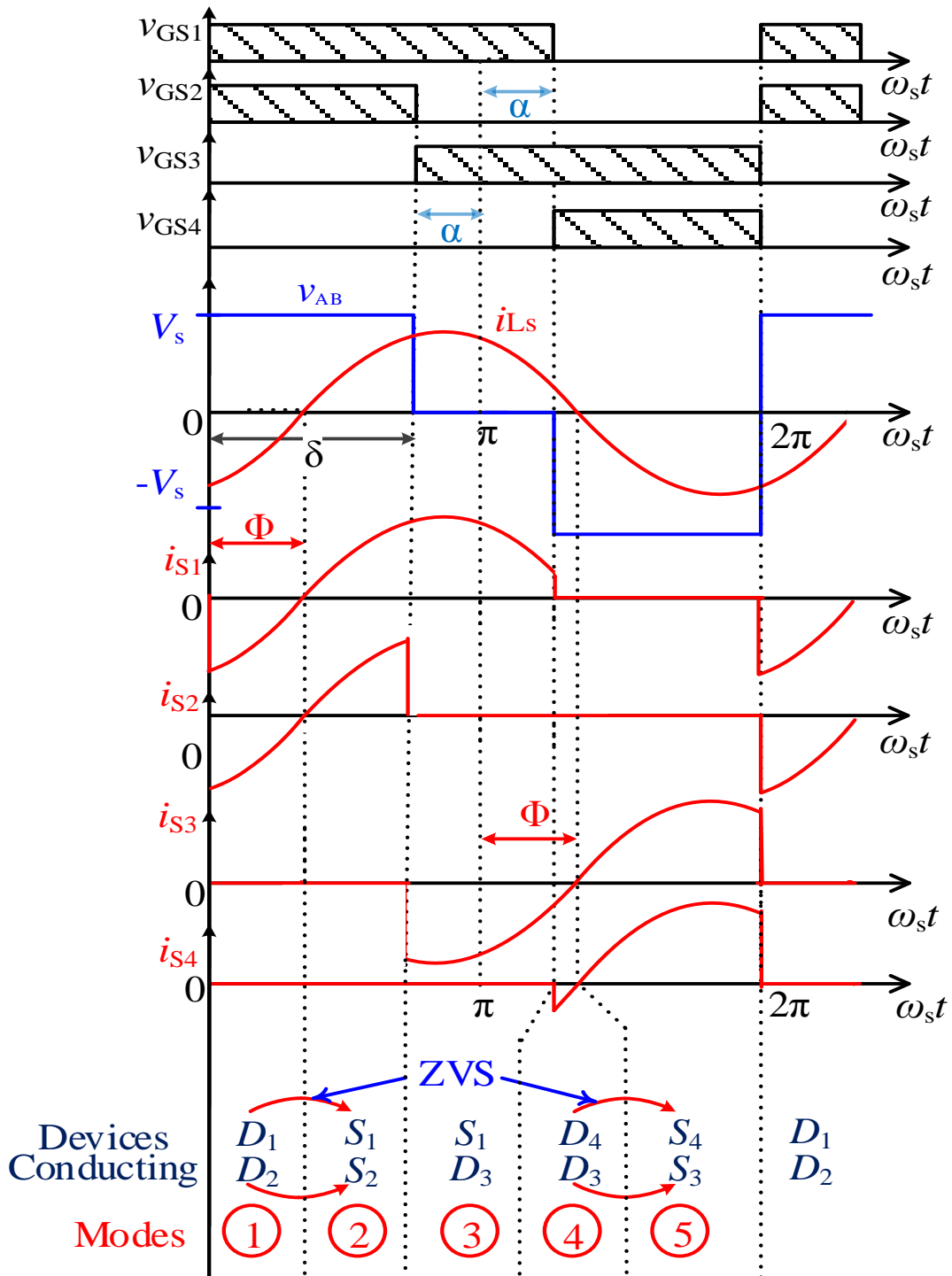


Figure 4.2: Typical switching waveforms of the proposed modified gating signal controlled LCL-T converter.

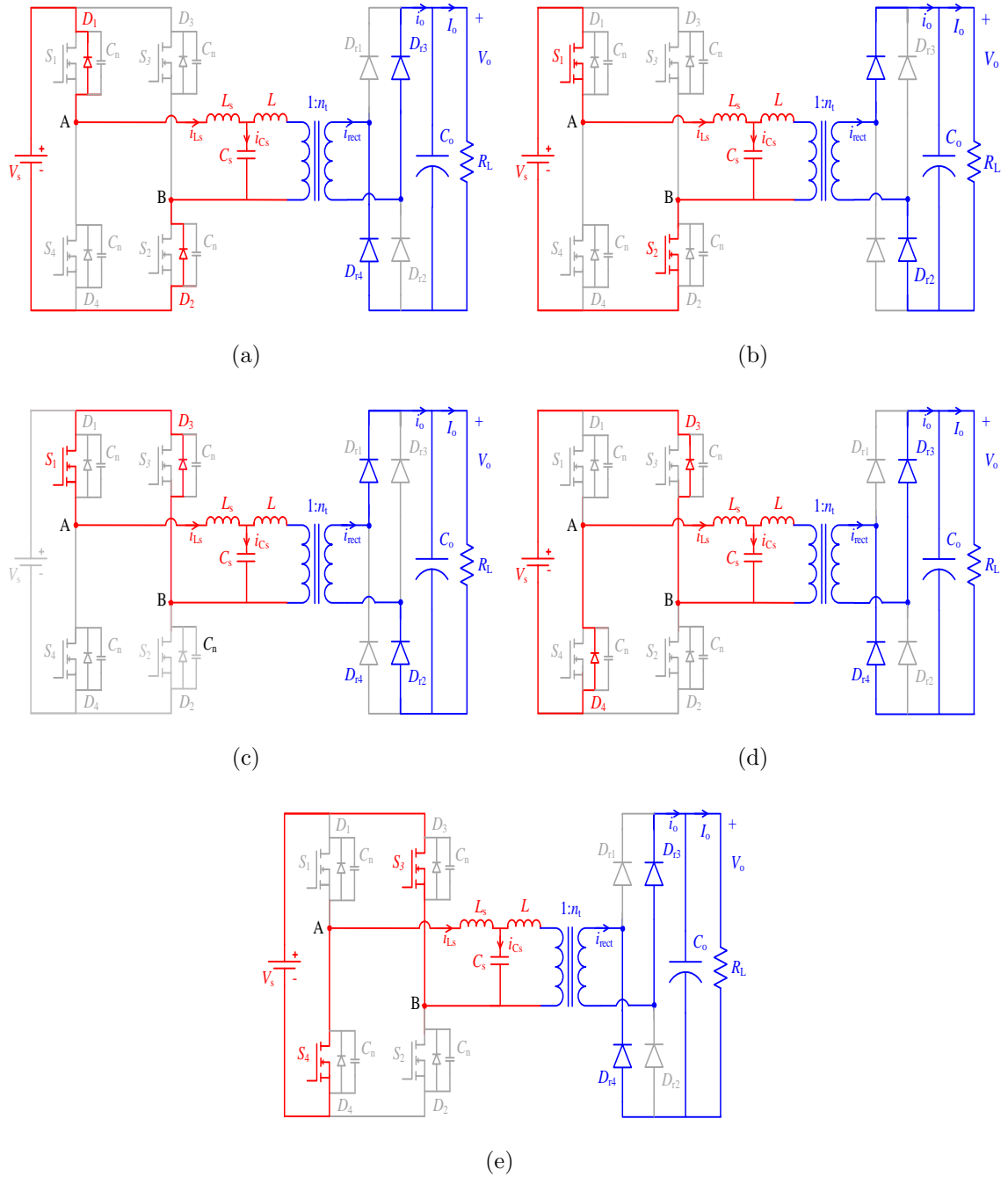


Figure 4.3: Equivalent circuits of LCL-T converter operating in: (a) mode-1 ($D_1, D_2 = \text{ON}$), (b) mode-2 ($S_1, S_2 = \text{ON}$), (c) mode-3 ($S_1, D_3 = \text{ON}$), (d) mode-4 ($D_3, D_4 = \text{ON}$), (e) mode-5 ($S_3, S_4 = \text{ON}$).

resonant current flows through the path $V_s - D_2 - \text{resonant circuit} - D_1 - V_s$ as indicated

in Fig. 4.3(a). In output rectifier block, diodes D_{r3} and D_{r4} conduct, while the output voltage remains constant. The rectifier diodes D_{r1} and D_{r2} are clamped to output voltage (V_o).

4.1.1.2 Mode-2 ($S_1, S_2 = \text{ON}$)

In this mode, the gating signals of devices S_1 and S_2 remain in active. Hence, the inverter output voltage, $v_{AB} = +V_s$. At the end of mode-1, the resonant current crosses zero and becomes positive. This positive voltage and current makes the devices S_1 and S_2 conducts with ZVS. Therefore, the resonant current (i_{Ls}) flows through the path $V_s - S_1 - \text{resonant circuit} - S_2 - V_s$ as indicated in Fig. 4.3(b). In output rectifier block, diodes D_{r1} and D_{r2} conduct, while the output voltage remains constant. The rectifier diodes D_{r3} and D_{r4} are clamped to output voltage (V_o).

4.1.1.3 Mode-3 ($S_1, D_3 = \text{ON}$)

In this mode, the gating signals of devices S_1 and S_3 are active. Hence, the inverter output voltage, $v_{AB} = 0$. At the end of mode-2, the gating signal for S_2 is removed. However, since the resonant current cannot change instantaneously, the path is provided by the diode D_3 . Therefore, the resonant current (i_{Ls}) flows through the path $S_1 - \text{resonant circuit} - D_3$ as indicated in Fig. 4.3(c). In output rectifier block, diodes D_{r1} and D_{r2} conduct, while the output voltage remains constant. The rectifier diodes D_{r3} and D_{r4} are clamped to output voltage (V_o).

4.1.1.4 Mode-4 ($D_3, D_4 = \text{ON}$)

In this mode, the gating signals of devices S_3 and S_4 are active. Hence, the inverter output voltage, $v_{AB} = -V_s$. Since the converter operating in lagging pf mode, devices D_3 and D_4 conduct to provide a path for resonant current (i_{Ls}). Therefore, the resonant current flows through the path $V_s - D_4 - \text{resonant circuit} - D_3 - V_s$ as indicated in Fig. 4.3(d). In output rectifier block, diodes D_{r1} and D_{r2} conduct, while the output voltage remains constant. The rectifier diodes D_{r3} and D_{r4} are clamped to output voltage (V_o).

4.1.1.5 Mode-5 ($S_3, S_4 = \text{ON}$)

In this mode, the gating signals of devices S_3 and S_4 remain in active. Hence, the inverter output voltage, $v_{AB} = -V_s$. At the end of mode-4, the resonant current crosses zero and becomes negative. This negative voltage and current makes the devices S_3 and S_4 conducts with ZVS. Therefore, the resonant current (i_{L_s}) flows through the path $V_s - S_3 - \text{resonant circuit} - S_4 - V_s$ as indicated in Fig. 4.3(e). In output rectifier block, diodes D_{r3} and D_{r4} conduct, while the output voltage remains constant. The rectifier diodes D_{r1} and D_{r2} are clamped to output voltage (V_o).

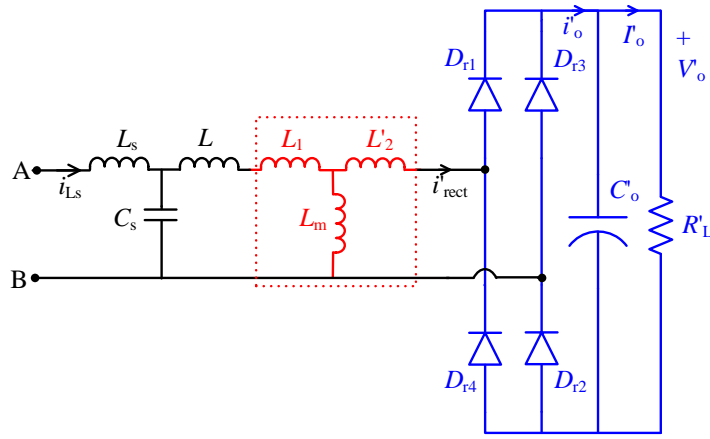
4.2 STEADY-STATE ANALYSIS USING FOURIER SERIES

In this section, the LCL-T resonant converter is analyzed by using the Fourier series (FS) approach. This method considers all the harmonic components in voltage and current waveforms. Hence, this method provides accurate and efficient results as compared to the fundamental harmonic approximation (FHA) analysis method where, only fundamental component is considered. Some of the assumptions made to reduce the complexity of the analysis are as follows:

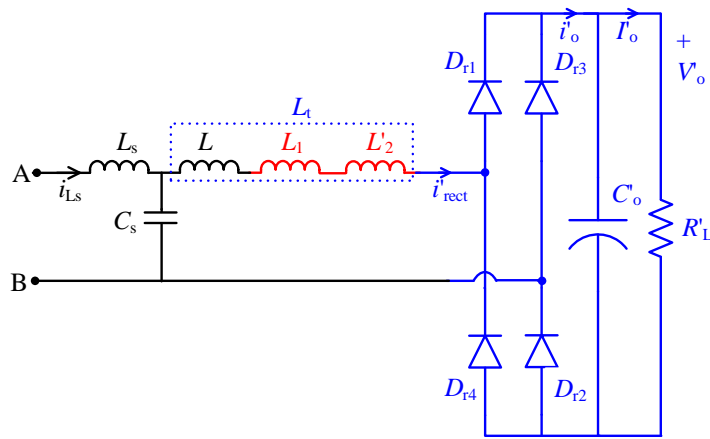
- all components in the circuit i.e., switches, diodes, inductors, and capacitors are loss free
- high-frequency (HF) transformer is represented by its T-equivalent
- magnetizing inductance of the HF transformer is very large.

4.2.1 MODELING

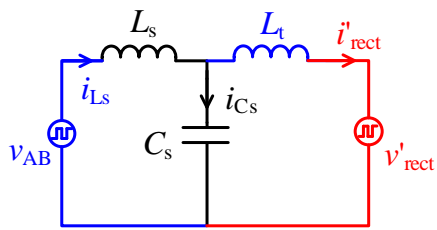
Fig. 4.4(a) shows the equivalent circuit diagram referred to primary side of HF transformer after replacing the transformer by its T-equivalent circuit. The HF transformer magnetizing current is very small due to the large value of the magnetizing inductance. Therefore, to reduce the complexity in the analysis, the magnetizing inductance L_m is treated as an open circuit and the resulting circuit is shown in Fig. 4.4(b). L , L_1 , and L'_2 in Fig. 4.4(b) are replaced by $L_t (L + L_1 + L'_2)$ in Fig. 4.4(c). The primary side referred diode rectifier, filter capacitance and the load are replaced by its equivalent



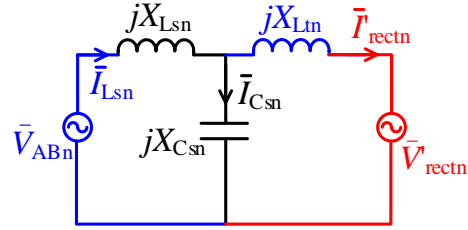
(a)



(b)



(c)



(d)

Figure 4.4: Simplification of converter circuit: (a) high frequency transformer represented as T-connection, (b) equivalent circuit of Fig. 4.4(a) after L_m treated as open circuit, (c) equivalent circuit of Fig. 4.4(b) after combining $L_1+L_2+L = L_t$ and represented with the rectifier input voltage, and (d) phasor equivalent circuit for n^{th} harmonic of Fig. 4.4(c) used for analysis.

voltage source v'_{rect} in Fig. 4.4(c). The n^{th} harmonic phasor equivalent circuit of Fig. 4.4(c) used for analysis is shown in Fig. 4.4(d).

4.2.2 NORMALIZATION

All the parameters referred to primary side of the transformer are denoted by a superscript ('). Normalization of some of the quantities is done to make the analysis simple. The following are the bases chosen.

$$V_B = V_s(min.), Z_B = (L_s/C_s)^{1/2}, I_B = V_B/Z_B \quad (4.1)$$

where, V_B is the voltage base, Z_B is the impedance base, and I_B is the current base.

All normalized and n^{th} harmonic quantities are denoted by subscript "0" and "n" respectively. The n^{th} harmonic reactive elements shown in Fig. 4.4(d) are normalized as below.

$$\begin{aligned} X_{Lsn} &= n\omega_s L_s, & X_{Lsn0} &= nF \\ X_{Csn} &= -1/(n\omega_s C_s), & X_{Csn0} &= -1/(nF) \\ X_{Ltn} &= n\omega_s L_t, & X_{Ltn} &= nFK \\ F &= \omega_s/\omega_r = f_s/f_r; & \omega_s &= 2\pi f_s; \quad \omega_r = 2\pi f_r = 1/\sqrt{L_s C_s}; & K &= L_t/L_s \end{aligned} \quad (4.2)$$

where, f_s is the switching frequency in Hz, f_r is the resonant frequency in Hz, ω_s is the switching frequency in rad/sec, and ω_r is the resonant frequency in rad/sec.

Converter gain,

$$M = \frac{V'_o}{V_s} = \frac{V_o}{(n_t V_s)} \quad (4.3)$$

where, V'_o is the output voltage referred to primary side of HF transformer.

Normalized load current,

$$J = \frac{I'_o}{I_B} = \frac{(n_t I_o)}{I_B} \quad (4.4)$$

4.2.3 ANALYSIS

From Fig. 4.1, the inverter output voltage v_{AB} and primary side referred rectifier input voltage v'_{rect} in time domain are derived as (Refer Appendix-A, (A.9)):

$$v_{AB}(t) = \sum_{n=1,3,5\dots}^{\infty} \frac{4V_s}{n\pi} \left[\frac{(1 - \cos(n\delta))}{2} \right] \sin(n\omega_s t) \quad (4.5)$$

$$v'_{rect}(t) = \sum_{n=1,3,5\dots}^{\infty} \frac{4V'_o}{n\pi} \sin(n\omega_s t - n\theta) \quad (4.6)$$

normalized v_{AB} and v'_{rect} can be obtained as:

$$v_{AB0}(t) = \sum_{n=1,3,5\dots}^{\infty} \frac{4}{n\pi} \left[\frac{(1 - \cos(n\delta))}{2} \right] \sin(n\omega_s t) \quad (4.7)$$

$$v'_{rect0}(t) = \sum_{n=1,3,5\dots}^{\infty} \frac{4M}{n\pi} \sin(n\omega_s t - n\theta) \quad (4.8)$$

where, δ is the pulse-width angle of v_{AB} and θ is the phase-shift angle of v'_{rect} with respect to v_{AB} shown in Fig. 4.1.

By referring to Fig. 4.4(d), the currents through L_s and L_t are simplified and normalized as,

$$i_{Ls0}(t) = \sum_{n=1,3,5\dots}^{\infty} \frac{4}{n\pi} \frac{1}{Z_{n0}} \left[M X_{Csn0} \cdot \cos(n\omega_s t - n\theta) - (X_{Ltn0} + X_{Csn0}) \left[\frac{(1 - \cos(n\delta))}{2} \right] \cdot \cos(n\omega_s t) \right] \quad (4.9)$$

$$i_{Lt0}(t) = \sum_{n=1,3,5\dots}^{\infty} \frac{4}{n\pi} \frac{1}{Z_{n0}} \left[M (X_{Lsn0} + X_{Csn0}) \cdot \cos(n\omega_s t - n\theta) - X_{Csn0} \left[\frac{(1 - \cos(n\delta))}{2} \right] \cdot \cos(n\omega_s t) \right] \quad (4.10)$$

where,

$$Z_{n0} = X_{Lsn0} X_{Ltn0} + X_{Csn0} (X_{Lsn0} + X_{Ltn0})$$

The normalized voltage across C_s is:

$$v_{Cs0}(t) = (i_{Ls0}(t) - i_{Lt0}(t)) \cdot j X_{Csn0}$$

$$v_{Cs0}(t) = \sum_{n=1,3,5\dots}^{\infty} \frac{4}{n\pi} \frac{X_{Csn0}}{Z_{n0}} \left[X_{Ltn0} [(1 - \cos(n\delta))/2] \cdot \sin(n\omega_s t) + \right. \\ \left. M X_{Lsn0} \cdot \sin(n\omega_s t - n\theta) \right] \quad (4.11)$$

The normalized resonant inductor current i_{Ls0} can be written in time domain as,

$$i_{Ls0}(t) = \sum_{n=1,3,5\dots}^{\infty} i_{Lsn0p} \cdot \sin(n\omega_s t - n\phi) \quad (4.12)$$

where,

$$i_{Lsn0p} = (i_{Lsn0p1}^2 + i_{Lsn0p2}^2)^{(1/2)}$$

and

$$i_{Lsn0p1} = \frac{4}{n\pi} \frac{1}{Z_{n0}} \left[M X_{Csn0} \cdot \cos(n\theta) - (X_{Ltn0} + X_{Csn0}) [(1 - \cos(n\delta))/2] \right],$$

$$i_{Lsn0p2} = \frac{4}{n\pi} \frac{1}{Z_{n0}} M X_{Csn0} \sin(n\theta);$$

$$\phi = \tan^{-1} \left(i_{Lsn0p1} / i_{Lsn0p2} \right)$$

The normalized total external inductor current i_{Lt0} can be written in time domain as,

$$i_{Lt0}(t) = \sum_{n=1,3,5\dots}^{\infty} i_{Ltn0p} \cdot \sin(n\omega_s t + \gamma_{n1}) \quad (4.13)$$

where,

$$i_{Ltn0p} = (i_{Ltn0p1}^2 + i_{Ltn0p2}^2)^{(1/2)}$$

and

$$i_{Ltn0p1} = \frac{4}{n\pi} \frac{1}{Z_{n0}} \left[M (X_{Lsn0} + X_{Csn0}) \cos(n\theta) - X_{Csn0} [(1 - \cos(n\delta))/2] \right],$$

$$i_{Ltn0p2} = \frac{4}{n\pi} \frac{1}{Z_{n0}} M (X_{Lsn0} + X_{Csn0}) \sin(n\theta);$$

$$\gamma_{n1} = \tan^{-1} \left(-i_{Ltn0p1} / i_{Ltn0p2} \right)$$

The normalized resonant capacitor voltage v_{Cs0} can be written in time domain as,

$$v_{Cs0}(t) = \sum_{n=1,3,5\dots}^{\infty} v_{Csn0p} \cdot \sin(n\omega_s t + \gamma_{n2}) \quad (4.14)$$

where,

$$v_{Csn0p} = (v_{Csn0p1}^2 + v_{Csn0p2}^2)^{(1/2)}$$

and

$$v_{Csn0p1} = \frac{4}{n\pi} \frac{X_{Csn0}}{Z_{n0}} \left[MX_{Lsn0} \cos(n\theta) + X_{Ltn0} [(1 - \cos(n\delta))/2] \right],$$

$$v_{Csn0p2} = \frac{4}{n\pi} \frac{X_{Csn0}}{Z_{n0}} \left[-MX_{Lsn0} \sin(n\theta) \right];$$

$$\gamma_{n2} = \tan^{-1} \left(-v_{Csn0p1} / v_{Csn0p2} \right)$$

The RMS values of current through inductors i_{Ls} and i_{Lt} and voltage across capacitor v_{Cs} are

$$i_{Ls0r}(t) = \left[\sum_{n=1,3,5\dots}^{\infty} i_{Lsn0p}^2 \right]^{(1/2)} \cdot \frac{1}{\sqrt{2}} \quad (4.15)$$

$$i_{Lt0r}(t) = \left[\sum_{n=1,3,5\dots}^{\infty} i_{Ltn0p}^2 \right]^{(1/2)} \cdot \frac{1}{\sqrt{2}} \quad (4.16)$$

$$v_{Cs0r}(t) = \left[\sum_{n=1,3,5\dots}^{\infty} v_{Csn0p}^2 \right]^{(1/2)} \cdot \frac{1}{\sqrt{2}} \quad (4.17)$$

The load current I'_o is the average value of i'_o . However, for $0 \leq \omega_s t \leq \pi$, $i'_o = i_{Lt}$ as given in (4.10). Therefore, the normalized I'_o (i.e., J) is computed as:

$$J = \frac{1}{\pi} \int_0^{\pi} i_{Lt0}(t) d(\omega_s t)$$

$$J = \sum_{n=1,3,5\dots}^{\infty} \frac{8}{n^2 \pi^2 Z_n} X_{Csn} \sin(n\theta) [(1 - \cos n\delta)/2] \quad (4.18)$$

To solve (4.5) to (4.10), the initial value of ' θ ' is required to be determined. This

can be done by solving (4.10) numerically for all harmonics. Since, the rectifier input current (i_{rect}) is in phase with the rectifier input voltage (v_{rect}), the i_{rect} in (4.10) is zero at $\omega_s t = \theta$. Therefore, (4.10) can be rewritten (by substituting, $i_{rect} = 0$ and $\omega_s t = \theta$) as:

$$0 = \sum_{n=1,3,5\dots}^{\infty} \frac{4}{n\pi} \frac{1}{Z_{n0}} \left[M(X_{Lsn0} + X_{Csn0}) - X_{Csn0}[(1 - \cos n\delta)/2] \cdot \cos(n\theta) \right]$$

$$\cos(n\theta) = M \left(1 + \frac{X_{Lsn0}}{X_{Csn0}} \right) \left[\frac{2}{1 - \cos(n\delta)} \right] \quad (4.19)$$

The initial value of θ is calculated only for $n = 1$ to simplify the calculation in (4.19). therefore, from (4.19), the initial value of $\theta = \theta_1$ is obtained as:

$$\cos(\theta_1) = M \left(1 + \frac{X_{Ls10}}{X_{Cs10}} \right) \left[\frac{2}{1 - \cos(\delta)} \right] \quad (4.20)$$

The kVA/kW rating of resonant tank circuit can be calculated by using RMS values:

$$\frac{kVA}{kW} = \frac{I_{Ls0r}^2 X_{Lsn0} + I_{Cs0r}^2 X_{Csn0} + I_{Lt0r}^2 X_{Ltn0}}{P_o} \quad (4.21)$$

where, P_o is the rated output power.

The resonant network components L_s , C_s , and L_t can be obtained by using (4.1) and (4.2) with the following expressions (Bhat, 1995a)

$$L_s = \frac{Z_B}{\omega_r} = \frac{M J V_B^2 F}{2\pi f_s P_o} \quad (4.22)$$

$$C_s = \frac{1}{Z_B \omega_r} = \frac{P_o F}{2\pi f_s M J V_B^2} \quad (4.23)$$

$$L_t = K L_s \quad (4.24)$$

4.2.4 ZVS CONDITIONS

To realize ZVS operation of all switches, the necessary condition is that the anti-parallel diode of respective switches should conduct prior to the switch. Therefore, to ascertain ZVS, expression for current through the switches is obtained as given in (4.25) - (4.27) and the initial current is verified to be negative. The negative switch current indicates conduction of anti-parallel diode. This happens when the current

through the resonant circuit/switch lags the inverter output voltage. For the proposed modulation scheme as given in Fig. 4.2, the initial current for switches S_1 and S_2 is determined by substituting $\omega_s t = 0$ in the expression for current given in (4.12). Similarly, for Switch S_3 , the initial current is found by substituting $\omega_s t = (\pi - \alpha)$ in the expression for current given in (4.12) and for switch S_4 , the initial current is found by substituting $\omega_s t = (\pi + \alpha)$ in the expression for current given in (4.12). The ZVS condition (i.e., the initial switch current) for all the switches is given below:

Initial current through switches S_1 and S_2 (i_{s12}) is:

$$i_{S12}(0) = i_{Ls0}(t) = \sum_{n=1,3,5\dots}^{\infty} i_{Lsn0p} \cdot \sin(n\omega_s t - n\phi) < 0 @\omega_s t = 0 \quad (4.25)$$

where, $\phi < \pi$.

Initial current through switches S_3 (i_{s3}) is:

$$i_{S3}(0) = -i_{Ls0}(t) = - \sum_{n=1,3,5\dots}^{\infty} i_{Lsn0p} \cdot \sin(n\omega_s t - n\phi) < 0 @\omega_s t = \pi - \alpha \quad (4.26)$$

where, $\phi < \pi$.

Initial current through switches S_4 (i_{s4}) is:

$$i_{S4}(0) = -i_{Ls0}(t) = - \sum_{n=1,3,5\dots}^{\infty} i_{Lsn0p} \cdot \sin(n\omega_s t - n\phi) < 0 @\omega_s t = \pi + \alpha \quad (4.27)$$

where, $\alpha < \phi < \pi$.

4.3 DESIGN

The specifications of the proposed fixed-frequency modified gating signals controlled LCL-T resonant converter are formulated as given in Table 3.1. Selection of optimum design parameters such as frequency ratio (F), inductor ratio (K), and the DC voltage gain (M) is critical in making the converter design compact and efficient. These design parameters can be selected by using the design curves presented in Figs. 4.5-4.7. The analysis presented in Section 4.2 is used in plotting the design curves. The effect of harmonics of the order greater than 100 is negligible, hence are not considered in the voltage and current waveforms. The converter is designed to operate with lagging

current by choosing $F > 1$. The converter is designed for the worst-case operating condition, i.e., minimum input voltage and full-load, and at this condition the pulse width angle $\delta = \pi$ is used.

4.3.1 DESIGN TRADE-OFFS

Figs. 4.5(a) and (b) shows the design curves of resonant tank kVA/kW with respect to converter gain (M) for different values of frequency ratio (F) and inductor's ratio (K) respectively. The following observations are made from Fig. 4.5:

- kVA/kW of resonant tank decreases with decreases in F from Fig. 4.5(a), and this is not drastic after $F \leq 1.4$.
- kVA/kW of resonant tank decreases with decrease in K from Fig. 4.5(b), but this decrement is not much after $K \leq 0.8$.
- kVA/kW of resonant tank decreases with increase in M (Figs. 4.5(a) and (b)), hence M should be selected close to 1.

In Fig. 4.6, the variations of peak resonant current (I_{Lsp}) versus voltage gain (M) for varying frequency ration (F) with $K = 0.8$ (Fig. 4.6(a)) and $K = 1$ (Fig. 4.6(b))

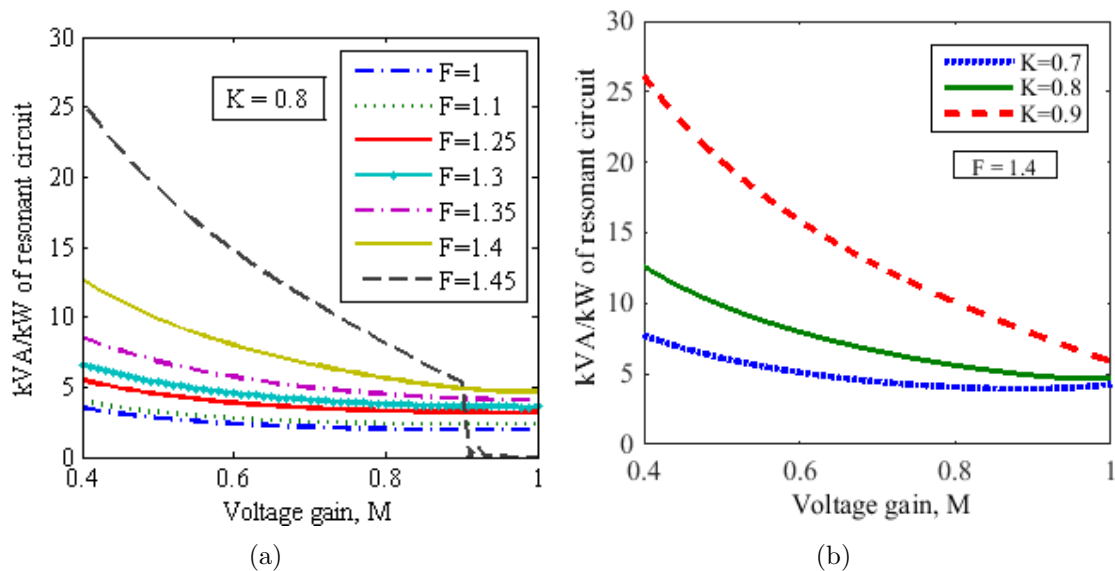


Figure 4.5: Variation of resonant tank kVA/kW versus converter gain (M): (a) for different values of F with $K = 0.8$, and (b) for different values of K with $F = 1.4$.

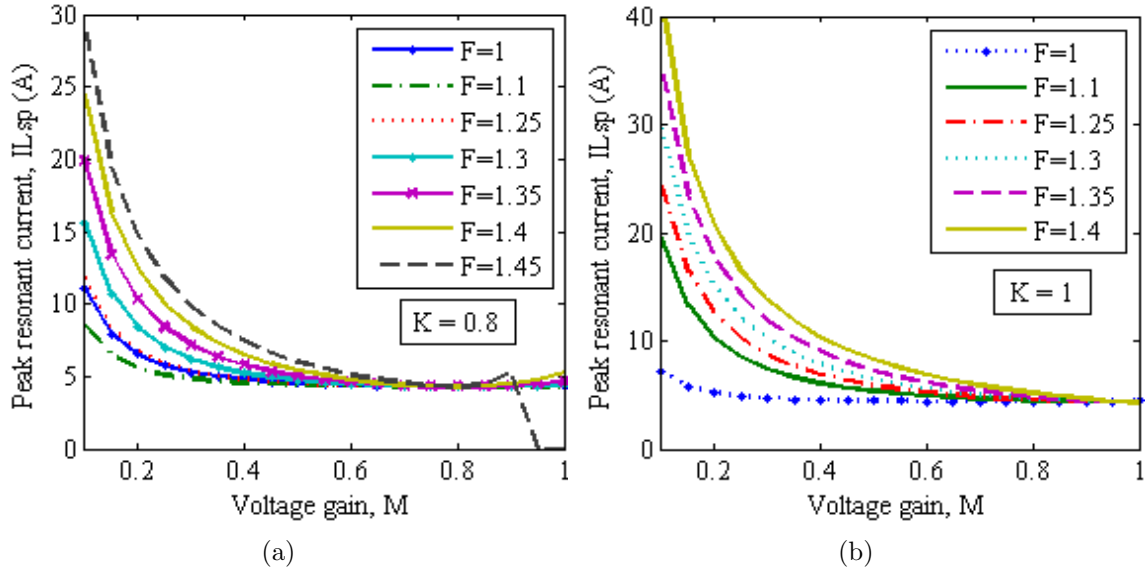


Figure 4.6: Variation of peak resonant current (I_{Lsp}) versus converter gain (M) for variations in F with: (a) $K = 0.8$, and (b) $K = 1$.

are shown. The following observations are made from Fig. 4.6:

- increase in F increases I_{Lsp} and further increases with increase in K .
- I_{Lsp} is minimum at $M = 0.8$ with $K = 0.8$ for $F = 1.4$ compared to the other

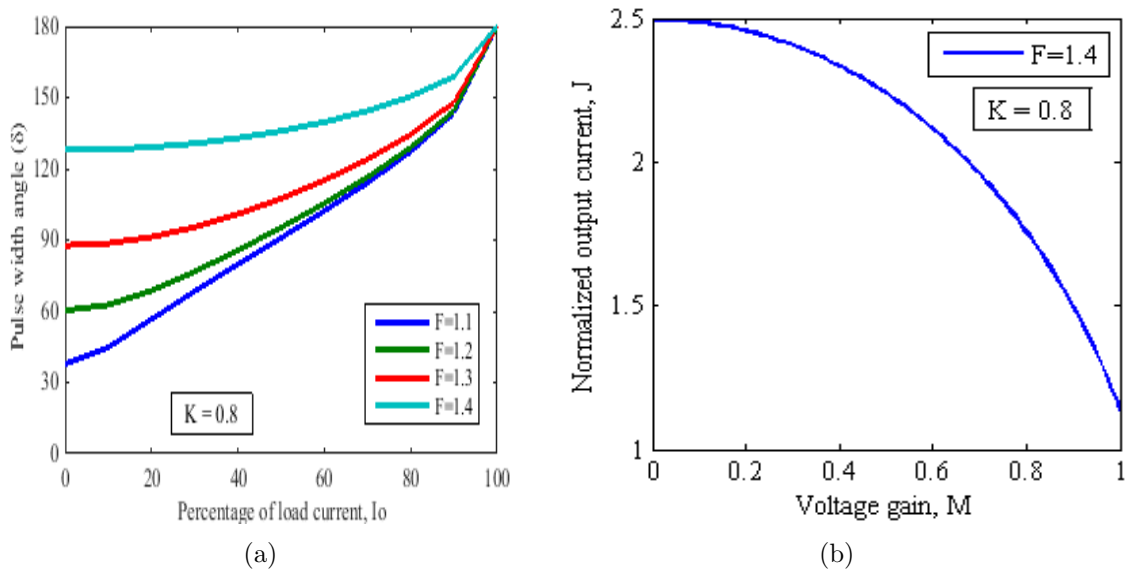


Figure 4.7: Variation of: (a) pulse width angle (δ) versus percentage of load current, and (b) normalized output current (J) versus M with $K = 0.8$.

values of F .

The curves of pulse width angle (δ) versus percentage of load current (I_o) for variation of F are shown in Fig. 4.7(a) with $K = 0.8$. It can be observed that, the required pulse width angle (δ) for regulating the output voltage for variations in the input voltage and the load is very less at $F = 1.4$ compared to other values of F shown in Fig. 4.7(a). Therefore, based on above observations $F = 1.4$, $K = 0.8$ and $M = 0.8$ are chosen as optimum parameters for the design. The graph of normalized output current (J) versus voltage gain (M) for the chosen values of F and K is shown in Fig. 4.7(b). Therefore, J can be read as 1.75 for the chosen value of M , from Fig. 4.7(b).

The steps involved in calculation of circuit elements for the selected optimum

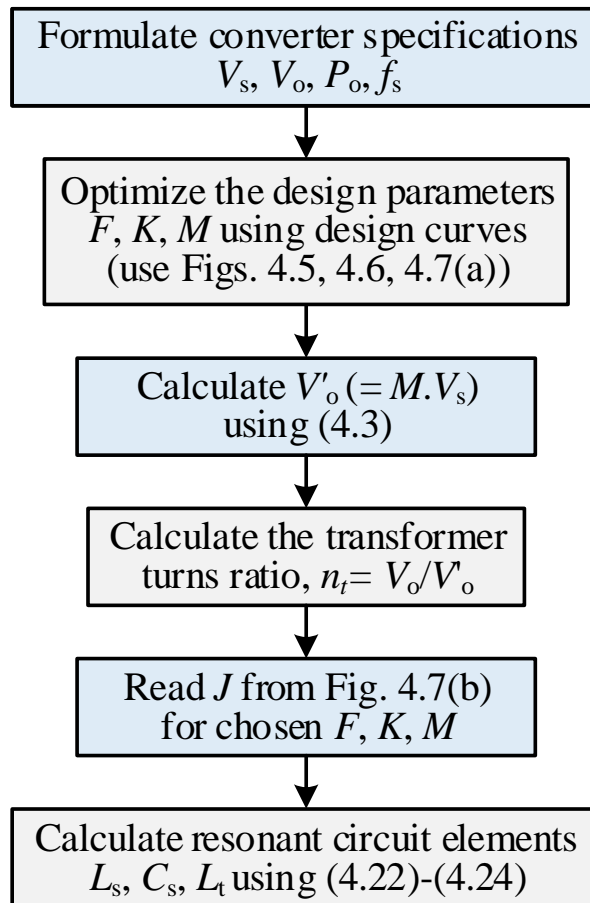


Figure 4.8: Block diagram indicating the steps involved in converter design.

design parameters with minimum input voltage V_s are as follows

Step-1: from (4.3), the output voltage referred to primary side of the HF transformer is calculated as, $V'_o = MV_s = 88$ V.

Step-2: The transformer turns ratio, 1: $n_t = 1$: $(V_o/V'_o) = 1:2.5$.

Step-3: The resonant tank elements L_s , C_s , and L_t are calculated by using (4.22)-(4.23) as $L_s = 126.21$ μ H; $C_s = 39.33$ nF; $L_t = 100.92$ μ H.

Step-4: The calculated peak values of current and voltage of resonant elements using (4.12) - (4.14) are: $I_{Lsp} = 4.36$ A, $I_{Ltp} = 5.38$ A, $V_{Csp} = 367.7$ V.

The block diagram indicating the steps involved in converter design is given in Fig. 4.8.

4.4 SIMULATION RESULTS

PSIM software tool is used to simulate the performance of the proposed converter. The following six cases are considered for exhaustive performance validation of the converter in steady-state:

- Case-1: $V_s(\text{min.}) = 110$ V, full-load
- Case-2: $V_s(\text{min.}) = 110$ V, half-load
- Case-3: $V_s(\text{min.}) = 110$ V, 10% of full-load
- Case-4: $V_s(\text{max.}) = 180$ V, full-load
- Case-5: $V_s(\text{max.}) = 180$ V, half-load
- Case-6: $V_s(\text{max.}) = 180$ V, 10% of full-load

In the simulation for MOSFETs $R_{DS} = 0.45$ Ω and for output rectifier diodes a voltage of 1 V is set as forward voltage drop. All other elements are chosen to be ideal. Open loop control is used to regulate the output voltage for changes in input voltage and load. The pulse-width angle δ is changed manually to maintain the output voltage constant at its full-load value by changing the angle α as indicated in Fig. 4.1. The block diagram of control process in the event of changes in load/input voltage is

shown in Fig. 4.9. Since manual control is used several iterations are required to determine the value of δ for the given input voltage/loading condition. Some of the important simulation waveforms are presented in Figs. 4.10 and 4.11 for all cases. In Figs. 4.10(a) and 4.11(a) the voltage across each switch (v_{s1} , v_{s2} , v_{s3} , and v_{s4}) and current through respective switches (i_{s1} , i_{s2} , i_{s3} , and i_{s4}) are shown to check zero-voltage switching (ZVS). It can be seen from Fig. 4.10(a) that, the switch voltage

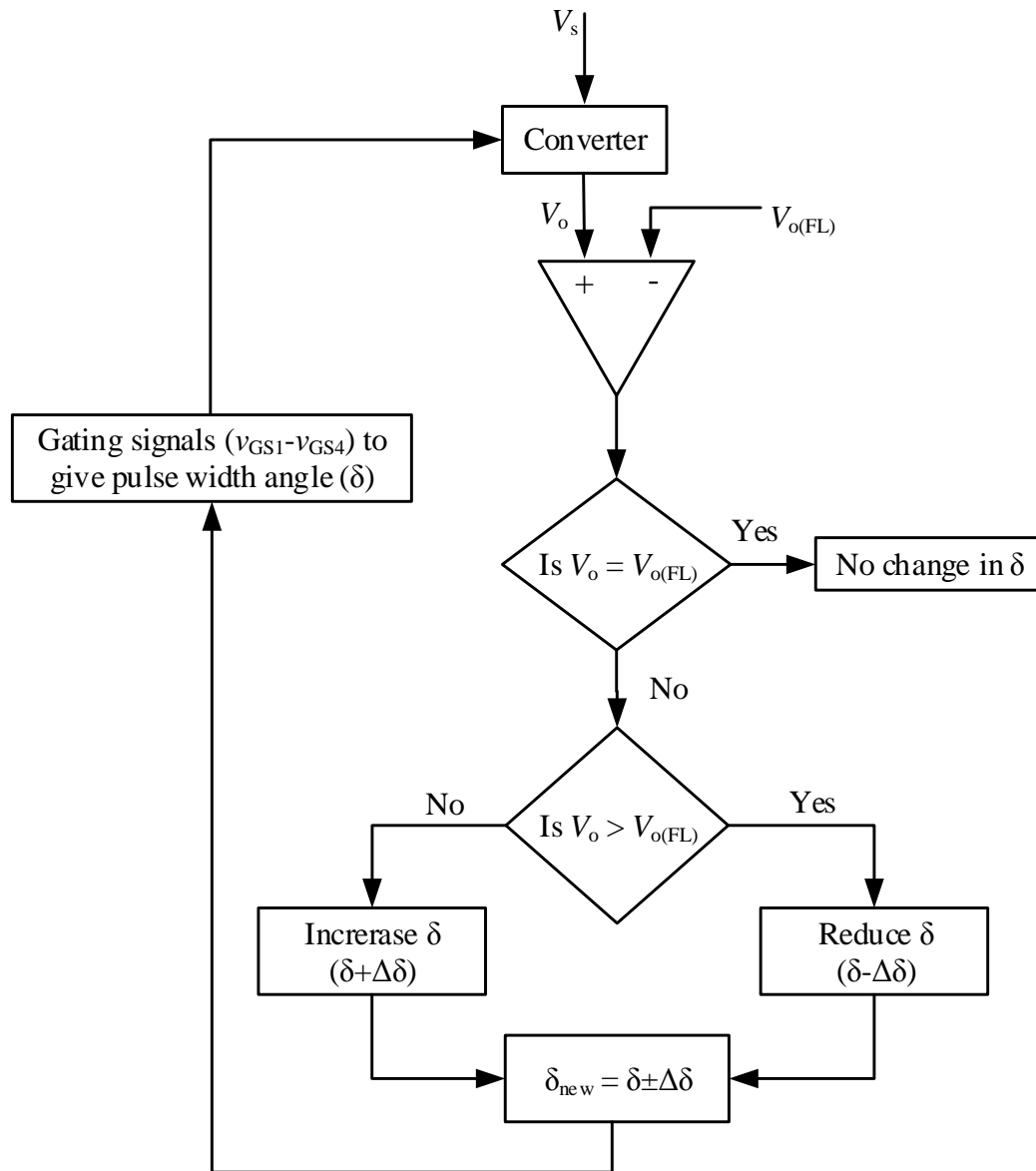


Figure 4.9: The block diagram of control process in the event of changes in load/input voltage.

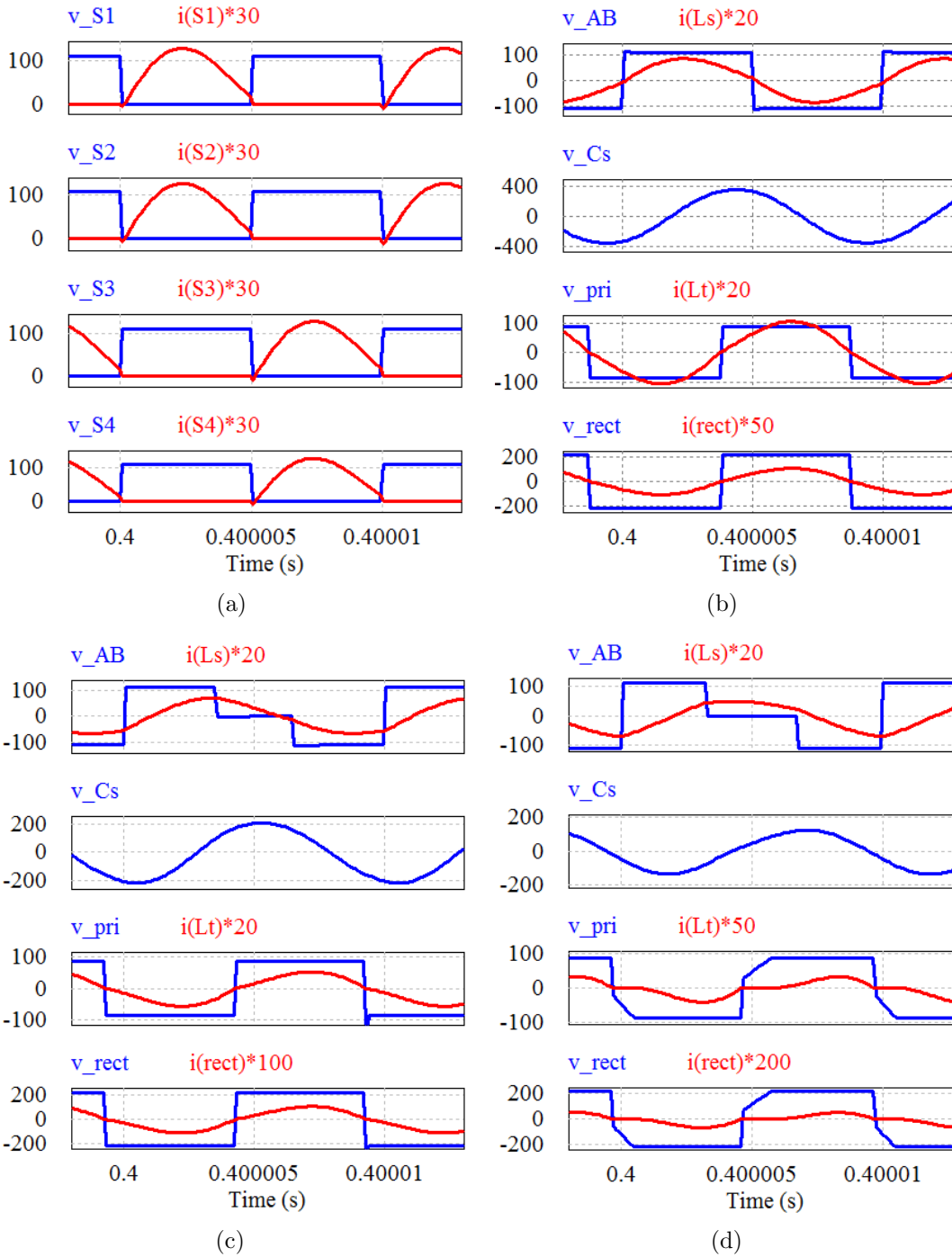


Figure 4.10: Simulation waveforms with $V_s(\text{min.}) = 110 \text{ V}$: (a) inverter switch currents and voltages to show ZVS in full load, $R_L = 161.17 \Omega$. Waveforms of v_{AB} , i_{Ls} , v_{Cs} , v_{pri} , i_{Lt} , v_{rect} and i_{rect} at: (b) full load ($R_L = 161.17 \Omega$), (c) half load ($R_L = 322.34 \Omega$), (d) 10% of full load ($R_L = 1611.7 \Omega$).

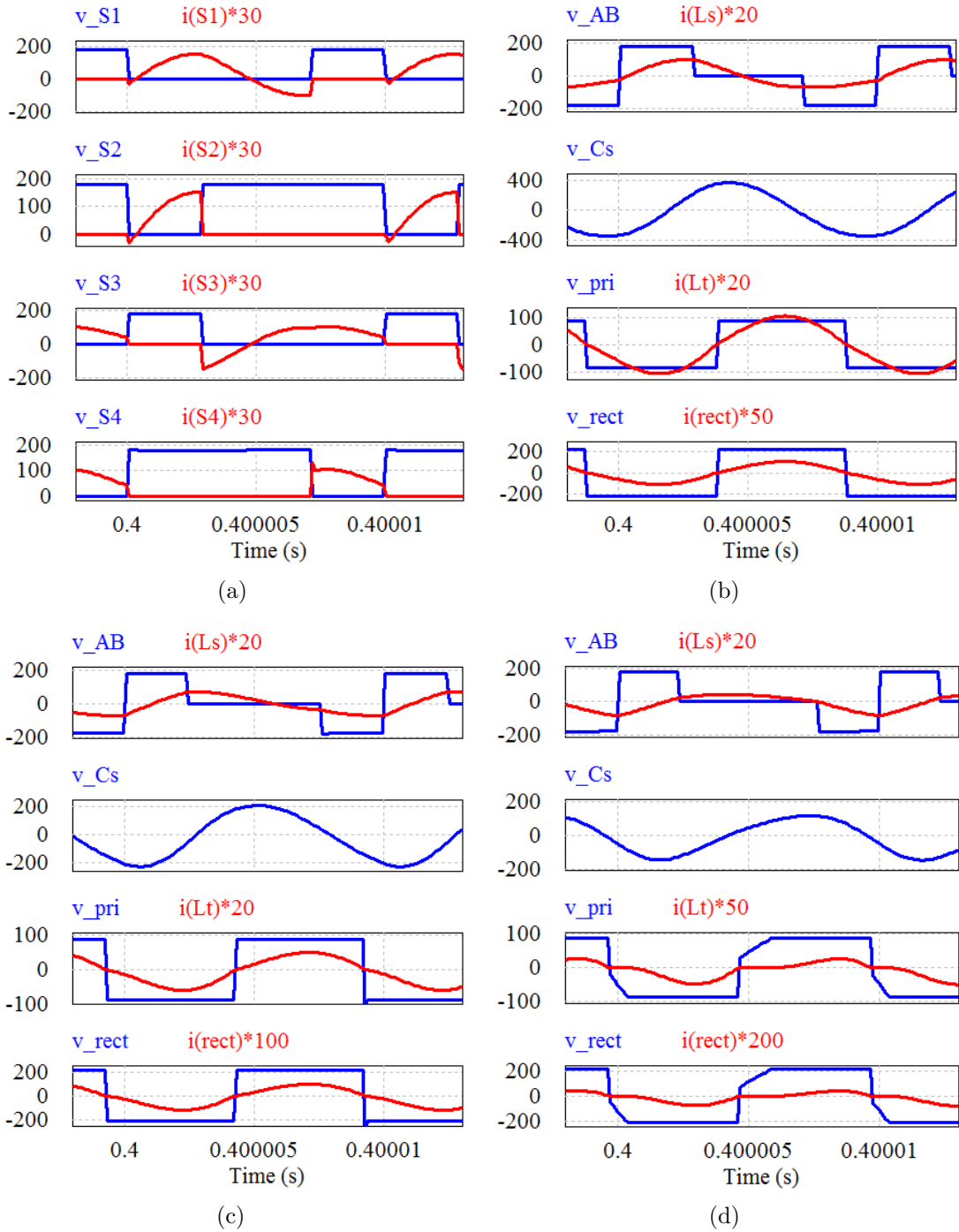


Figure 4.11: Simulation waveforms with $V_s(\text{max.}) = 180 \text{ V}$: (a) inverter switch currents and voltages to show ZVS in full load, $R_L = 161.17 \Omega$. Waveforms of v_{AB} , i_{Ls} , v_{Cs} , v_{pri} , i_{Lt} , v_{rect} and i_{rect} at: (b) full load ($R_L = 161.17 \Omega$), (c) half load ($R_L = 322.34 \Omega$), (d) 10% of full load ($R_L = 1611.7 \Omega$).

becomes zero before the switch current starts to rise in the positive direction for all the four switches hence, ZVS. This is true with the cases of minimum input voltage (i.e., cases 1, 2, and 3). However, in the cases of maximum input voltage (i.e., cases 4, 5, and 6), as it can be seen from Fig. 4.11(a) that only one switch loses ZVS. This is one of the main advantages of using modified gating signals as compared to the conventional gating signals, where two switches lose ZVS. Also, switch S_1 achieving ZCS as diode conduct before current jumps to zero. Also, from Figs. 4.11(a), it can be seen that the anti-parallel diode of switch S_1 conduct before current jumps to zero. Hence, switch S_1 turns-off with ZCS.

Figs. 4.10(b)-(d) shows the inverter output voltage (v_{AB}), resonant inductor current (i_{Ls}), resonant capacitor voltage (v_{Cs}), transformer primary voltage (v_{pri}), inductor current (i_{Lt}), and rectifier input voltage (v_{rect}) and current (i_{rect}) with the minimum input voltage. The same waveforms are shown in Fig. 4.11(b)-(d) with the maximum input voltage. The highest peak current through the resonant inductor (i.e., same switch current) is 4.41 A, and that occurs in case-4 ($V_s(\text{max.})$, full-load). The lowest peak current through inductor occurs in Case-3 ($V_s(\text{min.})$, 10% of full-load) and it is 2.94 A. To achieve higher efficiency at low load conditions, the peak resonant current has to decrease with the load. From Figs. 4.10 and 4.11, it can be observed that the peak resonant/switch current decreases as the load is decreased. Therefore, decreasing resonant current with load makes the LCL-T resonant converter efficient even at light load. The peak voltage stress that appears across each switch is the maximum value of the input voltage (i.e., 180 V). The maximum voltage stress across each output rectifier diodes is the value of the output voltage (i.e., 220 V).

In the simulations, the short-circuit fault is created during full-load steady-state operation by making the load resistance very small (i.e., $R_L = 161 \text{ m}\Omega$). The key waveforms in the event of load short-circuit fault is shown in Fig. 4.12(a) It is observed that the resonant/switch current does not shoot up to a large value when the load short-circuit takes place. No-load test is conducted by suddenly making the load resistance very large ($R_L = 161 \text{ K}\Omega$) during full-load steady-state operation. It is observed that the load voltage is maintained at its full-load value, thus the voltage is regulated even during no-load conditions. The key waveforms in the event of no-load are Fig. 4.12(b).

The power loss calculations of 300 W LCL-T resonant converter for a full load to low load (i.e., 10% of full load) with minimum and maximum input voltages are

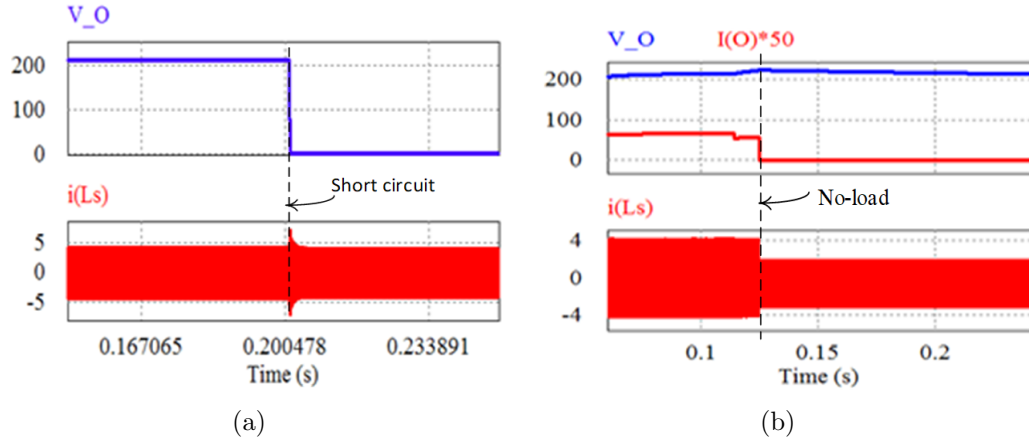


Figure 4.12: simulation waveforms of resonant/switch current (i_{L_s}) and output voltage (V_o) during (a) load short circuit test, (b) no-load test.

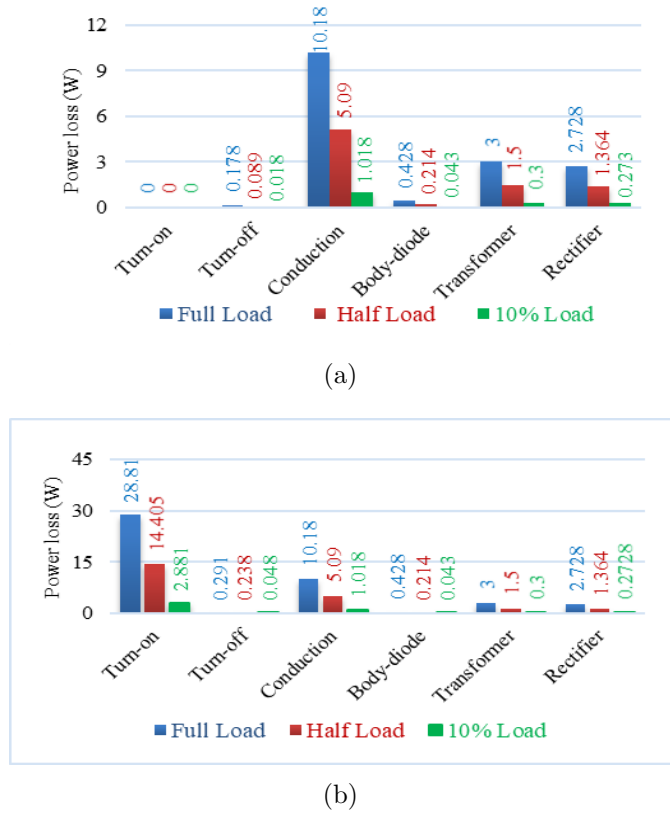


Figure 4.13: Power loss distribution of a 300 W LCL-T resonant power converter for full load to 10% of full load at: (a) the minimum input voltage (i.e., $V_s(\min.) = 110$ V), (b) the maximum input voltage (i.e., $V_s(\max.) = 180$ V).

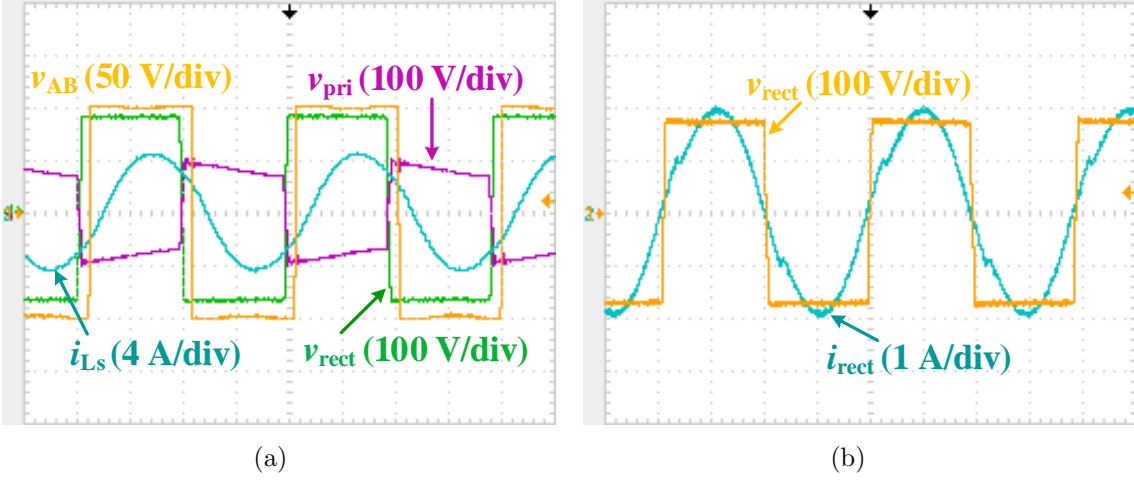


Figure 4.14: Experimental waveforms of case-1 ($V_s(\text{min.}) = 110 \text{ V}$ & full load, $R_L = 161.17 \Omega$): (a) v_{AB} , i_{L_s} , v_{pri} , v_{rect} ; (b) v_{rect} , i_{rect} .

given in Fig. 4.13. The following devices are chosen in the calculation of power losses. Inverter MOSFETs: IRF740, rectifier diode: UF5404. The transformer and Q losses are assumed to be 1% of output power.

4.5 EXPERIMENTAL RESULTS

A 300 W experimental setup of LCL-T resonant converter shown in Fig. 3.12 is built in the laboratory to validate the theoretical and simulation results. The details of the components used in building the converter circuit are listed in Table 4.1. The

Table 4.1: Details of the components used in experimental prototype

Component	Details
MOSFET switches (S_1 - S_4)	IRF740 (400V, 10A)
Resonant inductor (L_s)	122.81 μH
Resonant inductor (L_t)	94.8 μH
Resonant capacitor (C_s)	38.17 nF
HF transformer	Core: EE4215; Turns ratio: 16:40
Rectifier diodes (D_{r1} - D_{r4})	UF5404 (400 V, 3 A)
Output capacitor (C_o)	470 μF (400 V)

high-frequency transformer is built using the EE4215 ferrite core and litz wire. The resonant inductor L_s is built using the toroidal core, and 1.56 mm^2 litz wire of 45 turns. The designed values of the converter components are given in Section 4.3. The measured value of L_s using LCR meter (GW Instek 6300) is $122.81 \mu\text{H}$ at 100 kHz. The measured value of total leakage inductance referred to the primary side is $3.45 \mu\text{H}$. Since the leakage inductance of the transformer is used as part of L_t , an external inductance of $(98.25 \mu\text{H} - 3.45 \mu\text{H})$ $94.8 \mu\text{H}$ is built and connected at the primary side of the transformer. The gating signals of 3.75 V are generated using Nexys DDR4 artex-7 FPGA board. Driver circuit is developed to scale up the voltage to 15 V so as to drive the MOSFETs. Since the built values of resonant inductor and resonant capacitor are slightly different from the actual designed values, the switching frequency of the converter was recalculated using (4.2) to have 103 kHz. Some of the experimental waveforms are presented in Figs. 4.14-4.19. In these Figs. 4.14-4.19, waveforms are arranged as following:

- (a): inverter output voltage (v_{AB}); resonant inductor current (i_{L_s}); transformer primary voltage (v_{pri}); and voltage at the input terminals of rectifier block (v_{rect}).
- (b): voltage (v_{rect}) across and current (i_{rect}) through the input terminals of diode rectifier.

The peak inverter output current/switch current decreases from 4.75 A at $V_s(\text{max.}) = 180 \text{ V}$, full-load (Fig. 4.17(a)) to 2.82 A at $V_s(\text{min.}) = 110 \text{ V}$, 10% of full-load

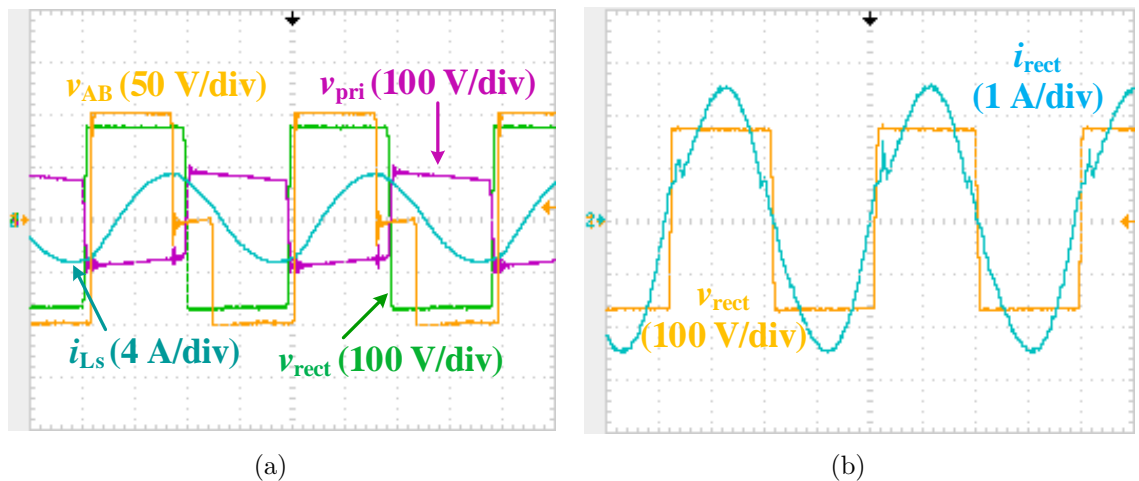


Figure 4.15: Experimental waveforms of case-2 ($V_s(\text{min.}) = 110 \text{ V}$ & half load, $R_L = 322.34 \Omega$): (a) v_{AB} , i_{L_s} , v_{pri} , v_{rect} ; (b) v_{rect} , i_{rect} .

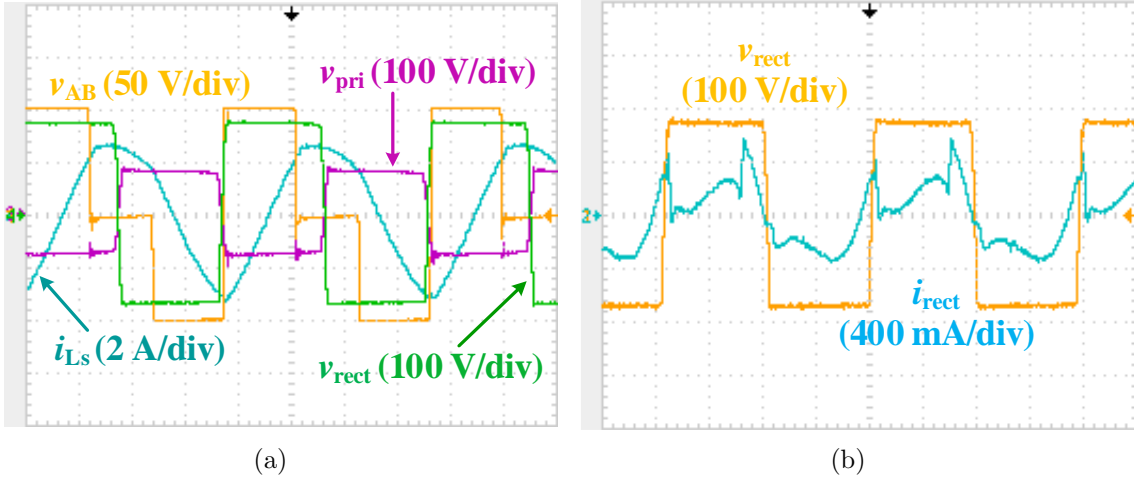


Figure 4.16: Experimental waveforms of case-3 ($V_s(\text{min.}) = 110 \text{ V}$ & 10% of full load, $R_L = 1611.7 \Omega$): (a) v_{AB} , i_{Ls} , v_{pri} , v_{rect} ; (b) v_{rect} , i_{rect} .

(Fig. 4.16(a)). The results obtained from calculations, simulations and experiment are presented in Table 4.2 for comparison. It is worth noting here that, the fall in peak current is not proportionally decreasing with the load. This indicates that the proposed converter topology is more close to the parallel resonant converter topology, where the light load efficiency is low.

The efficiency comparison plot of theoretical, simulation, and experimental results

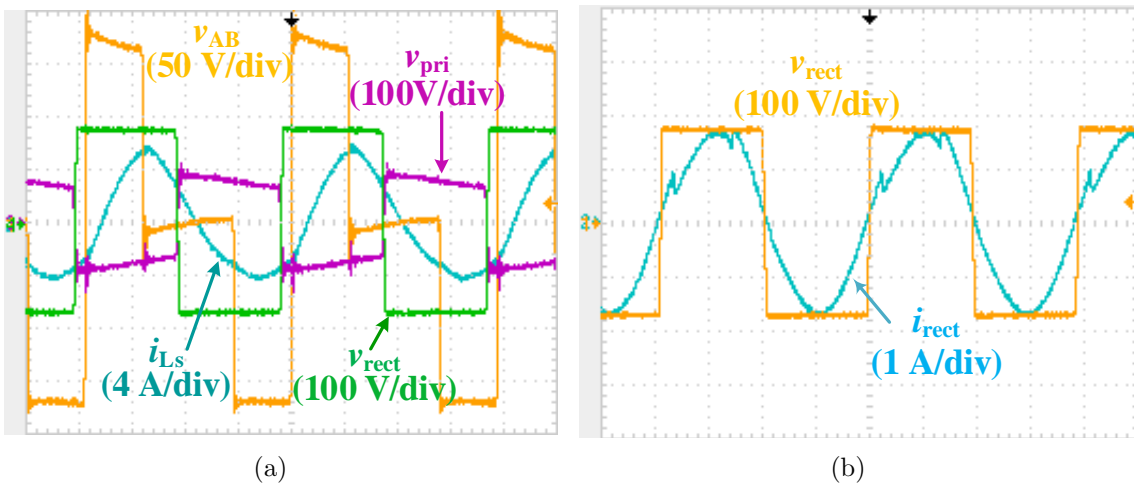


Figure 4.17: Experimental waveforms for case-4 ($V_s(\text{max.}) = 180 \text{ V}$ & full load, $R_L = 161.17 \Omega$): (a) v_{AB} , i_{Ls} , v_{pri} , v_{rect} ; (b) v_{rect} , i_{rect} .

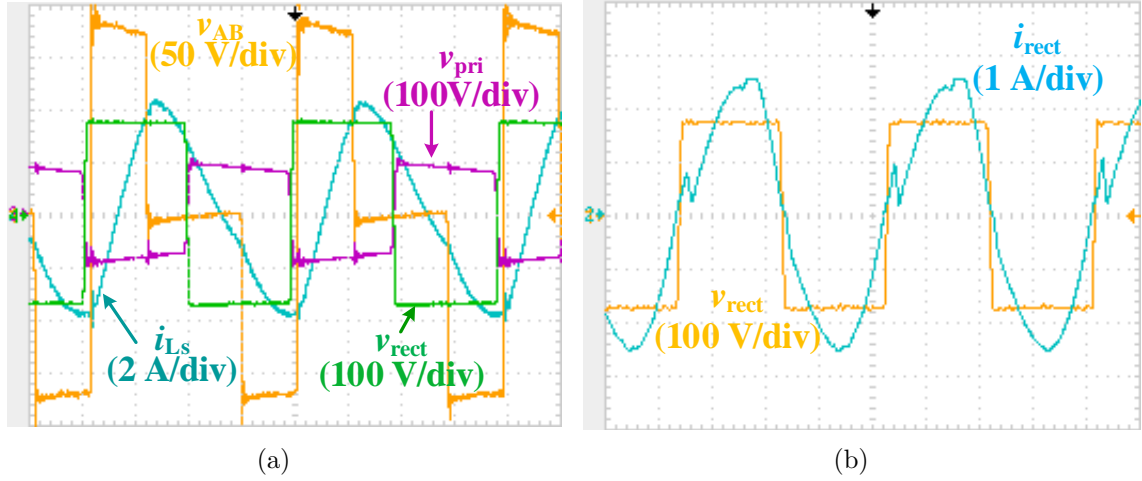


Figure 4.18: Experimental waveforms for case-5 ($V_s(\text{max.}) = 180 \text{ V}$ & half load, $R_L = 322.34 \Omega$): (a) v_{AB} , i_{Ls} , v_{pri} , v_{rect} ; (b) v_{rect} , i_{rect} .

for different loading conditions at the minimum input voltage (i.e., $V_s(\text{min.}) = 110 \text{ V}$) and the maximum input voltage (i.e., $V_s(\text{max.}) = 180 \text{ V}$) is shown in Fig. 4.20.

The possible reasons for the discrepancy between these results are:

1. All switches, diodes, inductors, capacitors, and HF transformer are treated as ideal in theoretical calculations. In simulations, the drain to source resistance $R_{DS(\text{on})} = 0.45 \Omega$ in MOSFETs (IRF 740) and a voltage drop of 1 V in rectifier diodes (UF5404) are set and all other elements are chosen to be ideal. But in

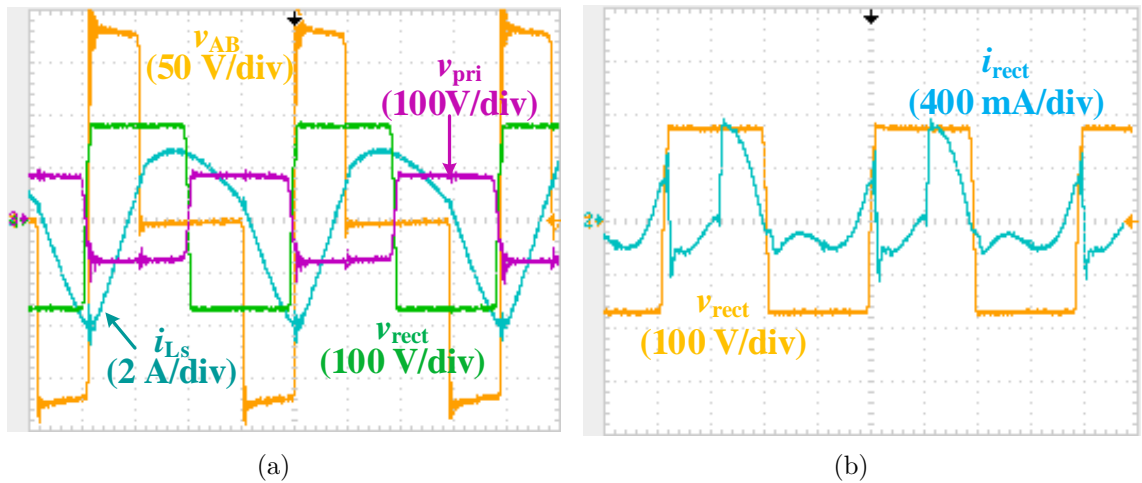


Figure 4.19: Experimental waveforms for case-6 ($V_s(\text{max.}) = 180 \text{ V}$ & 10% of full load, $R_L = 1611.7 \Omega$): (a) v_{AB} , i_{Ls} , v_{pri} , v_{rect} ; (b) v_{rect} , i_{rect} .

Table 4.2: Comparison of theoretical, simulation, and experimental results

Parameters	Case-1:			Case-2:			Case-3:		
	$V_s(\text{min.}), \text{ Full Load}$			$V_s(\text{min.}), \text{ Half Load}$			$V_s(\text{min.}), \text{ 10\% Load}$		
	Cal.	Sim.	Exp.	Cal.	Sim.	Exp.	Cal.	Sim.	Exp.
V_o (V)	220	214.62	199	220	214.68	202	220	214.62	196
I_o (V)	1.36	1.33	1.29	0.68	0.66	0.63	0.136	0.133	0.13
δ ($^\circ$)	180	180	176.3	131.6	126	142.9	122.8	116	122.5
I_{Lsr} (A)	3.04	2.99	3.04	1.52	2.41	2.4	0.3	2.08	2
I_{Ltr} (A)	3.80	3.70	3.425	1.90	1.89	1.75	0.38	0.45	0.29
V_{Csr} (V)	260	253	254	130	152	163	26	93	90
I_{in} (A)	2.72	2.703	2.57	1.36	1.41	1.34	0.27	0.28	0.26
η (%)	94.78	96	90.8	94.78	91.35	90.44	94.78	92.6	90
ZVS	All the four switches from S_1 to S_4 will have ZVS								
Parameters	Case-4:			Case-5:			Case-6:		
	$V_s(\text{max.}), \text{ Full Load}$			$V_s(\text{max.}), \text{ Half Load}$			$V_s(\text{max.}), \text{ 10\% Load}$		
	Cal.	Sim.	Exp.	Cal.	Sim.	Exp.	Cal.	Sim.	Exp.
V_o (V)	220	214.73	197	220	213.56	206	220	214.22	196
I_o (V)	1.36	1.33	1.27	0.68	0.66	0.61	0.136	0.133	0.14
δ ($^\circ$)	102.7	103	100.2	90.86	88	96.5	86.5	83	87.3
I_{Lsr} (A)	3.04	3.12	3.36	1.5	2.56	2.73	0.3	2.22	2.26
I_{Ltr} (A)	3.80	3.70	3.03	1.90	1.90	1.77	0.38	0.48	0.27
V_{Csr} (V)	260	253	251.12	130	153	182.1	26	94	102.4
I_{in} (A)	2.07	1.8	1.65	1.03	0.94	0.86	0.2	0.196	0.19
η (%)	86.85	88.14	84.23	86.85	83.3	81.17	86.85	80.75	80.2
ZVS	One of the four switches (S_4) lose ZVS								

practical circuits, components suffer from loss of voltage and power.

2. In calculations, power loss of 1% is used for the transformer. However, in

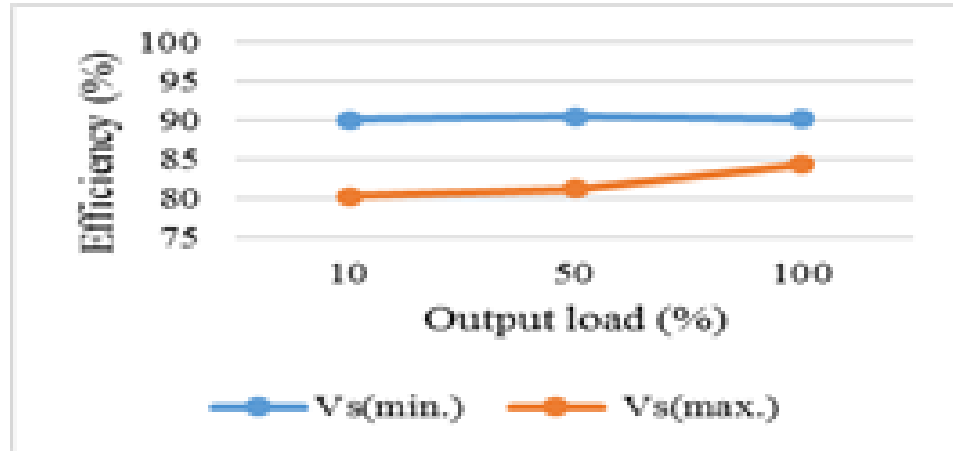


Figure 4.20: Experimental efficiency versus load.

experiments, only the copper loss changes with the load and core losses are constant.

3. In calculations, the component values as designed are used, while in practical circuit, there is small difference in these values due to the difficulties in building the exact value components in the laboratory.
4. No dead gap is accounted for in theoretical calculations. But, in the experiment nearly 150 ns dead gap is provided.

4.6 PERFORMANCE COMPARISON OF PSG AND MGS CONTROL SCHEMES

The performance of LCL-T DC-DC resonant power converter (RPC) when controlled with fixed-frequency modified-gating signals (MGS) and phase-shifted gating (PSG) control schemes is compared in this Section. The steady-state analysis of converter is carried-out using Fourier series approach for both control schemes.

The operating principle of PSG control scheme is explained in Section 3.1 and typical operating waveforms are shown in Fig. 3.2. The simulation results of PSG controlled LCL-T converter using Fourier series are given in Figs. 4.21 and 4.22. Since the voltage across switch becomes zero before the switch current starts to rise in the positive direction, there is ZVS for all the four switches. This is true with cases

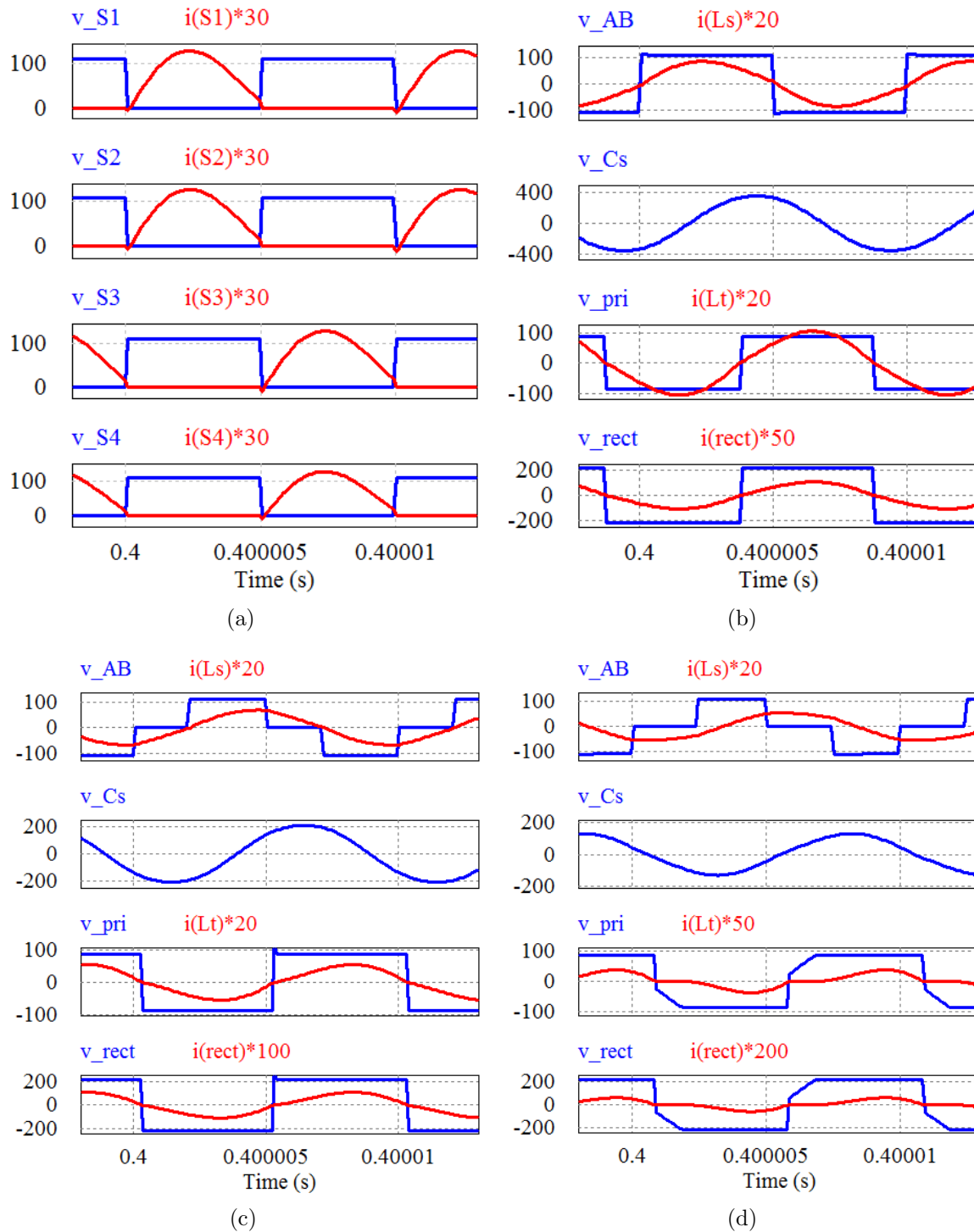


Figure 4.21: Simulation waveforms with $V_s(\text{min.}) = 110 \text{ V}$: (a) Inverter switch currents and voltages to show ZVS in full load, $R_L = 161.17 \Omega$. Waveforms of v_{AB} , i_{Ls} , v_{Cs} , v_{pri} , i_{Lt} , v_{rect} and i_{rect} at: (b) full load ($R_L = 161.17 \Omega$), (c) half load ($R_L = 322.34 \Omega$), (d) 10% of full load ($R_L = 1611.7 \Omega$).

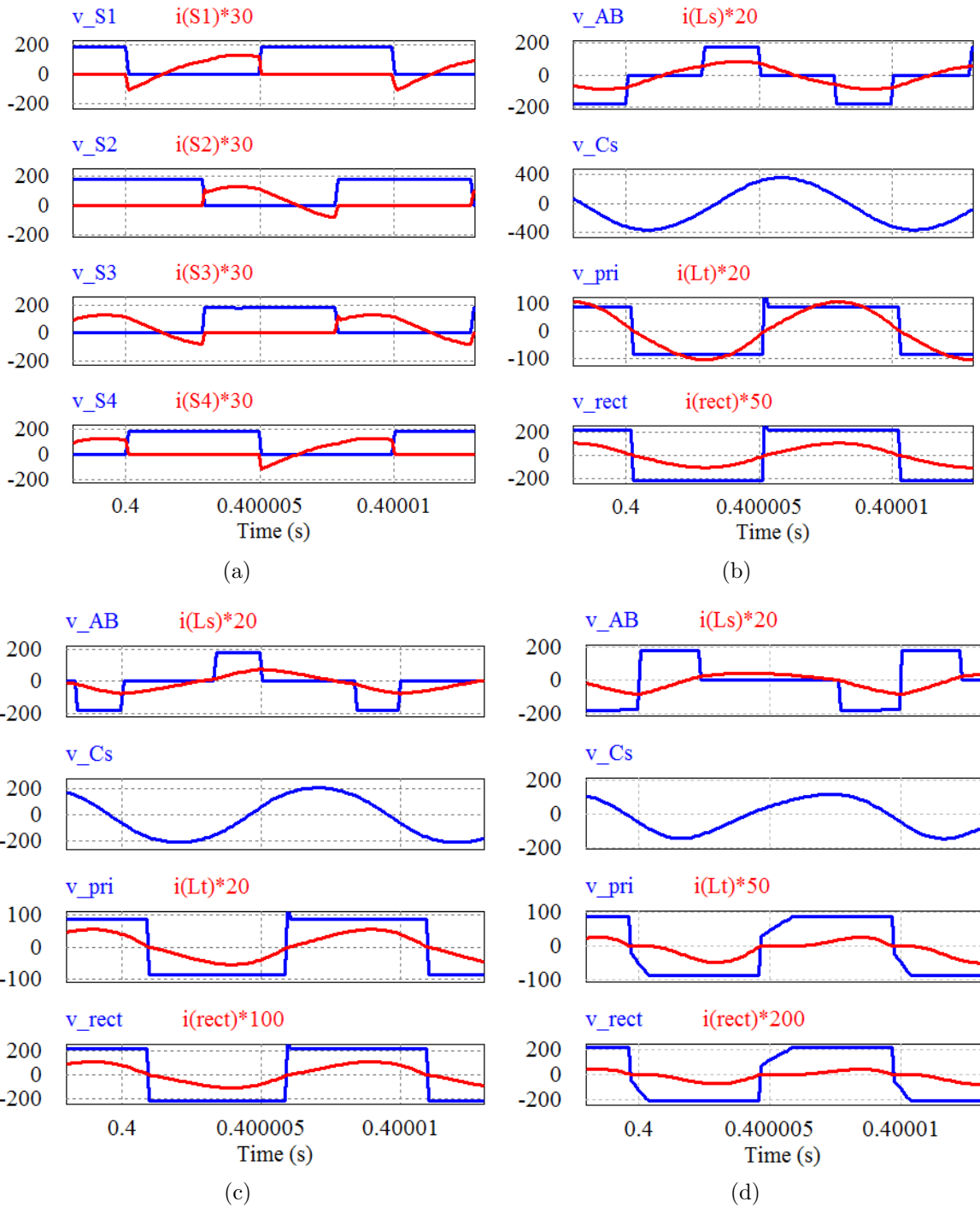
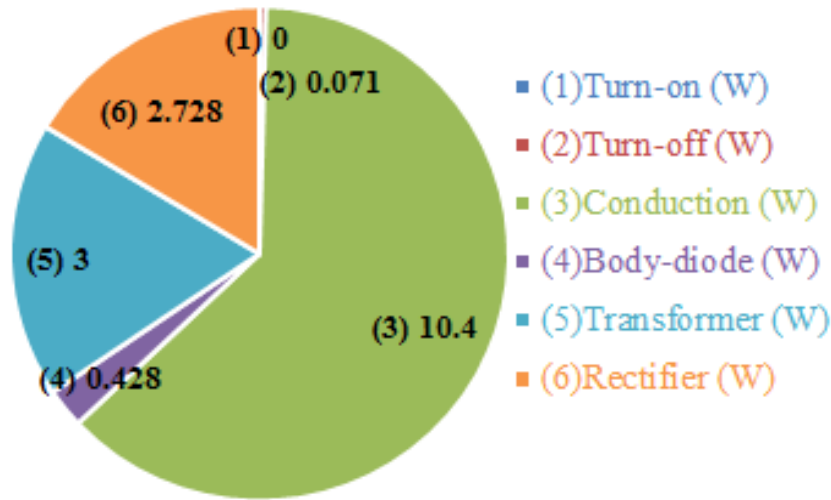
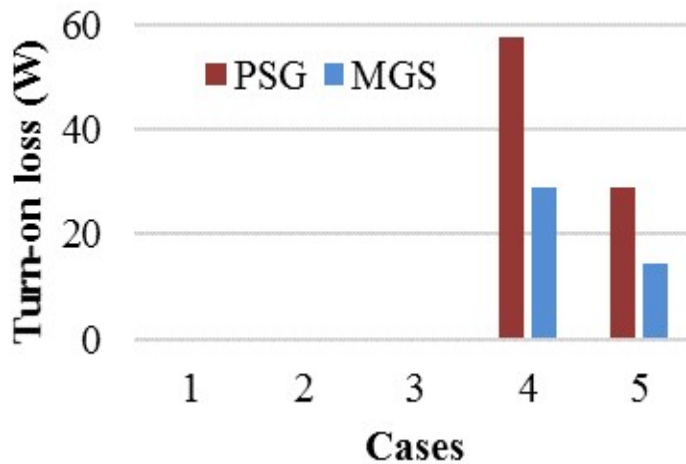


Figure 4.22: Simulation waveforms with $V_s(\text{max.}) = 180 \text{ V}$: (a) Inverter switch currents and voltages to show ZVS in full load, $R_L = 161.17 \Omega$. Waveforms of v_{AB} , i_{Ls} , v_{Cs} , v_{pri} , i_{Lt} , v_{rect} and i_{rect} at: (b) full load ($R_L = 161.17 \Omega$), (c) half load ($R_L = 322.34 \Omega$), (d) 10% of full load ($R_L = 1611.7 \Omega$).



(a)



(b)

Figure 4.23: Power loss calculations: (a) at different stages of circuit in case-1, (b) turn-on loss for all cases in PSG and MGS control.

of minimum input voltage (i.e., cases 1, 2, and 3) using both the control schemes i.e., PSG and MGS. However, in the cases of maximum input voltage (i.e., cases 4, 5, and 6), two switches (S_2 & S_3) lose ZVS with PSG control (Fig. 4.22(a)) while, only one switch (S_4) loses ZVS with MGS control (Fig. 4.11(a)). This is the major advantage of using MGS control.

Power loss breakdown analysis of a 300 W LCL-T RPC is performed and shown in Fig. 4.23. Power loss in HF transformer is assumed as 1% of rated power. Different power losses in the LCL-T converter for the design point i.e., minimum input voltage and full-load (case-1) are presented with pie-chart as shown in Fig. 4.23(a). It is

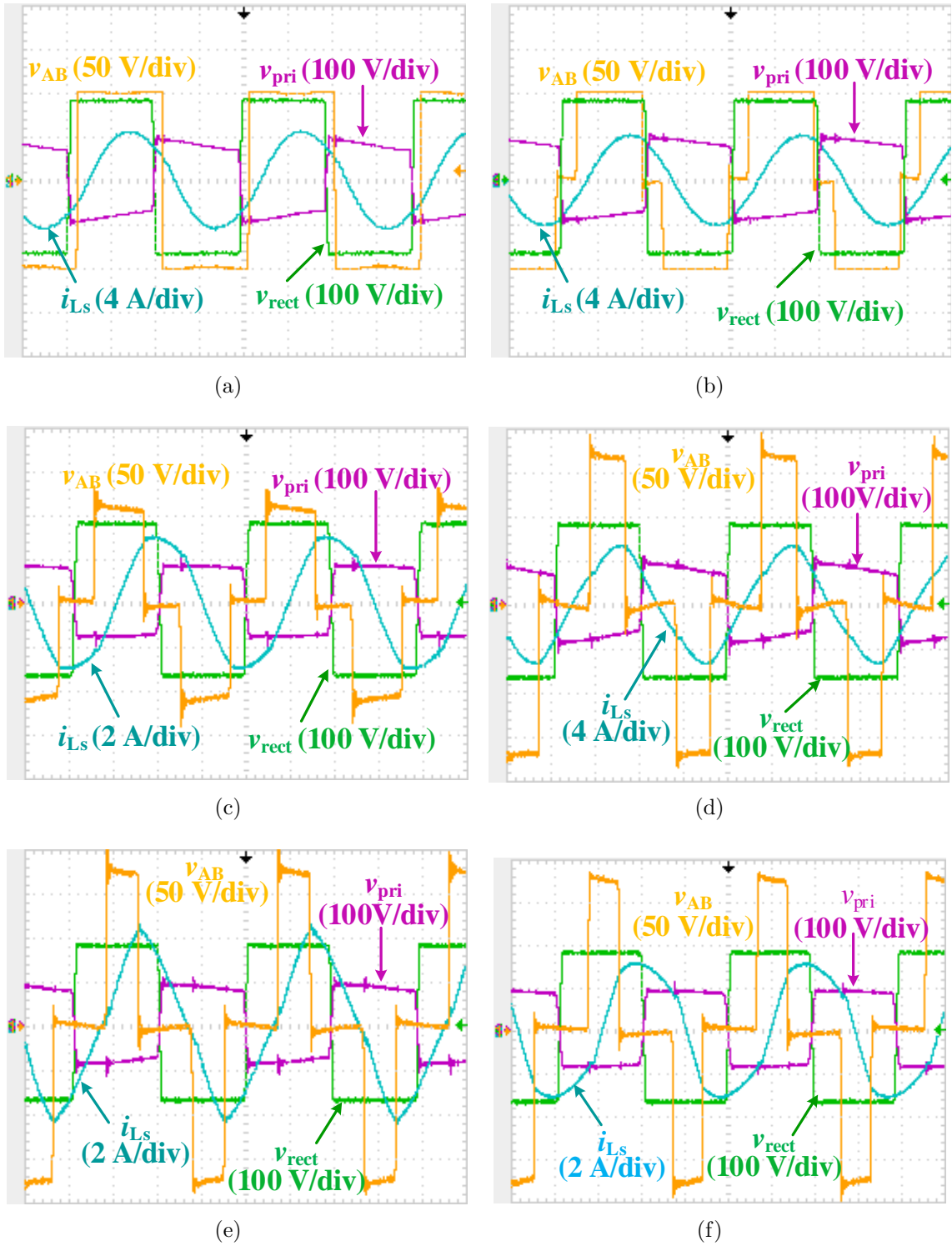


Figure 4.24: Experimental waveforms of v_{AB} , i_{Ls} , v_{pri} , and v_{rect} : (a) case-1, (b) case-2, (c) case-3, (d) case-4, (e) case-5, and (f) case-6.

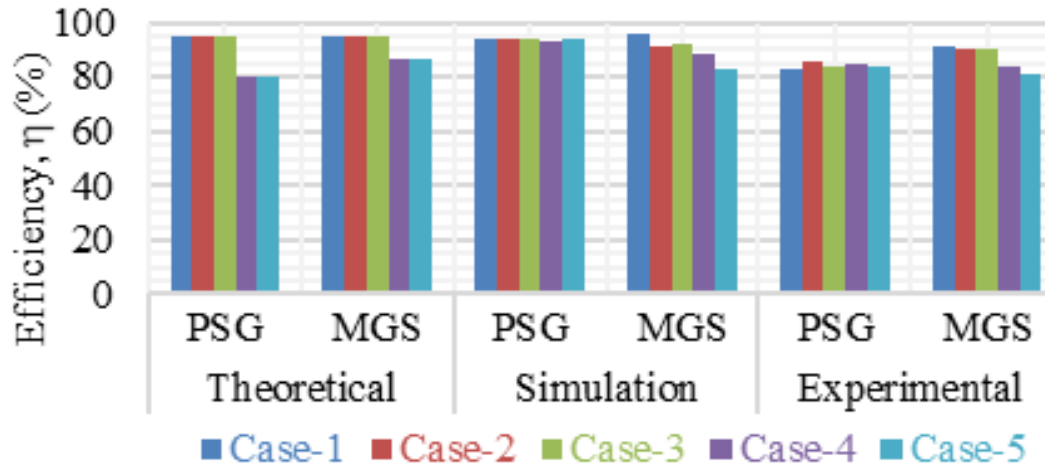


Figure 4.25: Theoretical, simulation, and experimental efficiency comparison plot.

worth nothing here that, with the minimum input voltage the power loss remains the same for the both control schemes as the all four switches turn-on with ZVS. However, with maximum input voltage, the turn-on loss varies with the control scheme as the number of switches that achieve ZVS are different. Two switches (S_2 and S_3) lose ZVS in PSG control whereas, only one switch (S_4) loses ZVS in MGS control. Hence, turn-on loss in MGS control is less compared to PSG control. A bar chart showing turn-on losses for the two control schemes is given in Fig. 4.23(b).

The experimental results of PSG controlled LCL-T resonant converter are shown in Fig. 4.24. Some of the key parameters obtained from the experiment using both PSG and MGS control schemes are presented in Table 4.3 for comparison. It is observed that the change in angle δ to regulate the DC output voltage is small in MGS control compared to PSG control. A bar chart showing the efficiency obtained from calculations, simulations and experiment at different operating conditions is given in Fig. 4.25. It is to be observed that the maximum theoretical, simulation and experimental efficiency of 94.7, 96 and 90.8 respectively for both PSG and MGS control occurs at minimum input voltage and full-load condition (i.e., case-1) itself. However, with maximum input voltage condition (i.e., case 4 and 5), the efficiency obtained is higher with MGS control due to the fact that, only one switch loses ZVS in MGS control as compared to two switches in PSG control. It is experimentally confirmed that both the control schemes can be used to regulate the output voltage. However, MGS is used to get better results e.g., efficiency and narrow variation in pulse-width angle δ .

A qualitative comparison of different converter topologies available in the literature is presented in Table 4.4. Also, a brief comparison of performance of LCL-T converter using Fourier series (FS) and fundamental harmonic approximation (FHA) analysis methods is presented in Table 4.5.

4.7 SUMMARY

Fixed-frequency modified gating signals (MGS) control scheme is proposed to regulate the output voltage of an LCL-T resonant power converter for variations in the input voltage and load. Fourier series approach is used to analyze the converter in steady-state. Power loss breakdown analysis is performed. A 300 W converter is designed and its performance is studied using PSIM simulations and the results have been verified by building the experimental model of the converter in the laboratory. Using MGS control scheme, all inverter switches turn-on with ZVS in the case of minimum input voltage and only one switch loses ZVS with maximum input voltage as compared to two in the conventional gating signals. It is shown that, although both the control schemes can be used to regulate the output voltage, the MGS control gives better results in terms of efficiency and the slight variation in pulse-width angle δ for no additional cost or complexity in generating the gating signals. Auxiliary

Table 4.3: Experimental performance comparison of PSG and MGS control schemes

Parameters	Case-1		Case-2		Case-3	
	<i>PSG</i>	<i>MGS</i>	<i>PSG</i>	<i>MGS</i>	<i>PSG</i>	<i>MGS</i>
V_o (V)	199	199	206	202	189	196
δ ($^\circ$)	172	172	138	143	105	122.5
η (%)	90.8	90.8	89.91	90.44	88.1	90
No. of ZVS switches	4					
Parameters	Case-4		Case-5		Case-6	
	<i>PSG</i>	<i>MGS</i>	<i>PSG</i>	<i>MGS</i>	<i>PSG</i>	<i>MGS</i>
V_o (V)	201	197	204.3	206	196	196
δ ($^\circ$)	80	100.2	72	96.5	87.3	87.3
η (%)	71.46	84.23	73.58	81.17	80.2	80.2
No. of ZVS switches	2	3	2	3	2	3

Table 4.4: Comparison of resonant power converter topologies

Parameter	SRC	PRC	LCC	LCL	LCL-T
Change in pulse-width angle (δ)	Wide	Wide	Narrow	Moderate	Narrow
Component stresses	Lowest	Highest	High	Low	High
Load short-circuit protection	No	Yes	No	No	Yes

Table 4.5: Comparison of FS analysis over FHA analysis

Parameters	FHA			FS		
	<i>Cal.</i>	<i>Sim.</i>	<i>Exp.</i>	<i>Cal.</i>	<i>Sim.</i>	<i>Exp.</i>
V_o (V)	220	213.96	197.4	220	214.62	199
I_{Lsr} (A)	3.33	3.30	2.87	3.04	2.99	3.04
V_{Csr} (V)	452.29	445	432.9	260	253	254
η (%)	94.74	94.14	82.96	94.74	96	90.8
L_s (μ H)	226.74			126.21		
L_t (μ H)	226.74			100.92		

zero-voltage-transition (ZVT) circuit may be used to make the converter fully-ZVS for any operating condition.

Chapter 5

SMALL-SIGNAL MODELING OF LCL-T RESONANT POWER CONVERTER

Contents

5.1	SMALL-SIGNAL MODELING	89
5.1.1	STATE-SPACE ANALYSIS	90
5.1.2	TRANSFER FUNCTIONS	95
5.2	CLOSED LOOP CONTROL	96
5.3	SUMMARY	96

The small-signal model which is useful in understanding the complete behavior of the converter for fluctuations in the input, output and control parameters is derived using extended describing function and presented in this Chapter.

5.1 SMALL-SIGNAL MODELING

Small-signal modeling is required to develop a single loop voltage feedback control scheme for regulating the output voltage of LCL-T resonant converter for variations in the input voltage and the load. The small-signal model is obtained by using extended describing function (EDF) method (Tahavorgar and Quicoe, 2019) and derivations of different transfer functions using Laplace transform are given in this Section.

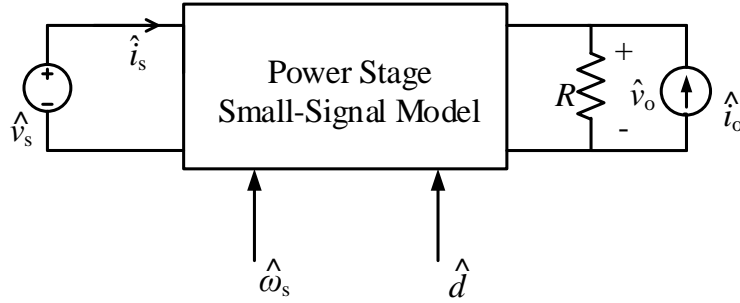


Figure 5.1: Conceptual diagram for small-signal model of resonant converters (Yang et al., 1992).

The conceptual diagram for small-signal model of the resonant converters is shown in Fig. 5.1. \hat{v}_s and \hat{i}_o stand for small-signal variables of the input voltage and output current respectively. $\hat{\omega}_s$ and \hat{d} correspond to frequency control and duty cycle control respectively.

5.1.1 STATE-SPACE ANALYSIS

Extended describing function (EDF) method is used to derive the state-space equations of a LCL-T resonant converter. The step-by-step analysis procedure is given as follows,

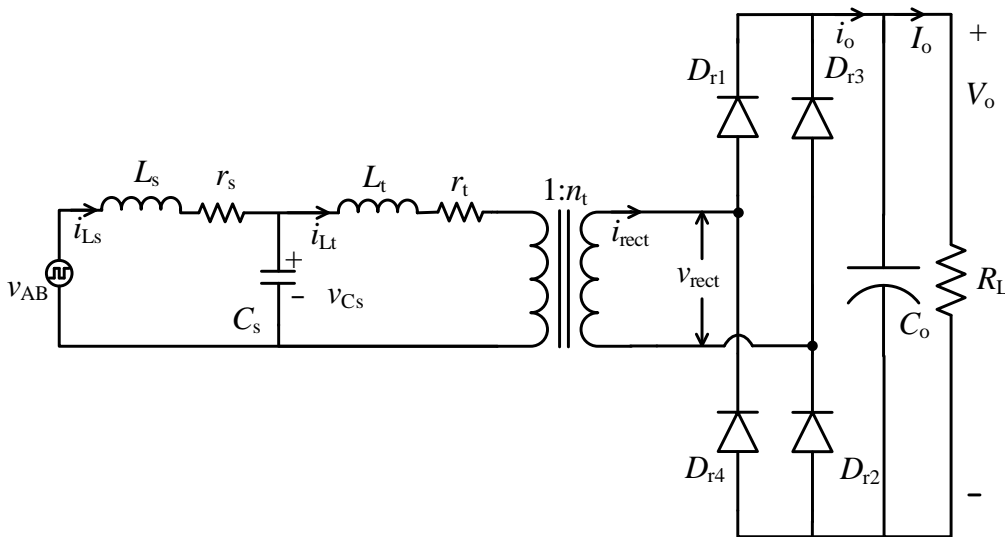


Figure 5.2: Equivalent circuit at the inverter output terminals of LCL-T resonant power converter.

1. For the LCL-T fixed-frequency DC-DC converter circuit given in Fig. 3.1, the equivalent circuit at the inverter output terminals is shown in Fig. 5.2. It is assumed that the switches, diodes and capacitors are ideal. The inductors (L_s , L_t) are considered as lossy and their resistances are represented as r_s and r_t respectively.
2. The possible non-linear state equations of Fig. 5.2 are as follows,

$$v_{AB} = r_s i_{Ls} + L_s \frac{di_{Ls}}{dt} + v_{Cs} \quad (5.1)$$

$$C_s \frac{dv_{Cs}}{dt} = i_{Ls} - |i_{Lt}| \quad (5.2)$$

$$v_{Cs} = r_t i_{Lt} + L_t \frac{di_{Lt}}{dt} + n \cdot \text{sign}(i_{Lt}) v_o \quad (5.3)$$

$$n|i_{Lt}| = \frac{v_o}{R} + C_o \frac{dv_o}{dt} \quad (5.4)$$

where, v_{AB} is a square wave voltage generated by full-bridge inverter, i_{Ls} , v_{Cs} , i_{Lt} , and v_o are state variables. n is the turns ration ($1/n_t$).

3. The state variables of the converter i_{Ls} , v_{Cs} , and i_{Lt} are approximated by fundamental harmonics. The output filter variables are approximated by DC components.

Here,

$$i_{Ls} = i_{Lss}(t) \sin(\omega_s t) + i_{Lsc}(t) \cos(\omega_s t) \quad (5.5)$$

$$v_{Cs} = v_{Css}(t) \sin(\omega_s t) + v_{Csc}(t) \cos(\omega_s t) \quad (5.6)$$

$$i_{Lt} = i_{Lts}(t) \sin(\omega_s t) + i_{Ltc}(t) \cos(\omega_s t) \quad (5.7)$$

The fundamental harmonic terms $\{i_{Lss}, i_{Lsc}, v_{Css}, v_{Csc}, i_{Lts}, i_{Ltc}\}$ are time varying, so the dynamic behavior of these terms can be investigated. The derivatives of these (5.5)-(5.7) are:

$$\frac{di_{Ls}}{dt} = \left(\frac{di_{Lss}}{dt} - \omega_s i_{Lsc} \right) \sin(\omega_s t) + \left(\frac{di_{Lsc}}{dt} + \omega_s i_{Lss} \right) \cos(\omega_s t) \quad (5.8)$$

$$\frac{dv_{Cs}}{dt} = \left(\frac{dv_{Css}}{dt} - \omega_s v_{Csc} \right) \sin(\omega_s t) + \left(\frac{dv_{Csc}}{dt} + \omega_s v_{Css} \right) \cos(\omega_s t) \quad (5.9)$$

$$\frac{di_{Lt}}{dt} = \left(\frac{di_{Lts}}{dt} - \omega_s i_{Ltc} \right) \sin(\omega_s t) + \left(\frac{di_{Ltc}}{dt} + \omega_s i_{Lts} \right) \cos(\omega_s t) \quad (5.10)$$

4. The non-linear terms in (5.1)-(5.4) can be approximated either by the fundamental terms or DC terms.

$$v_{AB} = f_1(V_s, D) \sin(\omega_s t) \quad (5.11)$$

$$\text{sign}(i_{Lt})v_o = f_2(i_{Lts}, i_{Ltc}, v_o) \sin \omega_s t + f_3(i_{Lts}, i_{Ltc}, v_o) \cos(\omega_s t) \quad (5.12)$$

$$|i_{Lt}| = f_4(i_{Lts}, i_{Ltc}) \quad (5.13)$$

where, $f_1(*, *)$ - $f_4(*, *)$ are called extended describing functions (EDFs). They are functions of the operating conditions and the harmonic coefficients of the state variables. The EDF terms can be calculated by using Fourier expansions of non-linear terms. Therefore,

$$f_1(V_s, D) = \frac{4V_s}{\pi} \cdot \sin(\pi D) \quad (5.14)$$

$$f_2(i_{Lts}, i_{Ltc}, v_o) = \frac{4}{\pi} \cdot \frac{i_{Lts}}{i_p} v_o \quad (5.15)$$

$$f_3(i_{Lts}, i_{Ltc}, v_o) = \frac{4}{\pi} \cdot \frac{i_{Ltc}}{i_p} v_o \quad (5.16)$$

$$f_4(i_{Lts}, i_{Ltc}) = \frac{2}{\pi} \cdot i_p \quad (5.17)$$

where,

$$i_p = \sqrt{i_{Lts}^2 + i_{Ltc}^2}$$

i_{Lts} and i_{Ltc} are the sine and cosine components of the inductor current i_{Lt} respectively, and D is the duty cycle which is considered to be 50%.

5. Substitute the (5.5) - (5.17) in (5.1) - (5.4), and then equate the sin, cos and DC terms.

$$L_s \frac{di_{Lss}}{dt} = -r_s i_{Lss} + L_s \omega_s i_{Lsc} - v_{Css} + \frac{4V_s}{\pi} \quad (5.18)$$

$$L_s \frac{di_{Lsc}}{dt} = -r_s i_{Lsc} - L_s \omega_s i_{Lss} - v_{Csc} \quad (5.19)$$

$$C_s \frac{dv_{Css}}{dt} = i_{Lss} - i_{Ls} + \omega_s v_{Csc} \quad (5.20)$$

$$C_s \frac{dv_{Csc}}{dt} = i_{Lsc} - i_{Lc} - \omega_s v_{Css} \quad (5.21)$$

$$L_t \frac{di_{Lts}}{dt} = v_{C_{ss}} - \frac{4}{\pi} \cdot \frac{i_{Lts}}{i_p} v_o + L_t \omega_s i_{Ltc} - r_t i_{Ls} \quad (5.22)$$

$$L_t \frac{di_{Ltc}}{dt} = v_{C_{sc}} - \frac{4}{\pi} \cdot \frac{i_{Ltc}}{i_p} v_o - L_t \omega_s i_{Lts} - r_t i_{Ltc} \quad (5.23)$$

$$C_o \frac{dv_o}{dt} = n \frac{2}{\pi} \cdot i_p - \frac{v_o}{R} \quad (5.24)$$

6. The small-signal equivalent circuit diagram of the resonant converters is shown in Fig. 5.1. All the variables in (5.18)-(5.24) are replaced with the AC small-signal part of the corresponding variables. i.e.,

$$v_s = V_s + \hat{v}_s \quad D = D + \hat{d}$$

$$i_o = I_o + \hat{i}_o \quad v_o = V_o + \hat{v}_o \quad \omega_s = \omega_s + \hat{\omega}_s$$

where, \hat{v}_s , \hat{d} , $\hat{\omega}_s$, \hat{i}_o and \hat{v}_o are the small-signal parts of corresponding variables.

$$L_s \frac{d\hat{i}_{Lss}}{dt} = -r_s \hat{i}_{Lss} + L_s (\omega_s + \hat{\omega}_s) \hat{i}_{Lsc} - v_{C_{ss}} + \frac{4}{\pi} \cdot (V_s + \hat{v}_s) \cdot \sin(\pi(D + \hat{d})) \quad (5.25)$$

$$L_s \frac{d\hat{i}_{Lsc}}{dt} = -r_s \hat{i}_{Lsc} - L_s (\omega_s + \hat{\omega}_s) \hat{i}_{Lss} - v_{C_{sc}} \quad (5.26)$$

$$C_s \frac{d\hat{v}_{C_{ss}}}{dt} = \hat{i}_{Lss} - \hat{i}_{Lts} + C_s (\omega_s + \hat{\omega}_s) \hat{v}_{C_{sc}} \quad (5.27)$$

$$C_s \frac{d\hat{v}_{C_{sc}}}{dt} = \hat{i}_{Lsc} - \hat{i}_{Ltc} - C_s (\omega_s + \hat{\omega}_s) \hat{v}_{C_{ss}} \quad (5.28)$$

$$L_t \frac{d\hat{i}_{Lts}}{dt} = \hat{v}_{C_{ss}} - r_t \hat{i}_{Lts} + L_t (\omega_s + \hat{\omega}_s) \hat{i}_{Lc} - \frac{4}{\pi} \cdot \frac{\hat{i}_{Lts}}{\hat{i}_p} \hat{v}_o \quad (5.29)$$

$$L_t \frac{d\hat{i}_{Ltc}}{dt} = \hat{v}_{C_{sc}} - r_t \hat{i}_{Ltc} - L_t (\omega_s + \hat{\omega}_s) \hat{i}_{Ls} - \frac{4}{\pi} \cdot \frac{\hat{i}_{Ltc}}{\hat{i}_p} \hat{v}_o \quad (5.30)$$

$$C_o \frac{d\hat{v}_o}{dt} = n \frac{2}{\pi} \cdot \hat{i}_p - \frac{\hat{v}_o}{R} + \hat{i}_o \quad (5.31)$$

7. The general form of state-space analysis of the converter is as follows,

$$\frac{d\hat{x}}{dt} = A\hat{x} + B\hat{u} \quad (5.32)$$

$$\hat{y} = C\hat{x} \quad (5.33)$$

where,

$$\begin{aligned}\hat{x} &= (\hat{i}_{Lss}, \hat{i}_{Lsc}, \hat{v}_{Css}, \hat{v}_{Csc}, \hat{i}_{Lts}, \hat{i}_{Ltc}, \hat{v}_o)^T \\ \hat{u} &= (\hat{v}_s, \hat{d}, \hat{\omega}_s, \hat{i}_o)^T \\ \hat{y} &= (\hat{v}_o)\end{aligned}$$

The resulting state-space matrices (A, B, C) using (5.25) - (5.33) are as,

$$A = \begin{pmatrix} \frac{-r_s}{L_s} & F\omega_r & \frac{-1}{L_s} & 0 & 0 & 0 & 0 \\ -F\omega_r & \frac{-r_s}{L_s} & 0 & \frac{-1}{L_s} & 0 & 0 & 0 \\ \frac{1}{C_s} & 0 & 0 & F\omega_r & \frac{-1}{C_s} & 0 & 0 \\ 0 & \frac{1}{C_s} & -F\omega_r & 0 & 0 & \frac{-1}{C_s} & 0 \\ 0 & 0 & \frac{1}{L_t} & 0 & \frac{-r_t}{L_t} & F\omega_r & \frac{K_s}{L_t} \\ 0 & 0 & 0 & \frac{1}{L_t} & -F\omega_r & \frac{-r_t}{L_t} & \frac{K_c}{L_t} \\ 0 & 0 & 0 & 0 & \frac{nI_p}{\pi I_{Lts}} & \frac{nI_p}{\pi I_{Ltc}} & \frac{-1}{RC_o} \end{pmatrix}$$

$$B = \begin{pmatrix} \frac{4}{\pi L_s} \cdot \sin(\pi D) & \frac{4V_s}{\pi L_s} \cdot \cos(\pi D) & I_{Lsc} & 0 \\ 0 & 0 & -I_{Lss} & 0 \\ 0 & 0 & V_{Lcc} & 0 \\ 0 & 0 & -V_{Lcs} & 0 \\ 0 & 0 & I_{Ltc} & 0 \\ 0 & 0 & -I_{Lts} & 0 \\ 0 & 0 & 0 & \frac{1}{C_o} \end{pmatrix}$$

$$C = (0 \ 0 \ 0 \ 0 \ 0 \ 0 \ 0 \ 1)$$

where, $K_s = \frac{2}{\pi} \cdot \frac{i_{Lts}}{i_p}$ and $K_c = \frac{2}{\pi} \cdot \frac{i_{Ltc}}{i_p}$

5.1.2 TRANSFER FUNCTIONS

Transfer functions relating the output voltage to various converter control variables can be obtained by transforming the state-space equations to the frequency domain using the inverse Laplace transform as follows:

$$T(s) = C(sI - A)^{-1}B \quad (5.34)$$

The four transfer functions namely, input voltage to output voltage (\hat{v}_o/\hat{v}_s), duty ratio to output voltage (\hat{v}_o/\hat{d}), switching frequency to output voltage ($\hat{v}_o/\hat{\omega}_s$), output current to output voltage (\hat{v}_o/\hat{i}_o) can be derived by solving (5.34).

The output voltage of LCL-T converter can be regulated with two degrees of freedom namely, switching frequency (ω_s) and duty ratio (d). Therefore, either switching frequency to output voltage ($\hat{v}_o/\hat{\omega}_s$) or duty ratio to output voltage (\hat{v}_o/\hat{d}) transfer function can be used to regulate the output voltage. In these, implementation of closed loop control or compensator is more straight forward and easy using variable duty cycle control than variable frequency control. Therefore, duty ratio to output voltage transfer function (\hat{v}_o/\hat{d}) is more suitable to demonstrate the stability and transient behavior of the converter and also design a single loop voltage feedback control to regulate the output voltage.

$$\frac{\hat{v}_o(s)}{\hat{d}(s)} = \frac{K_d}{\Delta} \left(s^3 - 3F\omega_r s^2 + (\omega_r^2(1+K) - 3F^2\omega_r^2) s + F^3\omega_r^3 - F\omega_r^3(1+K) \right) \quad (5.35)$$

where,

$$\Delta = \left(s + \frac{1}{RC_o} \right) \left(s^6 + \omega_r^2(3F^2 + 2(K+1))s^4 + 3\omega_r^4(F^4 + (K+1)^2)s^2 + \omega_r^6 F^2(F^2 - K)(F^2 - (K+2)) \right) \quad (5.36)$$

$$K_d = \frac{4n^2 I_P V_s \omega_r^2}{\pi I_L L_s L} \cos(\pi D)$$

$$\omega_r = \frac{1}{\sqrt{L_s C_s}}$$

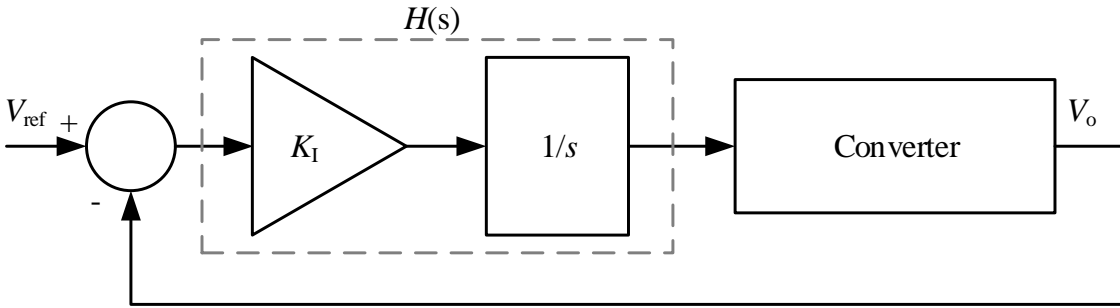


Figure 5.3: Voltage feedback control scheme to control the output voltage of the converter.

5.2 CLOSED LOOP CONTROL

In order to use duty ratio to output voltage transfer function in a closed loop control scheme, the transfer function needs to be simplified by removing the non-significant poles and zeros. The imaginary poles associated with resonant frequency are non-significant poles since these occur at very high frequencies compared to the real poles. Real zeros are assumed to occur at infinity since these are associated with higher frequencies in comparison with the significant poles. Fig. 5.3 shows the voltage feedback loop with an integral compensator which is used to control the output voltage of the converter with respect to the reference voltage.

5.3 SUMMARY

The small-signal modeling of the LCL-T resonant converter is carried out using extended describing function (EDF) method. It combines both the time and frequency domain analyses. The duty ratio to output voltage transfer function is derived to demonstrate the stability and transient behavior of the converter.

Chapter 6

CONCLUSIONS AND FUTURE SCOPE

In this work, for the effective control of LCL-T resonant converter, two different control schemes are proposed. Also, two different analysis methods are used and the performance of the converter is studied. The important contributions are listed below.

6.1 CONTRIBUTIONS

1. Proposed a fixed-frequency phase-shifted gating (PSG) control scheme for regulating the output voltage of the LCL-T resonant power converter against the input voltage and load variations.
 - The operating principle of PSG control scheme is explained using typical operating waveforms
 - The possible operating modes with PSG control are shown and each mode of operation is explained with the help of equivalent circuits
 - The steady-state analysis of the converter is carried out using fundamental harmonic approximation (FHA) method
 - A 300 W LCL-T converter operated with PSG control has been designed and different design curves are drawn based on the derived FHA analysis for selecting the near optimum design parameters
 - The ZVS condition for all the switches with PSG control is derived

- Performance of the converter is studied using PSIM simulations
 - The power loss breakdown analysis is performed
 - The experimental setup of a LCL-T resonant converter is built in the laboratory and tested
 - The gating signals of 3.75 V are generated using Nexys DDR4 artex-7 FPGA board. Driver circuit is developed to scale up the voltage to 15 V so as to drive the MOSFETs.
 - Compared the calculated, simulation, and experimental results
2. Proposed a fixed-frequency modified gating signals (MGS) control scheme for regulating the output voltage of the LCL-T resonant power converter against the input voltage and load variations.
- The operating principle of MGS control scheme is explained using typical operating waveforms
 - The possible operating modes with MGS control are shown and each mode of operation is explained with the help of equivalent circuits
 - The steady-state analysis of the converter is carried out using Fourier series (FS) method
 - A 300 W LCL-T converter operated with MGS control has been designed and different design curves are drawn based on the derived FS analysis for selecting the near optimum design parameters
 - The ZVS condition for all the switches with MGS control is derived
 - Performance of the designed converter is studied using PSIM simulations
 - The power loss breakdown analysis is performed
 - The experimental setup of a LCL-T resonant converter is built with the newly designed values in the laboratory and tested
 - The gating signals of 3.75 V are generated using Nexys DDR4 artex-7 FPGA board. Driver circuit is developed to scale up the voltage to 15 V so as to drive the MOSFETs.
 - Compared the calculated, simulation, and experimental results

3. Analyzed the PSG controlled LCL-T converter with Fourier series (FS) approach and its performance is studied.
 - The comparison of performance of LCL-T resonant converter with PSG and MGS control schemes is made
4. The small-signal modeling of LCL-T resonant converter is carried out using extended describing function (EDF) method. This can be used for future work to study the dynamic behavior of the converter.

6.2 CONCLUSIONS

In this thesis, several conclusions have been made. Some of the important conclusions of the thesis are summarized as following,

- The fixed-frequency phase-shifted gating (PSG) and modified gating signals (MGS) schemes can be used to control the LCL-T resonant converter with no additional series DC blocking capacitor as required in asymmetrical duty cycle (ADC) control scheme.
- In the LCL-T resonant converter, when operated with phase-shifted gating (PSG) control scheme, it is observed that all the inverter switches turn-on with ZVS from full-load to 10% of full-load at the minimum input voltage and two switches lose ZVS at the maximum input voltage.
- In the LCL-T resonant converter, when operated with modified gating signals (MGS) control scheme, it is observed that all the inverter switches turn-on with ZVS from full-load to 10% of full-load in the case of minimum input voltage and only one switch loses ZVS with maximum input voltage as compared to two in the PSG control scheme.
- It is found that, to regulate the output voltage for input voltage and load variations, MGS control scheme requires a small change in pulse-width angle (δ) than the PSG control scheme.
- Turn-on loss with MGS control scheme is less compared to PSG control scheme at maximum input voltage. Hence, efficiency is more with the MGS control.

- Fourier series (FS) steady-state analysis method considers n- harmonic components in the analysis. Hence it gives better and more accurate results compared to fundamental harmonic approximation (FHA) method where, only fundamental component is considered.

6.3 FUTURE SCOPE

Based on the research carried out in this thesis, the recommendations for future research are given below.

1. Zero-voltage transition (ZVT) circuit can be used to make the inverter switches to have ZVS even with the maximum input voltage.
2. The transient behavior of the converter can be studied to understand the small-signal stability of the converter.

Appendix A

Fourier Analysis

A periodic waveform is one which repeats itself after regular intervals of the time. If $f(t)$ waveform is said to be periodic, then

$$f(t) = f(t + T) \quad (\text{A.1})$$

where, T is the total time period of one cycle of $f(t)$.

The periodic equation of any waveform for an angular frequency ω_s is,

$$f(t) = a_o + \sum_{n=1,2,3\dots}^{\infty} [a_n \cos(n\omega_s t) + b_n \sin(n\omega_s t)] \quad (\text{A.2})$$

where,

a_o is the average value, or dc value of $f(t)$ for one cycle.

$$a_o = \frac{1}{T} \int_0^T f(t) dt = \frac{1}{2\pi} \int_0^{2\pi} f(\omega_s t) d(\omega_s t)$$

a_n is the amplitude of 'cos' component of $f(t)$

$$a_n = \frac{2}{T} \int_0^T f(t) \cos(n\omega_s t) dt = \frac{1}{\pi} \int_0^{2\pi} f(\omega_s t) \cos(n\omega_s t) d(\omega_s t)$$

b_n is the amplitude of 'sin' component of $f(t)$

$$b_n = \frac{2}{T} \int_0^T f(t) \sin(n\omega_s t) dt = \frac{1}{\pi} \int_0^{2\pi} f(\omega_s t) \sin(n\omega_s t) d(\omega_s t)$$

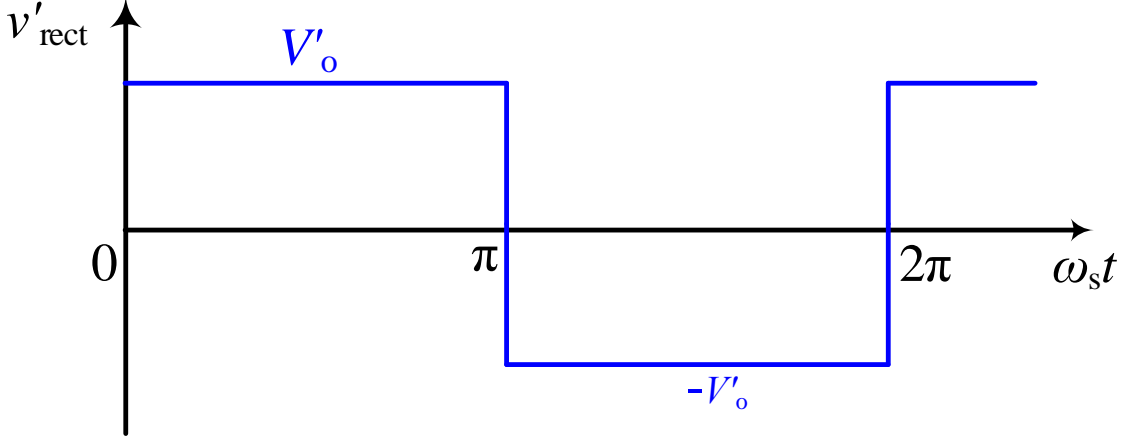


Figure A.1: Rectifier input voltage waveform

(i). Rectifier Input Voltage Waveform

The rectifier input voltage waveform of the LCL-T resonant power converter (Fig. 3.1) is shown in Fig. A.1. Since it is a periodic waveform the resultant voltage equation is as follows:

$$v'_{rect}(t) = a_o + \sum_{n=1}^{\infty} [a_n \cos(n\omega_o t) + b_n \sin(n\omega_o t)] \quad (\text{A.3})$$

Therefore, using (A.2) and Fig. A.1,

(i) $a_o = 0$

(ii) $a_n = 0$

(iii) $b_n = \frac{2V'_o}{n\pi} [1 - \cos(n\pi)]$

a. $b_n = 0$ for $n = 2, 4, \dots$ i.e., even

b. $b_n = \frac{4V'_o}{n\pi}$ for $n = 1, 3, \dots$ i.e., odd

Therefore,

$$v'_{rect}(t) = \sum_{n=1,3,5..}^{\infty} \frac{4V'_o}{n\pi} \sin(n\omega_o t) \quad (\text{A.4})$$

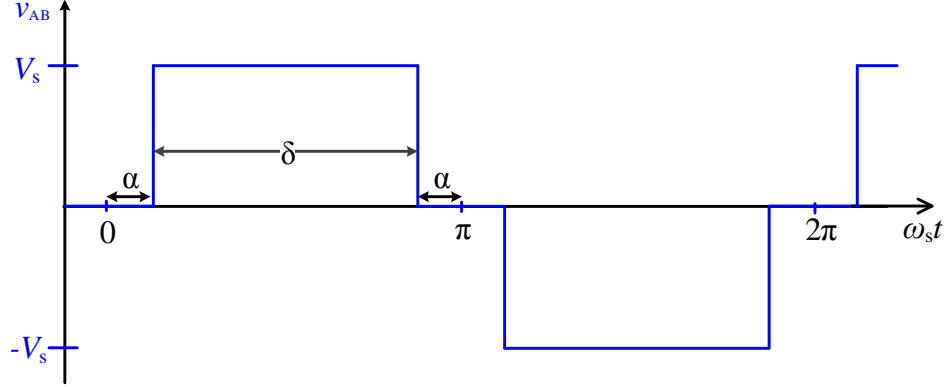


Figure A.2: Inverter output voltage waveform with phase-shifted gating control scheme

(ii). Phase-shifted Gating (PSG) Control

The inverter output voltage waveform (v_{AB}) of phase-shifted gating (PSG) control scheme is shown in Fig. A.2. Since the v_{AB} waveform is periodic, then the voltage equation is as follows

$$v_{AB}(t) = a_o + \sum_{n=1}^{\infty} [a_n \cos(n\omega_o t) + b_n \sin(n\omega_o t)] \quad (\text{A.5})$$

Therefore, using (A.2) and Fig. A.2,

(i) $a_o = 0$

(ii) $a_n = 0$

(iii) $b_n = \frac{V_s}{n\pi} [2\cos(n\alpha) - 2(-1)^n \cos(n\alpha)]$

a. $b_n = 0$ for $n = 2, 4, \dots$ i.e., even

b. $b_n = \frac{4V_s}{n\pi} \cos(n\alpha)$ for $n = 1, 3, \dots$ i.e., odd

Therefore,

$$v_{AB}(t) = \sum_{n=1,3,5..} \frac{4V_s}{n\pi} \cos(n\alpha) \sin(n\omega_s t) \quad (\text{A.6})$$

where, $\alpha = \frac{\pi - \delta}{2}$

$$v_{AB}(t) = \sum_{n=1,3,5..} \frac{4V_s}{n\pi} \sin\left(\frac{n\pi}{2}\right) \sin\left(\frac{n\delta}{2}\right) \sin(n\omega_s t) \quad (\text{A.7})$$

(iii). Modified Gating Signal (MGS) Control

Similarly, the inverter output voltage waveform (V_{AB}) obtained from modified gating signals (MGS) control scheme is periodic and shown in Fig. A.3.

Therefore, using (A.2) and Fig. A.3,

(i) $a_o = 0$

(ii) $a_n = 0$

(iii) $b_n = \frac{2V_s}{n\pi} [1 - \cos(n\pi) \cdot \cos(n\alpha)]$

Therefore,

$$v_{AB}(t) = \sum_{n=1,3,5..} \frac{4V_s}{n\pi} [1 + \cos(n\alpha)] \sin(n\omega_s t) \quad (\text{A.8})$$

where, $\alpha = \pi - \delta$

$$v_{AB}(t) = \sum_{n=1,3,5..} \frac{2V_s}{n\pi} [1 - \cos(n\delta)] \sin(n\omega_s t) \quad (\text{A.9})$$

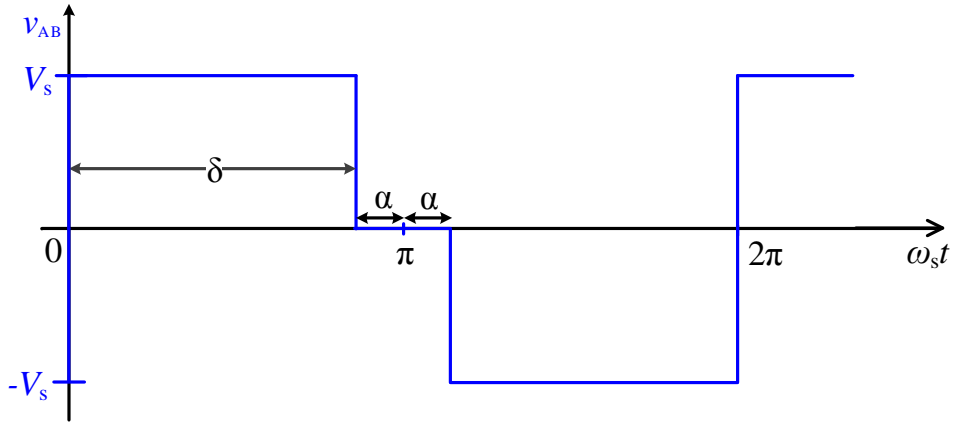


Figure A.3: Inverter output voltage waveform with modified gating signals control scheme

Appendix B

Power Loss Calculations

The power loss in the LCL-T resonant converter takes place mainly in three parts i.e., power loss in the full-bridge inverter, high-frequency transformer, and output diode rectifier. The calculation of losses in these parts is explained below:

(a). Losses in the full-bridge inverter

Losses in the full-bridge inverter are divided into switching losses and conduction losses in the MOSFETs, and conduction losses in the body-diodes of the MOSFETs.

(i). Switching losses:

Switching losses in the full-bridge inverter are sub-divided into turn-on losses and turn-off losses. The typical voltage and current waveforms of a MOSFET at turn-on and turn-off instants are shown in Fig. B.1.

- **Turn-on losses:** Turn-on losses occur if the voltage across the switch and current through the switch exist simultaneously at turn-on. The total turn-on loss can be computed using (B.1),

$$P_{on} = \left[\frac{1}{2} \cdot V_s \cdot I_s \cdot (t_d + t_r) + V_s \cdot Q_{rr} \right] \cdot f_s \cdot n \quad (\text{B.1})$$

Where, V_s is the input voltage, I_s is the effective value of switch current during turn-on, t_d is the delay time, t_r is the rise time, Q_{rr} is the reverse recovery charge, f_s is the switching frequency, and n is the number of switches.

- **Turn-off loss:** The turn-off losses occur if the voltage across switch and current through the switch exist simultaneously during turn-off. The total turn-off loss can be computed using (B.2),

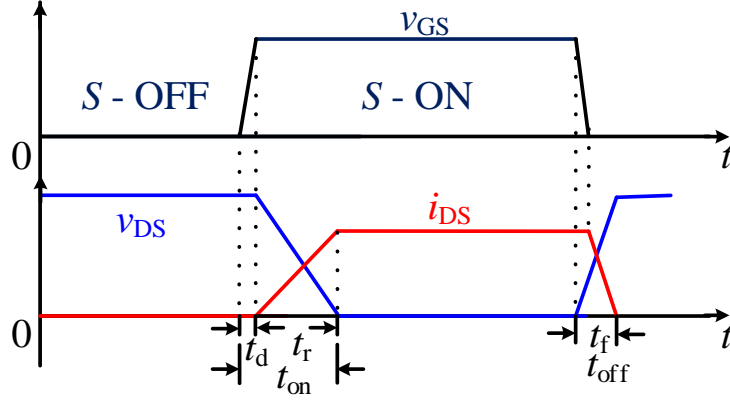


Figure B.1: Typical voltage and current waveforms of a MOSFET during turn-on and turn-off process (v_{DS} : Drain to source voltage, i_{DS} : Drain current, v_{GS} : Gating signal, t_{on} : turn-on time, t_{off} : turn-off time, t_d : delay time, t_r : rise time of the MOSFET).

$$P_{off} = \frac{1}{12} \cdot V_s \cdot i_o \cdot t_f \cdot f_s \cdot n \quad (\text{B.2})$$

Where, V_s is the input voltage, i_o is the switch current at the beginning of turn-off, t_f is the fall time of the switch, f_s is the switching frequency, and n is the number of switches.

(ii).Conduction losses:

The conduction loss in a switch occurs during its conduction due to the finite voltage drop across it. Conduction loss in a MOSFET is a function of its drain-to-source resistance ($R_{DS(on)}$). The total conduction loss can be evaluated using (B.3),

$$P_{conduction} = I_{sw(rms)}^2 \cdot R_{DS(on)} \cdot n \quad (\text{B.3})$$

Where, $I_{sw(rms)}$ is the rms switch current and it can be computed using (B.4),

$$I_{sw(rms)} = \frac{i_{m(sw)}}{2\sqrt{\pi}} [\pi - \phi + \frac{1}{2} \sin(2\phi)]^{(1/2)} \quad (\text{B.4})$$

where, $I_{m(sw)}$ is the peak value and ϕ is the phase angle of the switch current.

(iii). Diode losses:

The power loss in the body diode of a MOSFET is a function of average diode current and the forward voltage drop of the diode. It can be expressed as,

$$P_d = V_{fd} \cdot I_{d(avg)} \cdot n \quad (\text{B.5})$$

Where, V_{fd} is the forward voltage drop of diode, $I_{d(avg)}$ is the average value of the diode current and it can be computed using (B.6),

$$I_{d(avg)} = \frac{I_{m(sw)}}{2\pi} [1 - \cos(\phi)] \quad (\text{B.6})$$

where, $I_{m(sw)}$ is the peak value and ϕ is the phase angle of the switch current.

(b). HF Transformer Losses:

The loss in the high-frequency transformer consists of copper loss in the winding and iron loss in the core. In the analysis carried here, as found in the literature, the total power loss in the transformer ($P_{transformer}$) is taken as 1 percent of the output power.

(c). Diode Rectifier Losses:

The conduction loss in the diodes of the output rectifier depends on the average current and the forward voltage drop of the diodes. The total conduction loss in the diode rectifier (P_{rect}) can be calculated using (B.7),

$$P_{rect} = V_{FD} \cdot I_{D(avg)} \cdot n \quad (\text{B.7})$$

Where, V_{FD} is the forward voltage, $I_{D(avg)}$ is the average current of the diode. $I_{D(avg)}$ can be computed using (B.8),

$$I_{D(avg)} = \frac{I_o}{2} \quad (\text{B.8})$$

Where, I_o is the output current. Therefore, the total power loss in the resonant converter is,

$$P_L = P_{on} + P_{off} + P_d + P_{conduction} + P_{transformer} + P_{rect} \quad (\text{B.9})$$

Bibliography

- Abbasi, M., Emamalipour, R., Masood Cheema, M. A., and Lam, J. (2019). An extended describing function model for a hybrid frequency/phase-shift controlled sic-based high-gain dc-dc resonant converter module. In *2019 IEEE Energy Conversion Congress and Exposition (ECCE)*, pages 695–701.
- Abdelsalam, A. K., Massoud, A. M., Ahmed, S., and Enjeti, P. N. (2011). High-performance adaptive perturb and observe mppt technique for photovoltaic-based microgrids. *IEEE Transactions on power electronics*, 26(4):1010–1021.
- Agarwal, V. and Bhat, A. K. S. (1995). Small signal analysis of the lcc-type parallel resonant converter using discrete time domain modeling. *IEEE Transactions on Industrial Electronics*, 42(6):604–614.
- Agarwal, V., Bhat, A. K. S., and Belaguli, M. (1997). Dynamic analysis of lcc-type parallel resonant converter operating in discontinuous current mode. *Canadian Journal of Electrical and Computer Engineering*, 22(3):119–129.
- Ahmed, M. T., Gonçalves, T., Albino, A., Rashel, M. R., Veiga, A., and Tlemcani, M. (2016). Different parameters variation analysis of a pv cell. In *2016 International Conference for Students on Applied Engineering (ICSAE)*, pages 176–180.
- Amjad, M. and Salam, Z. (2014). Design and implementation of a high-frequency lc-based half-bridge resonant converter for dielectric barrier discharge ozone generator. *IET Power Electronics*, 7(9):2403–2411.
- Asa, E., Colak, K., Bojarski, M., and Czarkowski, D. (2015). Asymmetrical duty-cycle and phase-shift control of a novel multiport cll resonant converter. *IEEE Journal of Emerging and Selected Topics in Power Electronics*, 3(4):1122–1131.

- Ayachit, A., Murthy-Bellur, D., and Kazimierczuk, M. K. (2012). Steady-state analysis of series resonant converter using extended describing function method. In *2012 IEEE 55th International Midwest Symposium on Circuits and Systems (MWSCAS)*, pages 1160–1163.
- Bhat, A. (1990). Analysis and design of lcl-type series resonant converter. In *12th International Conference on Telecommunications Energy*, pages 172–178.
- Bhat, A. (1991a). Analysis and design of a modified series resonant converter. In *[Proceedings] APEC '91: Sixth Annual Applied Power Electronics Conference and Exhibition*, pages 594–600.
- Bhat, A. and Dewan, S. (1989). A generalized approach for the steady-state analysis of resonant inverters. *IEEE Transactions on Industry Applications*, 25(2):326–338.
- Bhat, A. K. S. (1991b). Analysis and design of a series-parallel resonant converter with capacitive output filter. *IEEE Transactions on Industry Applications*, 27(3):523–530.
- Bhat, A. K. S. (1991). A unified approach for the steady-state analysis of resonant converters. *IEEE Transactions on Industrial Electronics*, 38(4):251–259.
- Bhat, A. K. S. (1992). Fixed-frequency pwm series-parallel resonant converter. *IEEE Transactions on Industry Applications*, 28(5):1002–1009.
- Bhat, A. K. S. (1995a). A fixed frequency lcl-type series resonant converter. *IEEE Transactions on Aerospace and Electronic Systems*, 31(1):125–137.
- Bhat, A. K. S. (1995b). A generalized steady-state analysis of resonant converters using two-port model and fourier-series approach. In *Proceedings of 1995 IEEE Applied Power Electronics Conference and Exposition - APEC'95*, volume 2, pages 920–926 vol.2.
- Bhat, A. K. S. and Dewan, S. B. (1987). Analysis and design of a high-frequency resonant converter using lcc-type commutation. *IEEE Transactions on Power Electronics*, PE-2(4):291–301.
- Bhat, A. K. S. and Zheng, R. L. (1996). A three-phase series-parallel resonant converter-analysis, design, simulation, and experimental results. *IEEE Transactions on Industry Applications*, 32(4):951–960.

- Bhowmick, S. and Bhat, A. K. S. (2014). A fixed-frequency lcc-type resonant converter with inductive output filter using a modified gating scheme. In *2014 International Conference on Advances in Energy Conversion Technologies (ICAECT)*, pages 140–145.
- Bo-Tao Lin, Kam-Wah Siu, and Yim-Shu Lee (1999). Actively clamped zero-current-switching quasi-resonant converters using igbts. *IEEE Transactions on Industrial Electronics*, 46(1):75–81.
- Borage, M. B., Nagesh, K. V., Bhatia, M. S., and Tiwari, S. (2009). Characteristics and design of an asymmetrical duty-cycle-controlled lcl-t resonant converter. *IEEE Transactions on Power Electronics*, 24(10):2268–2275.
- Buccella, C., Cecati, C., Latafat, H., Pepe, P., and Razi, K. (2015). Observer-based control of llc dc/dc resonant converter using extended describing functions. *IEEE Transactions on Power Electronics*, 30(10):5881–5891.
- Canales, F., Barbosa, P., and Lee, F. C. (2002). A zero-voltage and zero-current switching three-level dc/dc converter. *IEEE Transactions on Power Electronics*, 17(6):898–904.
- Chakraborty, C., Ishida, M., and Hori, T. (1999). Performance and design of an lcl converter for voltage regulator type applications. *IEEJ Transactions on Industry Applications*, 119(6):848–856.
- Chen, H. and Bhat, A. K. S. (2016). A bidirectional dual-bridge lcl-type series resonant converter controlled with modified gating scheme. In *2016 IEEE 8th International Power Electronics and Motion Control Conference (IPEMC-ECCE Asia)*, pages 3036–3042.
- Chien-Ming Wang (2005). A new family of zero-current-switching (zcs) pwm converters. *IEEE Transactions on Industrial Electronics*, 52(4):1117–1125.
- Davoudi, A. and Jatskevich, J. (2007). Parasitics realization in state-space average-value modeling of pwm dc–dc converters using an equal area method. *IEEE Transactions on Circuits and Systems I: Regular Papers*, 54(9):1960–1967.

- Du, Y. and Bhat, A. K. S. (2014). Analysis and design of a high-frequency isolated dual-tank *lcl* resonant ac-dc converter. In *2014 International Power Electronics Conference (IPEC-Hiroshima 2014 - ECCE ASIA)*, pages 1721–1727.
- Du, Y. and Bhat, A. K. S. (2016). Analysis and design of a high-frequency isolated dual-tank *lcl* resonant ac-dc converter. *IEEE Transactions on Industry Applications*, 52(2):1566–1576.
- Elbuluk, M. E., Verghese, G. C., and Kassakian, J. G. (1988). Sampled-data modeling and digital control of resonant converters. *IEEE Transactions on Power Electronics*, 3(3):344–354.
- Fei, C., Lee, F. C., and Li, Q. (2017). Digital implementation of soft start-up and short-circuit protection for high-frequency *llc* converters with optimal trajectory control (otc). *IEEE Transactions on Power Electronics*, 32(10):8008–8017.
- Feng, W. and Lee, F. C. (2014). Optimal trajectory control of *llc* resonant converters for soft start-up. *IEEE Transactions on Power Electronics*, 29(3):1461–1468.
- Fu, D., Lee, F. C., Liu, Y., and Xu, M. (2008). Novel multi-element resonant converters for front-end dc/dc converters. In *2008 IEEE Power Electronics Specialists Conference*, pages 250–256.
- Gao, X., Wu, H., and Xing, Y. (2017). A multioutput *llc* resonant converter with semi-active rectifiers. *IEEE Journal of Emerging and Selected Topics in Power Electronics*, 5(4):1819–1827.
- Gautam, D. S. and Bhat, A. K. S. (2013). A comparison of soft-switched dc-to-dc converters for electrolyzer application. *IEEE Transactions on Power Electronics*, 28(1):54–63.
- Green, A. W. (1993). Modelling a push-pull parallel resonant convertor using generalised state-space averaging. *IEE Proceedings B - Electric Power Applications*, 140(6):350–356.
- Grigorova, T. G. and Vuchev, A. S. (2018). Dc characteristics of a series resonant dc/dc converter at variable-frequency control methods. In *2018 IEEE XXVII International Scientific Conference Electronics - ET*, pages 1–4.

- Hamada, S. and Nakaoka, M. (2002). A novel zero-voltage and zero-current switching pwm dc-dc converter with reduced conduction losses. *IEEE Transactions on Power Electronics*, 17(3):413–419.
- Hamdad, F.-S. and Bhat, A. (2001). A novel pulsewidth control scheme for fixed-frequency zero-voltage-switching dc-to-dc pwm bridge converter. *IEEE Transactions on Industrial Electronics*, 48(1):101–110.
- Harischandrappa, N. and Bhat, A. K. S. (2014). A fixed-frequency *lcl*-type series resonant converter with a capacitive output filter using a modified gating scheme. *IEEE Transactions on Industry Applications*, 50(6):4056–4064.
- Husev, O., Liivik, L., Blaabjerg, F., Chub, A., Vinnikov, D., and Roasto, I. (2015). Galvanically isolated quasi-z-source dc-dc converter with a novel zvs and zcs technique. *IEEE Transactions on Industrial Electronics*, 62(12):7547–7556.
- Hyeonah Park and Hyosung Kim (2013). Pv cell modeling on single-diode equivalent circuit. In *IECON 2013 - 39th Annual Conference of the IEEE Industrial Electronics Society*, pages 1845–1849.
- j. King, R. and Stuart, T. A. (1982). Modeling the full-bridge series-resonant power converter. *IEEE Transactions on Aerospace and Electronic Systems*, AES-18(4):449–459.
- Jain, P. K., Wen Kang, Soin, H., and Youhao Xi (2002). Analysis and design considerations of a load and line independent zero voltage switching full bridge dc/dc converter topology. *IEEE Transactions on Power Electronics*, 17(5):649–657.
- Jiang, Y., Wang, L., Fang, J., Li, R., Han, R., and Wang, Y. (2020). A high-efficiency zvs wireless power transfer system for electric vehicle charging with variable angle phase shift control. *IEEE Journal of Emerging and Selected Topics in Power Electronics*, pages 1–1.
- Johnson, S. D. and Erickson, R. W. (1988). Steady-state analysis and design of the parallel resonant converter. *IEEE Transactions on Power Electronics*, 3(1):93–104.

- Kanamarlapudi, V. R. K., Wang, B., Kandasamy, N. K., and So, P. L. (2018). A new zvs full-bridge dc–dc converter for battery charging with reduced losses over full-load range. *IEEE Transactions on Industry Applications*, 54(1):571–579.
- King, R. and Stuart, T. A. (1981). A normalized model for the half-bridge series resonant converter. *IEEE Transactions on Aerospace and Electronic Systems*, AES-17(2):190–198.
- Kojori, H., Dewan, S., and Lavers, J. (1991). Steady-state analysis and design optimization of an inductor-transformer resonant dc-dc converter. *IEEE Transactions on Industry Applications*, 27(3):515–522.
- Kranprakon, P., Sangswang, A., and Naetiladdanon, S. (2016). Asymmetrical duty cycle control with phase limit of llc resonant inverter for an induction furnace. In *2016 13th International Conference on Electrical Engineering/Electronics, Computer, Telecommunications and Information Technology (ECTI-CON)*, pages 1–6.
- Lappalainen, K. and Valkealahti, S. (2016). Effects of irradiance transition characteristics on the mismatch losses of different electrical pv array configurations. *IET Renewable Power Generation*, 11(2):248–254.
- Li, W. and He, X. (2011). Review of nonisolated high-step-up dc/dc converters in photovoltaic grid-connected applications. *IEEE Transactions on Industrial Electronics*, 58(4):1239–1250.
- Li, X. and Bhat, A. K. S. (2012). A utility-interfaced phase-modulated high-frequency isolated dual lcl dc/ac converter. *IEEE Transactions on Industrial Electronics*, 59(2):1008–1019.
- Liu, K. H. and Lee, F. C. Y. (1990). Zero-voltage switching technique in dc/dc converters. *IEEE Transactions on Power Electronics*, 5(3):293–304.
- Liu, R. and Lee, C. Q. (1992). Series resonant converter with third-order commutation network. *IEEE Transactions on Power Electronics*, 7(3):462–468.
- Lucia, O., Burdio, J. M., Millan, I., Acero, J., and Llorente, S. (2009). Efficiency optimization of half-bridge series resonant inverter with asymmetrical duty cycle

- control for domestic induction heating. In *2009 13th European Conference on Power Electronics and Applications*, pages 1–6.
- Mahdavi, J., Emaadi, A., Bellar, M. D., and Ehsani, M. (1997). Analysis of power electronic converters using the generalized state-space averaging approach. *IEEE Transactions on Circuits and Systems I: Fundamental Theory and Applications*, 44(8):767–770.
- Mandal, K., El Aroudi, A., Abusorrah, A., Al-Hindawi, M., Al-Turki, Y., Giaouris, D., and Banerjee, S. (2015). Non-linear modelling and stability analysis of resonant dc–dc converters. *IET Power Electronics*, 8(12):2492–2503.
- Martin-Ramos, J. A., Diaz, J., Pernia, A. M., Prieto, M. J., and Linera, F. F. (2002). Modelling of the prc-lcc resonant topology with a capacitor as output filter using edf. In *2002 IEEE 33rd Annual IEEE Power Electronics Specialists Conference. Proceedings (Cat. No.02CH37289)*, volume 3, pages 1337–1342 vol.3.
- Outeiro, M. T., Buja, G., and Czarkowski, D. (2016). Resonant power converters: An overview with multiple elements in the resonant tank network. *IEEE Industrial Electronics Magazine*, 10(2):21–45.
- Pilawa-Podgurski, R. C. N., Sagneri, A. D., Rivas, J. M., Anderson, D. I., and Perreault, D. J. (2009). Very-high-frequency resonant boost converters. *IEEE Transactions on Power Electronics*, 24(6):1654–1665.
- Ranganathan, V. T., Ziogas, P. D., and Stefanovic, V. R. (1982). A regulated dc–dc voltage source converter using a high frequency link. *IEEE Transactions on Industry Applications*, IA-18(3):279–287.
- Redl, R. (1996). A new soft-switching dc/dc converter and its application in an off-line power supply with integral high-quality rectification. In *PESC Record. 27th Annual IEEE Power Electronics Specialists Conference*, volume 1, pages 402–407 vol.1.
- Saeed, J. (2018). A zvs-zcs phase shift full bridge dc-dc converter with secondary-side control for battery charging applications. *International Journal of Circuit Theory and Applications*, 46(7):1407–1415.

- Salem, M., Jusoh, A., Idris, N. R. N., Das, H., and Alhamrouni, I. (2018). Resonant power converters with respect to passive storage (lc) elements and control techniques – an overview. *Renewable and Sustainable Energy Reviews*, 91:504 – 520.
- Seok, H., Han, B., Kwon, B., and Kim, M. (2018). High step-up resonant dc–dc converter with ripple-free input current for renewable energy systems. *IEEE Transactions on Industrial Electronics*, 65(11):8543–8552.
- Severns, R. (1990). Topologies for three element resonant converters. In *Fifth Annual Proceedings on Applied Power Electronics Conference and Exposition*, pages 712–722.
- Shakib, S. M. S. I. and Mekhilef, S. (2017). A frequency adaptive phase shift modulation control based llc series resonant converter for wide input voltage applications. *IEEE Transactions on Power Electronics*, 32(11):8360–8370.
- Shi, K., Zhang, D., Zhou, Z., Zhang, M., and Gu, Y. (2016). A novel phase-shift dual full-bridge converter with full soft-switching range and wide conversion range. *IEEE Transactions on Power Electronics*, 31(11):7747–7760.
- Shu, L., Chen, W., Ma, D., and Ning, G. (2018). Analysis of strategy for achieving zero-current switching in full-bridge converters. *IEEE Transactions on Industrial Electronics*, 65(7):5509–5517.
- Steigerwald, R. L. (1984). High-frequency resonant transistor dc-dc converters. *IEEE Transactions on Industrial Electronics*, IE-31(2):181–191.
- Steigerwald, R. L. (1984). High-frequency resonant transistor dc-dc converters. *IEEE Transactions on Industrial Electronics*, IE-31(2):181–191.
- Steigerwald, R. L. (1985). Analysis of a resonant transistor dc-dc converter with capacitive output filter. *IEEE Transactions on Industrial Electronics*, IE-32(4):439–444.
- Steigerwald, R. L. (1988). A comparison of half-bridge resonant converter topologies. *IEEE Transactions on Power Electronics*, 3(2):174–182.

- Sun, X., Li, X., Shen, Y., Wang, B., and Guo, X. (2017). Dual-bridge llc resonant converter with fixed-frequency pwm control for wide input applications. *IEEE Transactions on Power Electronics*, 32(1):69–80.
- Tahavorgar, A. and Quaicoe, J. E. (2017). A dual series-resonant dc–dc converter. *IEEE Transactions on Power Electronics*, 32(5):3708–3718.
- Tahavorgar, A. and Quaicoe, J. E. (2019). Stability and small-signal analyses of the dual series-resonant dc–dc converter. *IEEE Transactions on Power Electronics*, 34(2):1420–1430.
- Tan, X. and Ruan, X. (2016). Equivalence relations of resonant tanks: A new perspective for selection and design of resonant converters. *IEEE Transactions on Industrial Electronics*, 63(4):2111–2123.
- Tasi-Fu Wu and Yu-Kai Chen (1998). Modeling pwm dc/dc converters out of basic converter units. *IEEE Transactions on Power Electronics*, 13(5):870–881.
- Van Dijk, E., Spruijt, J. N., O’Sullivan, D. M., and Klaassens, J. B. (1995). Pwm-switch modeling of dc-dc converters. *IEEE Transactions on Power Electronics*, 10(6):659–665.
- Wai, R. and Wang, W. (2008). Grid-connected photovoltaic generation system. *IEEE Transactions on Circuits and Systems I: Regular Papers*, 55(3):953–964.
- Witulski, A. F. and Erickson, R. W. (1990). Extension of state-space averaging to resonant switches and beyond. *IEEE Transactions on Power Electronics*, 5(1):98–109.
- Wu, H., Jin, X., Hu, H., and Xing, Y. (2016). Multielement resonant converters with a notch filter on secondary side. *IEEE Transactions on Power Electronics*, 31(6):3999–4004.
- Yang, D., Chen, C., Duan, S., Cai, J., and Xiao, L. (2016). A variable duty cycle soft startup strategy for llc series resonant converter based on optimal current-limiting curve. *IEEE Transactions on Power Electronics*, 31(11):7996–8006.
- Yang, E. X., Lee, F. C., and Jovanovic, M. M. (1992). Small-signal modeling of lcc resonant converter. In *PESC '92 Record. 23rd Annual IEEE Power Electronics Specialists Conference*, pages 941–948 vol.2.

- Yang, R., Ding, H., Xu, Y., Yao, L., and Xiang, Y. (2014). An analytical steady-state model of lcc type series-parallel resonant converter with capacitive output filter. *IEEE Transactions on Power Electronics*, 29(1):328–338.
- York, B., Yu, W., and Lai, J. (2013). An integrated boost resonant converter for photovoltaic applications. *IEEE Transactions on Power Electronics*, 28(3):1199–1207.
- Zong, S., Luo, H., Li, W., Deng, Y., and He, X. (2016). Asymmetrical duty cycle-controlled llc resonant converter with equivalent switching frequency doubler. *IEEE Transactions on Power Electronics*, 31(7):4963–4973.

PUBLICATIONS BASED ON THE THESIS

Papers in refereed journals

1. **Vijaya Bhaskar Reddy** and H. Nagendrappa, “Comparison of Phase-Shift and Modified Gating Schemes on Working of DC-DC LCL-T Resonant Power Converter”, in *IEEE Transactions on Circuits and Systems II: Express Briefs*, vol. 68, no. 1, pp. 346-350, Jan. 2021, doi: 10.1109/TC-SII.2020.2992368.
2. **Vijaya Bhaskar Reddy** and H. Nagendrappa, “Fixed-Frequency Modified Gating Signals Controlled High-Frequency Isolated LCL-T DC-DC Resonant Power Converter”, in *IEEE Transactions on Industrial Electronics*. (Under Review)

Papers published in conference proceedings

1. **Vijaya Bhaskar Reddy** and H. Nagendrappa, “Modified Gating Signal Controlled High-Frequency Transformer Isolated LCL-T Type DC-DC Resonant Power Converter”, 8th *IEEE India International Conference on Power Electronics (IICPE)*, Jaipur, India, 2018, pp. 1-6, doi: 10.1109/IICPE.2018.8709588.
2. **Vijaya Bhaskar Reddy** and H. Nagendrappa, “Fixed frequency control of LCL-T resonant power converter with capacitive output filter”, 6th *International Conference on Computer Applications In Electrical Engineering-Recent Advances (CERA)*, Roorkee, India, 2017, pp. 568-573, doi: 10.1109/CERA.2017.8343392.

Bio-data

Name : Vijaya Bhaskar Reddy G.

Date of birth: 21-08-1992

E-mail: vijaybhaskarreddy2a9@gmail.com

Mobile: +91-8754560978

Education

- **M.Tech**, Power Electronic and Drives, Vellore Institute of Technology, Chennai, Tamilnadu, 2015.
- **B.Tech.**, Electrical & Electronics Engineering, QIS College of Engineering and Technology, Ongole, Andra Pradesh, 2013.

Address

H.No.: 8-60, Zulakallu

Piduguralla, Guntur

Andra Pradesh -522413,

India.